Structure Property Relations and Finite Element Analysis of Ram Horns: A Pathway to Energy Absorbent Bio-Inspired Designs

M W Trim

STRUCTURE PROPERTY RELATIONS AND FINITE ELEMENT ANALYSIS

OF RAM HORNS: A PATHWAY TO ENERGY ABSORBENT

BIO-INSPIRED DESIGNS

By

Michael Wesley Trim

A Dissertation
Submitted to the Faculty of
Mississippi State University
in Partial Fulfillment of the Requirements
for the Degree of Doctor of Philosophy
in Mechanical Engineering
in the Department of Mechanical Engineering

Mississippi State, Mississippi

August 2011

STRUCTURE PROPERTY RELATIONS AND FINITE ELEMENT ANALYSIS

OF RAM HORNS: A PATHWAY TO ENERGY ABSORBENT

BIO-INSPIRED DESIGNS

By

Michael Wesley Trim

Approved:

Mark F. Horstemeyer
Professor of Mechanical Engineering
Chair in Computational Solid Mechanics
Center for Advanced Vehicular Systems
(Major Professor)

Hongjoo Rhee
Associate Director and Research
Professor
Center for Advanced Vehicular Systems
(Committee Member)

Lakiesha Williams
Assistant Professor of Agriculture and
Biological Engineering
(Committee Member)

Jun Liao
Assistant Professor of Agriculture and
Biological Engineering
(Committee Member)

Joanna McKittrick
Professor of Mechanical and Aerospace
Engineering
University of California, San Diego
(Committee Member)

Steven R. Daniewicz
PACCAR Chair and Head of Mechanical
Engineering
(Graduate Coordinator)

Sarah A. Rajala
Dean of the James Worth Bagley College
of Engineering

Name: Michael Wesley Trim

Date of Degree: August 6, 2011

Institution: Mississippi State University

Major Field: Mechanical Engineering

Major Professor: Dr. Mark F. Horstemeyer

Title of Study: STRUCTURE PROPERTY RELATIONS AND FINITE ELEMENT
ANALYSIS OF RAM HORNS: A PATHWAY TO ENERGY
ABSORBENT BIO-INSPIRED DESIGNS

Pages in Study: 125

Candidate for Degree of Doctor of Philosophy

A recently emerging engineering design approach entails studying the brilliant design solutions found in nature with an aim to develop design strategies that mimic the remarkable efficiency found in biological systems. This novel engineering approach is referred to as bio-inspired design. In this context, the present study quantifies the structure-property relations in bighorn sheep (*Ovis canadensis*) horn keratin, qualitatively characterizes the effects of a tapered spiral geometry (the same form as in a ram's horn) on pressure wave and impulse mitigation, describes the stress attenuation capabilities and features of a ram's head, and compares the structures and mechanical properties of some energy absorbent natural materials. The results and ideas presented herein can be used in the development of lightweight, energy absorbent, bio-inspired material designs.

Among the most notable conclusions garnered from this research include:

- Horn keratin behaves in an anisotropic manner similar to a long fiber composite.

- Moisture content dominates the material behavior of horn keratin more than anisotropy, age, and stress-state. This makes moisture content the most influential parameter on the mechanical behavior of horn keratin.

- Tapered geometries mitigate the impulse generated by a stress wave due to the convergent boundary and a continually decreasing cross sectional area such that greater uniaxial stresses and subsequent axial deformation arises. Furthermore, the tapered geometry introduces small shear stresses that further decrease the impulse.

- Spiral geometries attenuate the impulse generated by a stress wave by the introduction of shear stresses along the length of the spiral. These shear stresses introduce transverse displacements that function to lessen the impulse.

- When both a taper and spiral geometry are used in a design, their synergistic effects multiplicatively reduce the impulse

- Tough natural materials have a high porosity, which makes them light-weight, while increasing their compressive energy absorption ability.

- Biomaterials whose functions include protection and energy absorption feature a multiscale, hierarchical, composite structure. The constituent materials are arranged in such ways to achieve a synergistic effect, where the properties of the composite exceed the properties of its constituents. Biological materials are therefore not confined to the law of mixtures.

Key words: Structure-Property Relations, Bio-Inspired Design, FEA, Energy Absorption

DEDICATION

I dedicate this dissertation my family: firstly to my parents, Mike and Jackie, because without their selfless support and diligence, this research would have not been possible. I also dedicate this work to my children, Jacob and McKay, who contributed to the realization of this document in their own unique way. They continually motivate and inspire me to do my best.

ACKNOWLEGEMENTS

TABLE OF CONTENTS

LIST OF TABLES

LIST OF FIGURES

viii

ix

CHAPTER I

INTRODUCTION

Traditionally, engineers have followed an Edisonian approach in new material and design development, where innovations come by trial-and-error discovery. Nature contains a plethora of ingenious design strategies. Therefore, nature is a tremendous resource of engineering solutions. A recently emerging engineering approach, termed bio-inspired design, entails mimicking the proven, brilliant solutions found in nature (Ball 2001). Unfortunately, nature doesn't give up her secrets easily and natural designs are generally very complex.

The process of bio-inspired design is two-step process. The first step involves gaining an understanding of the biological design. Only then can the process of mimicry begin. Both processes involve a great deal of research and technology. The bio-inspired research movement is continually gaining momentum. And, as technology continually progresses, the study and mimicry of complex biological systems is becoming more tractable. Several useful and interesting bio-inspired designs have already emerged, e.g. (Munch et al. 2008, Chen et al. 2007, Taya 2003, Yu 2007). Undoubtedly, *many* more will transpire in the following years.

The fundamental physical laws that govern the design of man-made materials obviously apply to natural material as well. However, nature is able to achieve a great

1

deal more efficiency and functionality by assembling constituent materials in clever ways. In these structures lie nature's solutions to achieving high strength and ductility, i.e. toughness and energy absorption.

D'Arcy Thompson's (1917) classic work was the first to examine living organisms in the context of the mechanical forces acting on them. More recent reports describe the significant progress that has been made in determining the structure-property relationships in various types of biomaterials and reviews of biological composite materials that can be utilized in bio-inspired design (McKittrick et al. 2010, Mayer 2005, Meyers et al. 2006, Srinivasan et al. 1996, Ji and Gao 2004, Arciszewski and J. 2006, Sanchez, Arribart and Giraud Guille 2005, Elices 2000, Currey 2005, Weiner, Addadi and Wagner 2000, Fratzl and Weinkamer 2007, Zhou 2000, Mohammed and Murphy 2009). Biological organisms often produce composites, comprised of inorganic and organic components that are organized into complex, hierarchical structures.

Natural composites have mechanical properties that vastly exceed the properties of their relatively weak constituents. Therefore, unlike synthetic materials, natural materials are not confined by mixture law. The synergistic effect achieved by biomaterials stems from their multi-scale hierarchical structures (Vincent 1990). Understanding how biological structures provide superior mechanical properties is the first step in developing useful bio-inspired design strategies. In this context, the present work focuses on ram horn with aim to understand its structure-property relations and determine how it achieves such remarkable toughness and energy absorption.

2

Chapters 2-5 of this document were all submitted for publication as separate works prior to the creation of this document. These chapters were only slightly modified to form this single, comprehensive dissertation.

Chapter 2 pertains to quantification of the structure-mechanical property relations of horn keratin for use in modeling and finite element analysis (FEA). Several parameters are investigated to determine their effects on the stress-strain behavior of horn keratin, namely: material orientation (transverse vs. longitudinal), spatial location within the horn (base vs. middle vs. tip of horn), stress-state (tension vs. compression), and hydration level (wet vs. dry). The mechanical properties of horn keratin obtained via micro-indentation, tensile, and compressive testing are compared. Fracture surfaces are analyzed and mechanical property gradients throughout the horn keratin sheath are investigated.

In Chapter 3, FEA is used to show the geometrical effects on pressure and impulse mitigation within a solid. In nature, there are several toroidal designs that are employed for mitigating shock waves; a couple of examples include a ram's horn or the hyoid bone on the back of a woodpecker's jaw. Four geometries with equal, circular cross-sections and equal lengths are evaluated using three dimensional FEA. The geometries each have an increasing degree of complexity: a uniform cylinder, a tapered cylinder (or cone), a cylinder that was spiraled in a two dimensional plane and a cylinder that was tapered and spiraled in a two dimensional plane. The primary aim of Chapter 3 is to answer the question: Does the spiral geometry of the ram horn play a role in the mitigation of the stress wave induced during a blow?

3

FEA results from a dynamic head-butting impact of a bighorn sheep simulation are presented in Chapter 4. Emphasis is placed on the contributions of the moisture content of the horn keratin and the horn geometry to the overall shock absorbing ability of the system. Four FEA models are used: 1) a bighorn sheep head with horns and dry horn keratin, 2) a bighorn sheep head without horns and dry horn keratin, 3) a bighorn sheep head with horns and hydrated horn keratin, and 4) a bighorn sheep head without horns and hydrated horn keratin. Results include quantification of the von Mises stresses, hydrostatic pressures, principal strains, impulses, and strain energies. These data are used to identify parametric trends in the shock mitigation capabilities of a ram head subjected to impact loading. To our knowledge, the three dimensional explicit finite element simulations of a ram head impact presented in Chapter 4 are the first to have ever been performed.

Chapter 5 presents a comparative study of the structure-property relations of turtle shell, armadillo shell, and ram horn. The hierarchical multiscale structures and compressive mechanical behavior of these natural, tough materials are examined and compared with emphasis on the energy absorption. The lessons from nature presented in Chapter 5 can be used as bio-inspired design strategies for the development of lightweight energy absorbent materials.

Finally, Chapter 6 provides a summary of the studies presented herein and outlines some of the most notable conclusions. Also included in Chapter 6 are suggestions for related future research.

4

CHAPTER II

STRUCTURE-PROPERTY RELATIONS IN BIGHORN SHEEP HORN KERATIN

Introduction

The horns of male bovids (e.g., goats, sheep, cattle, buffalo, bison, and antelope) are mainly used in combat with other males to gain access to females for mating (Leuthold 1977, Schaller 1977, Kitchener 1987b) and can also be used in visual display, defense from predators, and thermoregulation (Geist 1971, Goss 1983). Bighorn sheep (*Ovis canadensis*) can exert up to an estimated 3400 N of force during a fight (Kitchener 1988), which is more than any other sheep species. Unlike antlers, horns are permanent structures and are highly susceptible to damage accumulation over a lifetime (Goss 1983). Consequently, horns must be tough and resistant to flaw propagation, which could promote stress concentration and weaken the horns (Kitchener 1987b). Kitchener (1988) concluded that a crack must be more than 60% of the transverse basal dimension of the horn in order for there to be catastrophic failure at the maximum stresses developed during fighting. The remarkable resilience of horns makes them an excellent study if one is attempting to understand damage deterring mechanisms and impact resistant materials in nature.

The keratin sheath of horn has a higher energy absorption ability than bone or antler (Kitchener 1991). This allows horn sheaths to localize deformation away from the

5

immediate area of the brain and other cranial organs in the ram upon impact. Based on finite element analyses of goat skull impacts, Farke (2008) hypothesized that the keratinous horn sheaths are one of the most important features that contribute to the shock absorption ability of ram skulls.

Horns are made up of a sheath of keratin and a core of cancellous bone (Packer 1983). There are also areas of compact bone and air-filled sinuses within the frontal bones and horn cores. The keratin sheath is the primary impact load bearing material of the horn and is the focus of this chapter. The horn sheath is a composite material comprised of tough, crystalline fibers made of α-keratin set in a compliant, amorphous keratin matrix (Frasier and MacRae 1980, Kitchener and Vincent 1987). The keratin fibers serve to strengthen and stiffen the structure by forming long, hollow, fiber-like tubules. This dispersed tubule microstructure has been observed in other tough biological materials such as hoof, bone, antler, and dentin (McKittrick et al. 2010). Keratin is also found in many tough biological materials such as skin, hair, horns, and hooves. In a horn, the keratin fibers are parallel to the growth direction and are stacked in a lamellar fashion through the thickness of the horn.

Horn keratin has a lamellar structure (2–5 µm in thickness) stacked in the radial direction with tubules (~40 x 100 µm in diameter) dispersed between the lamellae. The tubules extend along the length of the horn in the growth direction (Tombolato et al. 2010). The tubules are randomly spaced in the transverse and radial direction, which leads to the material behavior in these two directions being nearly identical. Therefore, horn keratin is a transversely isotropic material, i.e., isotropic in the transverse and radial directions.

The mechanical properties of keratin are also highly dependent on moisture content (Feughelman 1997, Bertram and Gosline 1987, Fraser, MacRae and Rogers 1972, Kitchener and Vincent 1987). On a living animal, 'fresh' horn keratin contains around 20 wt.% water, but if left to soak, horn keratin can absorb up to about 40 wt.% water, depending on the sample thickness (Kitchener and Vincent 1987). In keratin, water interacts only with the amorphous matrix and not with the crystalline fibers (Druhala and Feughelman 1974). Wet horn keratin is less susceptible to damage, because the more compliant matrix can more readily yield and flow (Vincent 1990, Kitchener 1987a). In completely dry horn keratin, the stiffness of the matrix and fiber are assumed to be equal (Fraser and MacRae 1980), and this stiffness is higher compared to wet horn keratin. However, a balance between the stiffness of dry horn and the compliance of wet horn must exist for optimal performance of the horn, i.e. to maximize energy absorption and minimize damage accumulation; the stiffness of the horn must be modulated.

The anisotropy of fiber composites is well known. The behavior of the fibers in a composite subjected to compressive loads is analogous to the behavior of columns on an elastic foundation. Thus, the response of a composite to a compressive load is strongly dependent on matrix properties such as the shear stiffness. This observation is different from the response of the composite to longitudinal tensile loads, which is governed primarily by the fibers.

Because of the curvature of a ram's horn, when an impact occurs, a multi-axial stress-state arises. Historically, a von Mises (1913) assumption would be employed in a finite element analysis of this type of structure and impact, but the von Mises stress asserts that compression and tension would give equal and opposite values of the stress

7

tensor. Recently, Dighe, Gokhale and Horstemeyer (2002) showed that there exists fairly large differences between tension, compression, and torsion under quasi-static loads of homogeneous aluminum alloys, and Tucker et al. (2009) showed that large differences exist under high strain rates as well. As such, the tension-compression asymmetry would induce a different kind of stress (and strain) response than if the structure had equal and opposite tension and compression stresses. For horn keratin, these stress-state differences have not been examined.

In a recent study, Tombolato, et al. (2010) examined the microstructure, bending and compressive properties at different orientations in order to study the failure mechanisms of *Ovis canadensis* horn keratin. Similar studies have also been performed on similar keratin-based materials such as rhinoceros horns (Druhala and Feughelman 1974), bovine hooves (Zhang et al. 2007), and equine hooves (Kasapi and Gosline 1999). However, the various stress-state properties and in particular the tensile response and mechanical property gradients of a horn have not been examined. In addition, micro-indentation has never been performed on ram horn keratin. Micro-indentation is one accurate method in determining the hardness and modulus of a material (Oliver and Pharr 1992). Micro-indentation also provides a means to investigate the property gradients through the cross-sectional area in order to give insight into the hardness levels that could in turn be used for bio-inspired designs.

The primary purpose of this chapter is to quantify the structure-property relations of horn keratin for use in modeling and simulation. The structure-property data presented in this writing can be used for constitutive modeling in finite element analysis in order to solve boundary value problems related to ram's striking each other with their horns.

8

Previous data are not amenable to calculating material constants since constitutive model calibration typically requires homogeneous stress-states, i.e., uniaxial tension and compression. The parameters considered in this study that affect the stress-strain behavior are the following: material orientation (transverse vs. longitudinal), spatial location within the horn (base vs. middle vs. tip of horn), stress-state (tension vs. compression), and hydration level (wet vs. dry).

In this chapter, the stress state dependent structure-property relations for different orientations and moisture contents at various locations throughout a horn are investigated. As such, the mechanical properties obtained via micro-indentation, tensile, and compressive testing are compared. Fracture surfaces are analyzed and mechanical property gradients throughout the horn keratin sheath are studied.

Materials and Methods

Two well-preserved bighorn sheep (*Ovis canadensis*) horn sheaths, approximately 1 m in longitudinal length and 12 cm in diameter at the base, were obtained from Montana Fish, Wildlife, and Parks. The rams were killed for reasons unrelated to this study. The specimens were stored in a controlled environment with a temperature of – 18°C and a relative humidity of 30 percent until needed.

Compressive and tensile testing was performed on a universal testing machine (Instron EM Model 5869, Norwood, Massachusetts, USA) equipped with a 50 kN load cell. Three sets of specimens used for tensile and compression testing were cut from the base, middle, and tip of the horn using a water-jet cutting machine. Care was taken to cut the specimens such that the fiber orientation was aligned either parallel or perpendicular

to the long axis of the specimen. The dog-bone tensile specimens had a length of 37 mm, a width of 18 mm, a gage length of 12 mm, a gage width of 6 mm and a thickness of 3 mm. The cylindrical compression specimens had a diameter of 3 mm and thickness of 3 mm. A constant strain rate of 3.0×10^{-3} s^{-1} was maintained for all testing. Toughness values were calculated as the area under the average tensile stress-strain curves.

Twenty cylindrical specimens were harvested from each region of the horn (base, middle, and tip) for compression testing, ten in the longitudinal direction, and ten in the transverse direction. Of the ten longitudinal specimens from each region, five were tested in the 'wet' condition and five were tested in the 'dry' condition. The same was done for the transverse specimens. Similarly, twenty dog-bone shaped tensile specimens were taken from each region of the horn, ten of which were longitudinally oriented and ten were transversely oriented. Of the ten longitudinal and the ten transverse tension specimens from each region, five of each were tested in the 'wet' condition and five were tested in the 'dry' condition, i.e., each uniaxial tension and compression test was repeated five times. The resulting stress-strain curves for the duplicate tests were averaged together and the standard deviation at various strain levels was calculated. In this parametric study, sixty compression tests and sixty tension tests were performed in all. No specimens were harvested from the region of the horns where growth lines were obvious, as the growth lines could potentially affect the mechanical properties.

To investigate the effects of moisture content of the horn keratin, specimens were tested in both wet and ambient dry conditions. Prior to testing, the test-pieces for the wet condition were soaked in de-ionized water for three days, which has been determined to be a sufficient period for complete swelling to occur (Kitchener and Vincent 1987).

10

Subsequent to testing, the wet specimens were weighed and placed in a 130ºC oven for 24 hours. Once dried, the specimens were reweighed to determine the weight percent of water that was present in the specimen at time of testing. The specimens for the dry condition were allowed to acclimate to ambient humidity and temperature (roughly 50% RH and 20ºC). Each mechanical test was repeated five times and the results were averaged together.

The density of the horn keratin taken from the base, middle, and tip of the horn was determined using Archimedes principle. Cylindrical samples, having a diameter of 3 mm and thickness of 3 mm, were harvested from the three horn regions. The dry weight, $W_1,$ of each sample was obtained using a digital scale. The samples were then impregnated with oil and reweighed to obtain W_2. The oil-impregnated sample was then immersed in water of known density, $\phi_w,$ via a suspension wire with known mass, W_w to obtain W_3.

The Archimedes density was then calculated using:

$$\rho = \frac{W_1 \phi_w}{W_2 - (W_3 - W_w)} \tag{2.1}$$

A micromechanical testing machine (TI 900 Triboindentor, Hysitron Inc., Minneapolis, MN, USA) equipped with a Berkovich indentor tip was used to determine hardness and elastic modulus of the horn sheath material. An indentation profile was made across a polished cross section of the horn. Care was taken to not probe any voids within the material. Spacing between indentations 6 s 6   xim6 tely 500 μm t66 void 6 any strain hardening or residual stress effects. Mechanical testing specimen locations, orientations, and dimensions are schematically summarized in Figure 2.1.

11
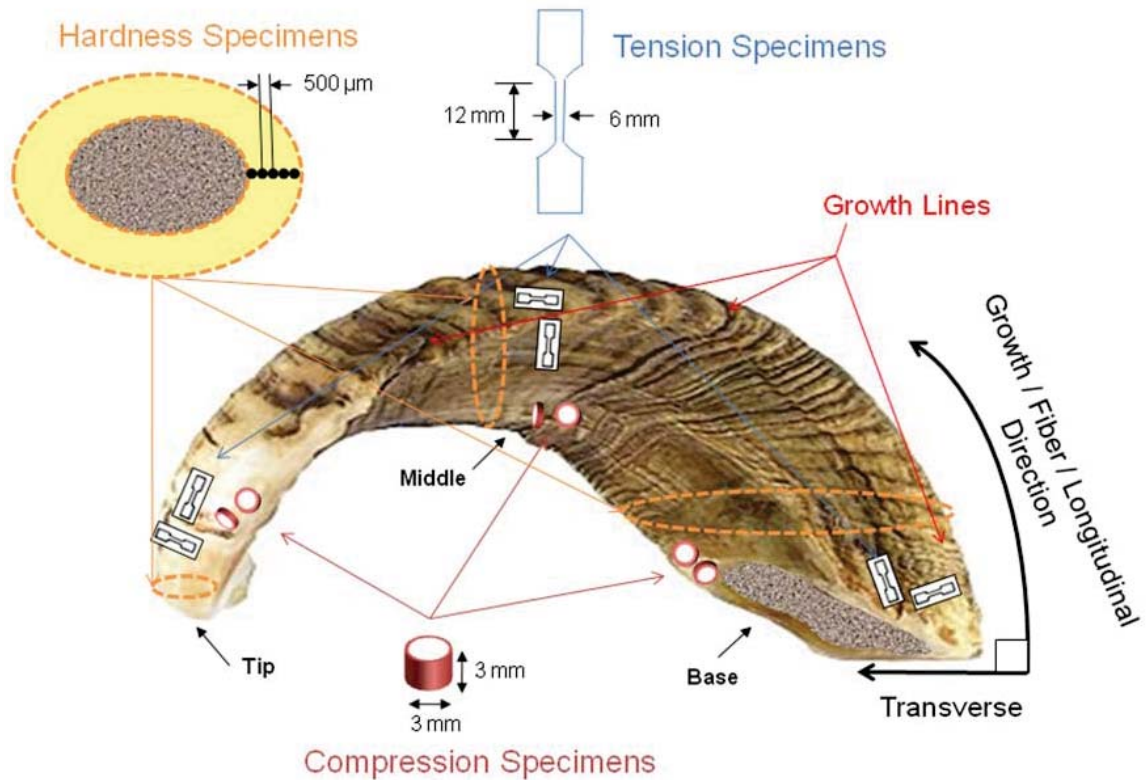
Figure 2.1   Schematic illustration of the mechanical testing specimen locations, dimensions, and orientations.

Fracture surfaces were examined using a field emission scanning electron microscope (SEM) equipped with EDS (JSM-6500F, JEOL Ltd., Tokyo, Japan). Specimens were mounted on aluminum sample holders and all surfaces not being examined were coated with silver paint. All specimens received a 12.5 nm platinum coating in a sputter coater (Polaron SC7640, Quorum Technologies Ltd., Connecticut, USA) prior to observation in secondary electron (SE) mode at 5 kV. SEM images were analyzed using the Image-Analyzer software package developed by the Center for Advanced Vehicular Systems (CAVS) at Mississippi State University (MSU) to quantify the microstructural features of the ram horn keratin material.

12

Results and Discussion

Similar to many other biological tissues (Fratzl and Weinkamer 2007), horn keratin is a hierarchical material. At the molecular level, horn keratin comprises helical, α-keratin protofibrils. These protofibrils assemble into rope-like structures called intermediate filaments (Fraser et al. 1986). The crystalline intermediate filaments are oriented along the growth direction and coil up into hollow, elliptically shaped tubules, with average minor and major diameters of 29.6 µm and 93 µm, respectively. These tubules, which resemble hollow reinforcing fibers, are embedded in an amorphous keratin matrix. The matrix is akin to a randomly oriented, chopped fiber composite. There is also a porosity gradient through the thickness of the horn, with the highest porosity being at the outer surface (Tombolato et al. 2010). At the macroscale, a horn takes the shape of a logarithmic or growth spiral.

Hardness and elastic modulus profiles obtained via microindentation are shown in Figure 2.2 and Figure 2.3, respectively. The hardness and modulus increase slightly radially when traversing from the outside surface of the horn to the core. There is about a 40% increase in the elastic modulus and hardness from the outer surface of the horn to the core of the keratin sheath. This indicates that there is a microstructure gradient from the core to the outer surface of the horn.

There is no significant difference between the longitudinal and transverse moduli of the keratin sheath. All indents were performed on the amorphous keratin matrix. This is the reason that there was no difference between longitudinal and transverse properties

13
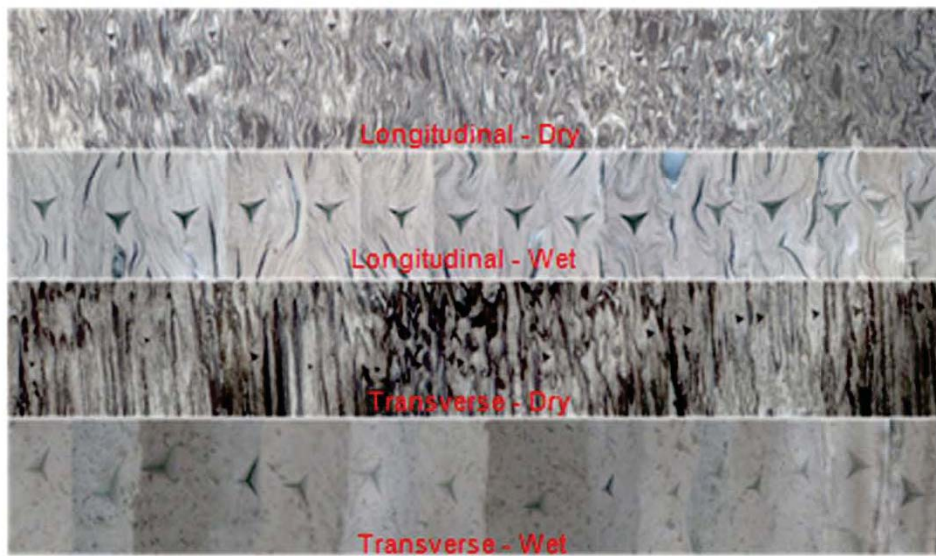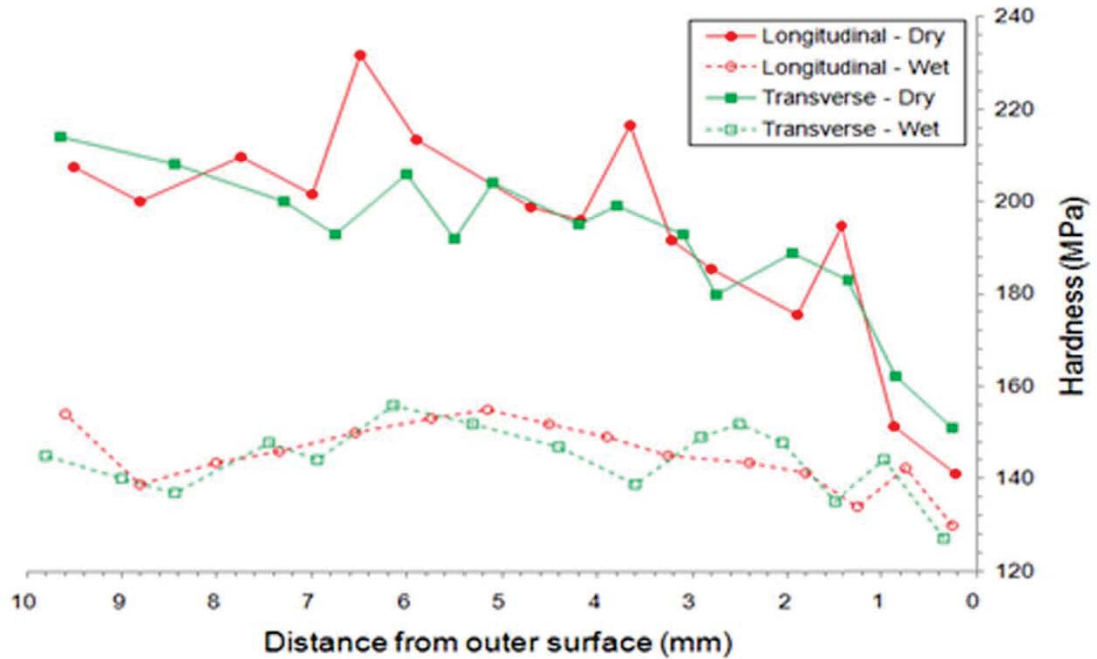
Figure 2.2   Longitudinal and transverse hardness profile of ram horn keratin in the wet (35 wt.% water) and dry (10 wt.% water) condition.

on the indentation profiles. Wet horn keratin shows considerably more compliance than dry horn keratin. The optical micrographs of the indentation profiles show significant swelling of the matrix in the wet keratin. In the longitudinal micrographs, the lamellae and porosity due to the tubules are clearly observed.

14
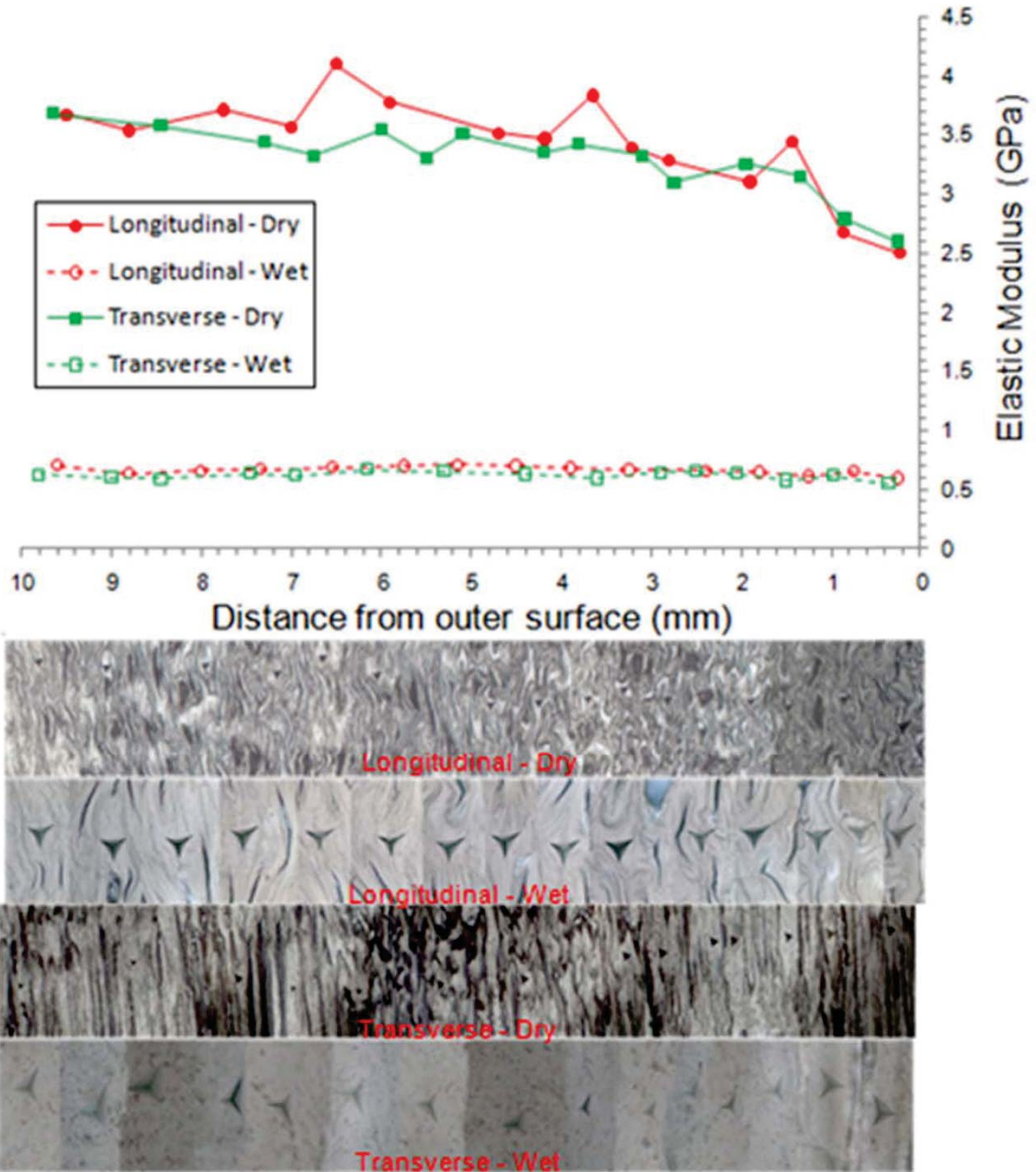
Figure 2.3   Longitudinal and transverse elastic modulus profile of ram horn keratin in the wet (35 wt.% water) and dry (10 wt.% water) condition.

Figure 2.4 (a) is a SEM micrograph of a polished, transverse section of horn keratin and Figure 2.4 (b) is the output from Image-Analyzer. The tubules resemble elliptical pores when viewed at this orientation. The average minor axis length of the

15

elliptical tubules is 29.6 μm and the average major axis length is 93.0 μm. The aspect ratio, defined as the major axis length over the minor axis length, averaged 3.14. And, the average porosity is 6.3%. These values are consistent with the results of Tombolato, et al. (Tombolato et al. 2010), who estimated the minor and major axis lengths to be 40 μm and 100 μm, respectively; and the porosity to be 7%.
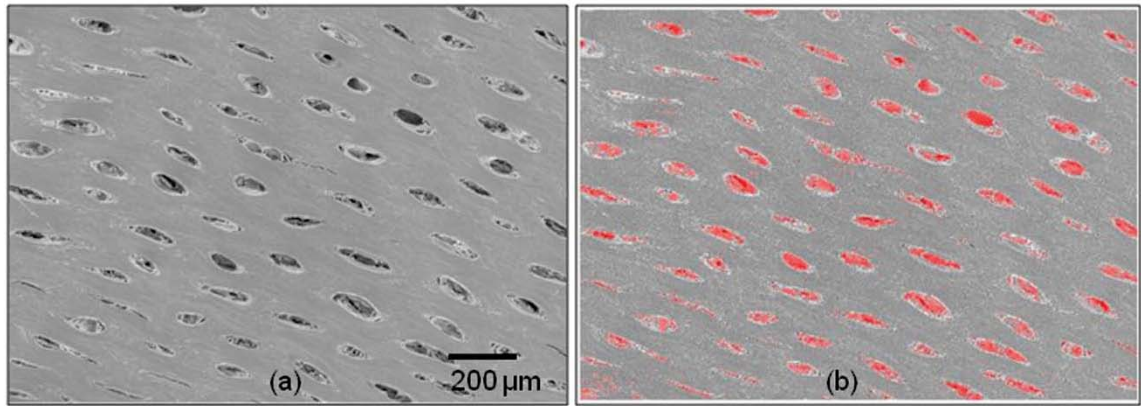
Figure 2.4   (a) SEM micrograph of polished transverse section of ram horn keratin. (b) Image analyzer output showing 6.3% porosity.

Anisotropy of Horn Keratin

When comparing the anisotropic behavior of the horn keratin, one can observe from the data (Table 2.1, Table 2.2, and Figure 2.5) that the longitudinal direction is stiffer (higher elastic modulus), stronger (higher yield and ultimate stress), and more ductile (higher elongations to failure) than the transverse direction, regardless of hydration level (wet or dry) or loading state (tension or compression). These mechanical property characteristics are similar to those of synthetic long fiber reinforced composite materials (Johnston 1987).

16

Table 2.1   Average (n=15) tensile longitudinal and transverse tensile mechanical properties of bighorn sheep horn keratin.

Specimen	Elastic Modulus (GPa)	Yield Strength (MPa)	Ultimate Strength (MPa)	Failure Strain (%)	Toughness (MJ/m^3)
Dry					
Longitudinal	3.9 ± 0.2	62.0 ± 6.9	77.3 ± 7.2	3.5 ± 0.5	2.0 ± 0.3
Transverse	2.8 ± 0.5	37.4 ± 9.1	44.9 ± 9.8	2.1 ± 0.8	0.6 ± 0.2
Wet					
Longitudinal	0.7 ± 0.1	13.3 ± 1.1	27.4 ± 4.5	61.2 ± 2.1	11.7 ± 1.2
Transverse	0.5 ± 0.2	7.6 ± 2.3	21.1 ± 4.9	59.3 ± 3.9	8.5 ± 2.5

Although in horn keratin, the tubules act as the crystalline reinforcement and the matrix comprises randomly oriented, chopped keratin fibers. When the tubules are oriented perpendicular to the loading direction, they tend to produce stress concentrations at the interface and within the matrix. As such, fiber composites subjected to transverse tensile loads fail, because of matrix cracking or interface debonding similar to their synthetic counterparts. Although the qualitative characteristics of the dry horn keratin are similar to graphite-epoxy long fiber composites (Johnston 1987) and in particular the failure strain, the values for elastic modulus and ultimate strengths are approximately two orders of magnitude weaker for the horn keratin.

When examining the different methods of quantifying the elastic moduli for the horn keratin, the micro-indentation and tensile loading and unloading moduli were generally larger than the forward compression and bending test results as summarized in

17

Table 2.3, which also includes data from Tombolato et al. (Tombolato et al. 2010). For example, the longitudinal, dry values ranged from 3.0-4.1 GPa for the indentation and tensile unloading data, and ranged from 1.3-2.4 GPa for the compression and bending data. Similarly for the transverse dry horn keratin, the values ranged from 2.3- 3.6 GPa for the indentation and tensile tests and 1.6-2.2 GPa for the compression and bending tests. Because of the compliance in testing machines, usually lower values are expected for the forward loading moduli measurements when compared to moduli measurements taken during unloading. The strong agreement between the elastic moduli measurements taken during forward loading and during unloading indicates that machine compliance did not affect the tensile test results.

Table 2.2   Average (n=15) compressive longitudinal and transverse mechanical properties of bighorn sheep horn keratin.

Specimen	Elastic Modulus (GPa)	Yield Strength (MPa)	Yield Strain (%)
Dry			
Longitudinal	2.2 ± 0.1	72.1 ± 5.4	3.4 ± 1.0
Transverse	1.9 ± 0.2	60.6 ± 12.8	3.1 ± 1.5
Wet			
Longitudinal	0.20 ± 0.1	3.7 ± 0.3	4.1 ± 0.2
Transverse	0.10 ± 0.01	4.1 ± 0.7	4.0 ± 0.2

The longitudinal and transverse moduli values ranged from 0.3-0.8 GPa for the wet horn keratin. The anisotropy of the elastic modulus significantly decreased with increasing moisture content of the horn keratin. The strong similarity between the 'wet' mechanical properties in the longitudinal and transverse directions suggests that hydration severely degraded the matrix phase, which led to a matrix dominated deformation behavior. The hydrated, amorphous matrix gives a much more isotropic response (Kitchener 1987a, Feughelman 1997).

Table 2.3 also shows that in the dry condition, the tensile testing resulted in a higher longitudinal elastic modulus than the micro-indentation testing. This attests to a stiffening effect of the tubules, since micro-indentation testing only probes the properties of the randomly oriented keratin fiber matrix. Furthermore, the ambient dry, transverse elastic modulus from micro-indentation is higher than the elastic modulus obtained via tensile testing. In the horn sheath, the tubules tend to debond from matrix under tensile loading. These trends, however, are much less noticeable in the wet horn keratin.

In terms of the anisotropic behavior on the failure strains, the dry, longitudinal compressive strength was only slightly higher than the transverse compressive strength indicating very good fiber-matrix adhesion, as expected due to the strong chemical bonds between fibers and matrix of identical composition. Water apparently strengthens this bonding even more, which is evidenced by the nearly identical longitudinal and transverse compressive strengths for wet horn keratin.
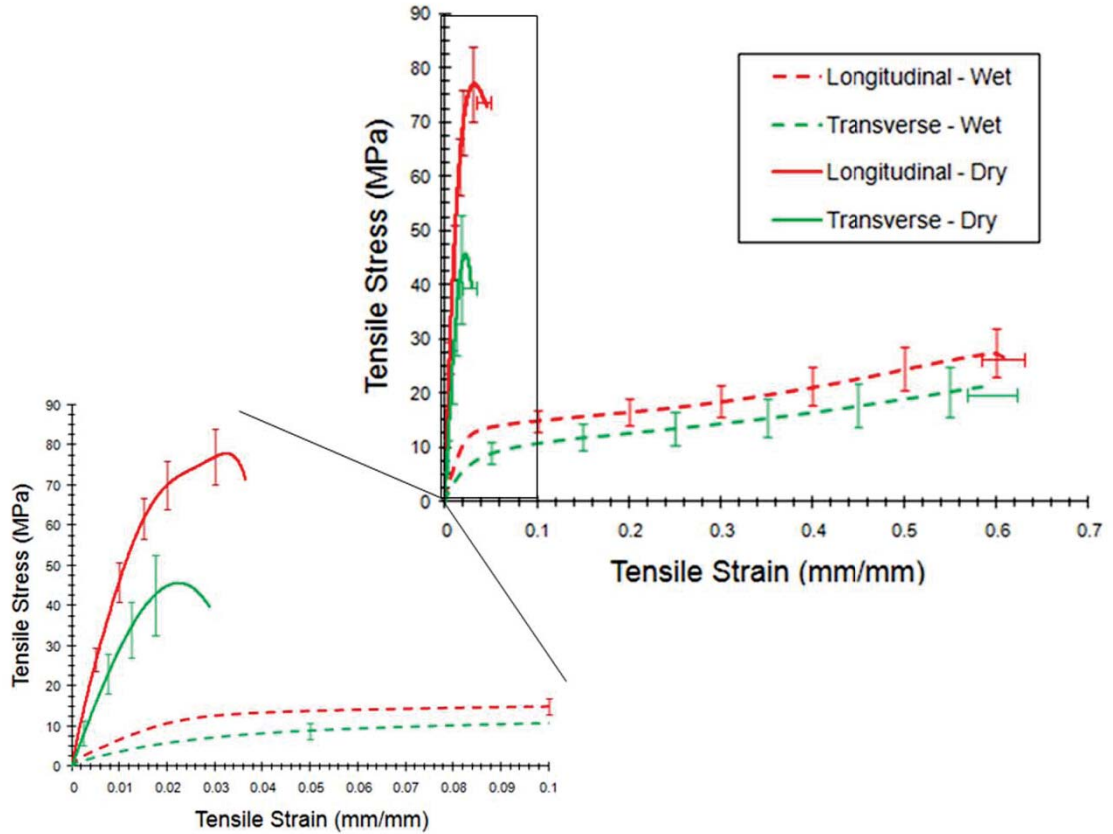
Figure 2.5   Average (n=15) tensile longitudinal and transverse stress-strain response for horn keratin in the wet (35 wt.% water) and dry (10 wt.% water) condition.

Moisture Dependence of Horn Keratin

Although qualitative similarities exist between synthetic long fiber composites and the dry horn keratin in terms of anisotropy, the qualitative character of wet horn keratin is much different than synthetic composites, because of the greater failure strains and associated fairly large fracture toughness, as illustrated in Figure 2.5. This flexibility of the horn moving back and forth between a stiffer and a more flexible structure is not available for the synthetic long fiber composites.

Related to the wet and dry specimen fracture surfaces, SEM images of tensile specimens revealed different failure phenomena between the longitudinal and transverse conditions, and examples are illustrated in Figure 2.6. The nearly flat fracture surface of the dry, longitudinal specimen was characterized by brittle fracture.

Table 2.3   Comparison of longitudinal and transverse elastic moduli of big horn sheep horn keratin obtained via tension, compression, micro-indentation, and three-point bending in the wet (35 wt.% water) and dry (10 wt.% water) condition.

	Tensile Test: Forward Loading (GPa)	Tensile Test: Unloading (GPa)	Compressive Test: Forward Loading (GPa)	Micro-indentation Test: Unloading (GPa)	Three-Point Bending Test: Forward Loading (GPa)	Ref
Dry						
Longitudinal	3.9 ± 0.2	4.0 ± 0.2	2.2 ± 0.1	3.44 ± 0.41	--	*
	--	--	1.64 ± 0.3	--	2.20 ± 0.2	‡
Transverse	2.8 ± 0.5	2.9 ± 0.3	1.9 ± 0.2	3.29 ± 0.28	--	*
	--	--	1.94 ± 0.3	--	1.69 ± 0.5	‡
Wet						*
Longitudinal	0.7 ± 0.1	0.5 ± 0.2	0.20 ± 0.1	0.67 ± 0.03	--	‡
	--	--	0.53 ± 0.2	--	0.81 ± 0.4	
Transverse	0.5 ± 0.2	0.4 ± 0.3	0.10 ± 0.1	0.62 ± 0.03	--	*
	--	--	0.25 ± 0.1	--	0.63 ± 0.2	‡

* This work
‡ (Tombolato et al. 2010)

Very little tubule pullout was observed, demonstrating a high degree of tubule-matrix adhesion, as seen in Figure 2.7. However, the wet, longitudinal fracture surface

21

showed an extremely ductile fracture mode, evidenced by a very deep, convoluted cup-and-cone type fracture.
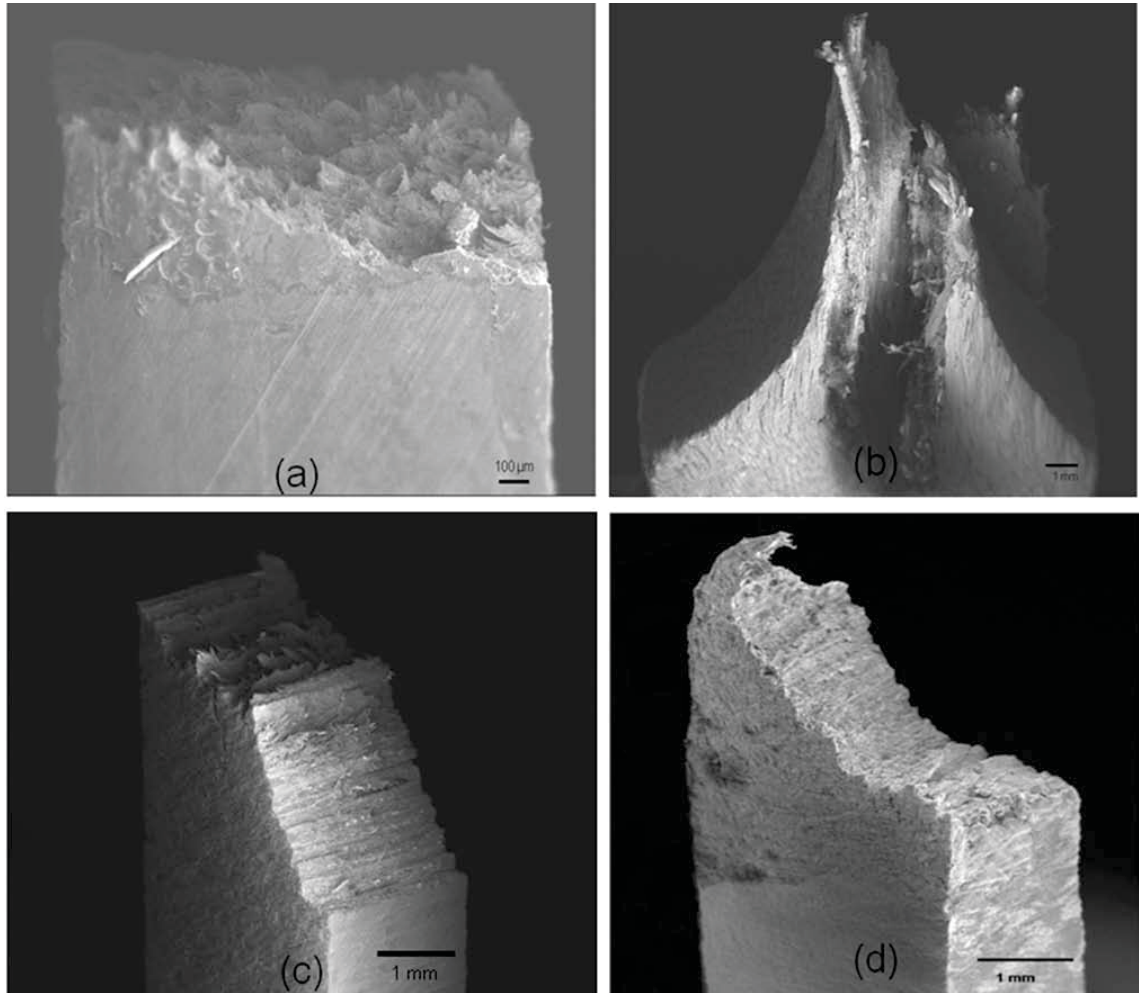
Figure 2.6   SEM fractographs of ram horn keratin specimens tested in tensile (a) longitudinal dry, (b) longitudinal wet, (c) transverse dry, and (d) transverse wet conditions.

Significant necking was also observed on the wet, longitudinal specimens but the specimen had fully recovered to its original shape and dimensions by the time of imaging. For the transverse loading specimens, both the wet and dry specimens exhibited

22

a shear type failure mode. Tubules perpendicular to the loading direction acted essentially to produce stress concentrations at the interface and in the matrix. When subjected to transverse tensile loads, wet horn keratin failed predominately because of matrix failure (around the tubules), with some transverse tubule pullout, as seen in Figure 2.8. However, ambient dry horn keratin exhibited delamination and tubule fracture, as seen in Figure 2.9.
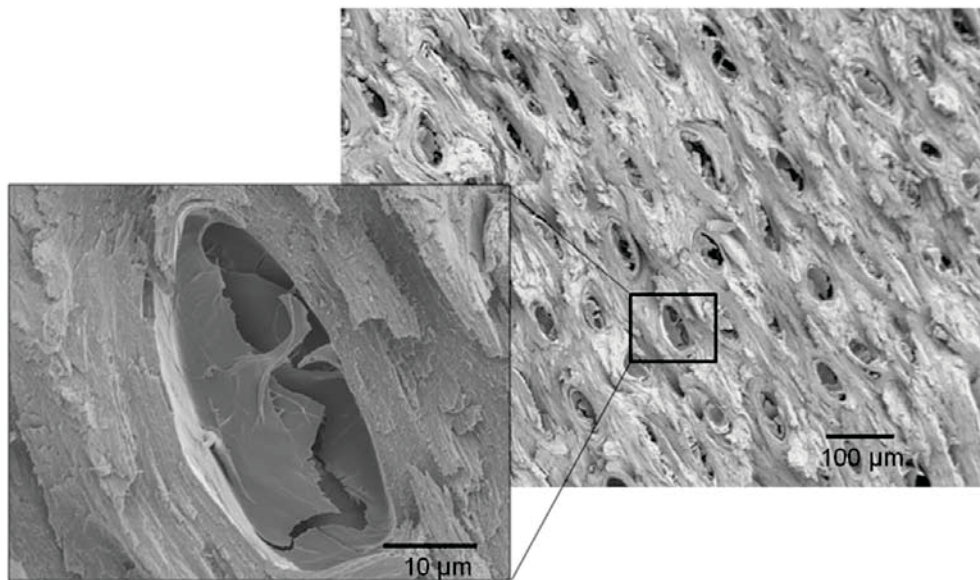
Figure 2.7   SEM micrograph of longitudinal, dry horn keratin specimen fractured in tension. The growth direction is out of the page. Loading was applied parallel to growth direction. Very little fiber pullout occurred, demonstrating a high degree of fiber-matrix adhesion.

The larger failure strains and fracture toughness under the wet conditions indicate that wet horn keratin is more resilient than dry horn keratin, i.e., the wet horn keratin material can elastically store more energy per unit volume than dry horn keratin. Under

23

the wet conditions, the energy absorption capability is much greater than in the dry conditions by approximately five to ten times.
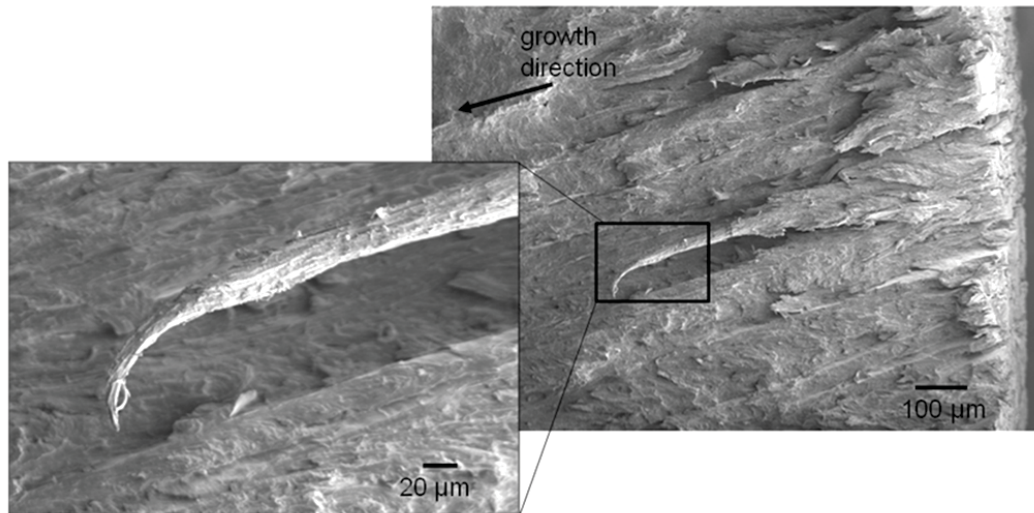
Figure 2.8   SEM fractographs of transverse, wet horn keratin specimen fractured in tension. Loading was applied perpendicular to growth direction. Failure occurred predominately because of matrix failure, with some transverse fiber pullout.
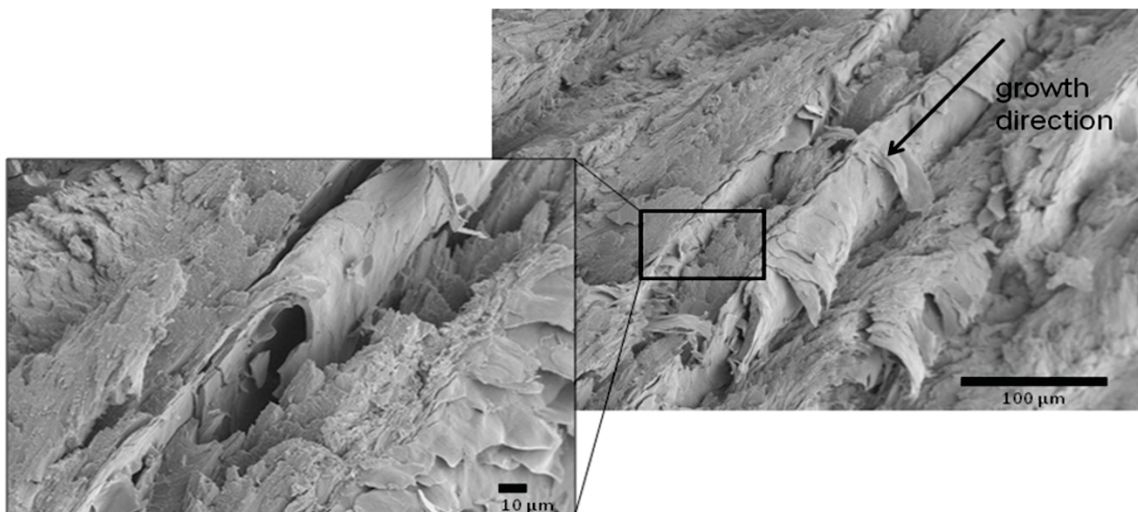
Figure 2.9   SEM fractographs of transverse, dry horn keratin specimen fractured in tension. Loading was applied perpendicular to growth direction. Failure exhibited delamination and fiber fracture.

Bovids display an interesting behavior known as horning, where they frequently rub their horns in mud and against wet vegetation prior to fighting (Kitchener 1987b). The animals that keep the keratinous sheath of their horns adequately hydrated maintain toughness and notch-insensitivity in their horns against the desiccating environment. This lessens the probability of the animal sustaining an injury.

Location Dependence within the Horn

It may be expected that strength and stiffness differences exist along the length of horn due to aging, with the material near the tip of the horn being older than the material at the base of the horn due to new horn being laid down as the animal grows larger. Figs.2.10-12 show the stress-strain behavior of the horn keratin at different locations for the examination of anisotropy between the longitudinal and transverse directions, stress-state dependence between tension and compression, and the wet-dry conditions. In particular, Figure 2.10 shows the average (n=5) tensile longitudinal and transverse tensile stress-strain behavior for horn keratin samples located in the base, middle, and tip regions in wet (35 wt.% water) and ambient dry (10 wt.% water) conditions. Taking into account the standard deviation associated with the five specimens that were tested in each condition, it appears that the location did not have a significant effect on the stress-strain behavior since the response from the base, middle, and tip of the horn were highly consistent, with the average curve for each parametric test falling within the bounds of deviation for the other tests. We suspect that with a larger sample population, these results would further converge. As a note related to the anisotropic and wet-dry discussion earlier, the mechanical properties were calculated by averaging the results

25

from the base, middle, and tip regions because of the lack of distinguishing the stress-strain behavior.
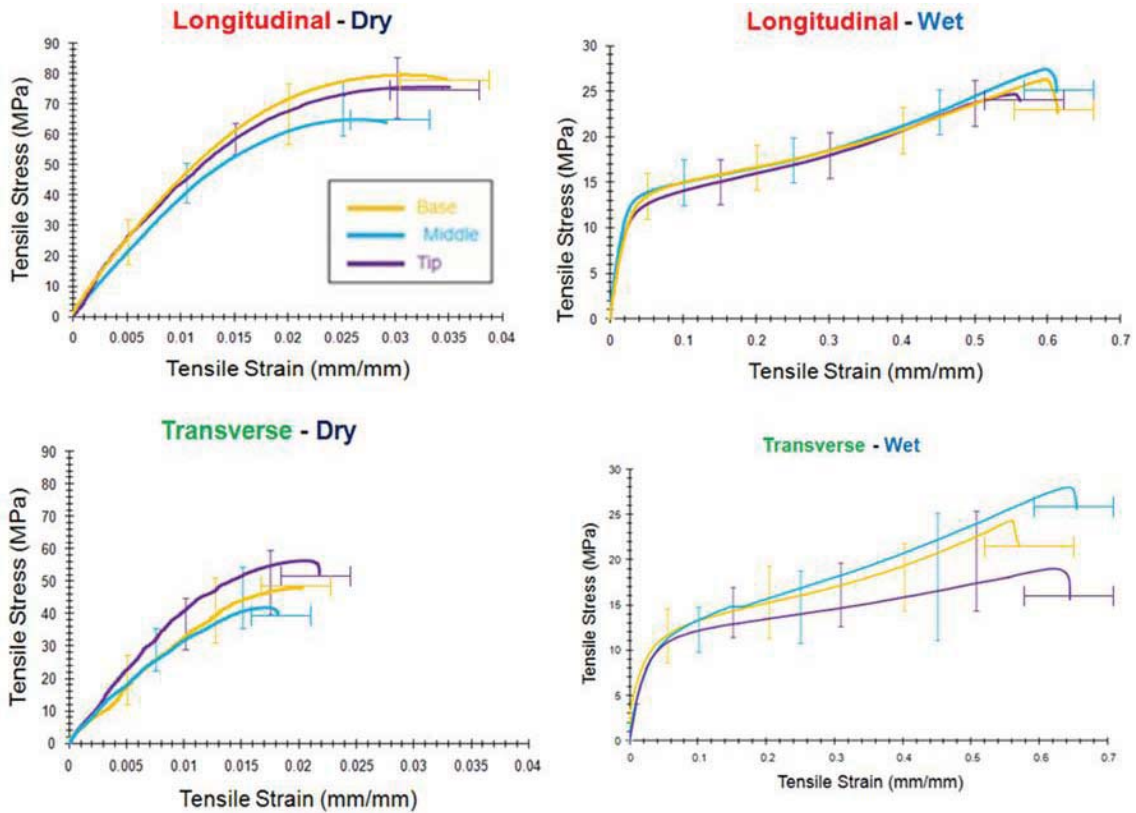
Figure 2.10   Average (n=5) longitudinal and transverse tensile stress-strain response for horn keratin samples located in the base, middle, and tip regions of the horn in the wet (35 wt.% water) and ambient dry (10 wt.% water) condition.

Figure 2.11 and Figure 2.12 show these average (n=5) longitudinal and transverse compressive stress-strain behavior for horn keratin samples located in the base, middle, and tip regions in the wet and dry condition. Similar to the tension loading case, the compressive stress-strain behavior did not vary much with location. Also, Figure 2.13

26

shows the comprehensive average (n=15) of the longitudinal and transverse compressive

stress-strain behaviors of all three locations in the wet and ambient dry conditions.
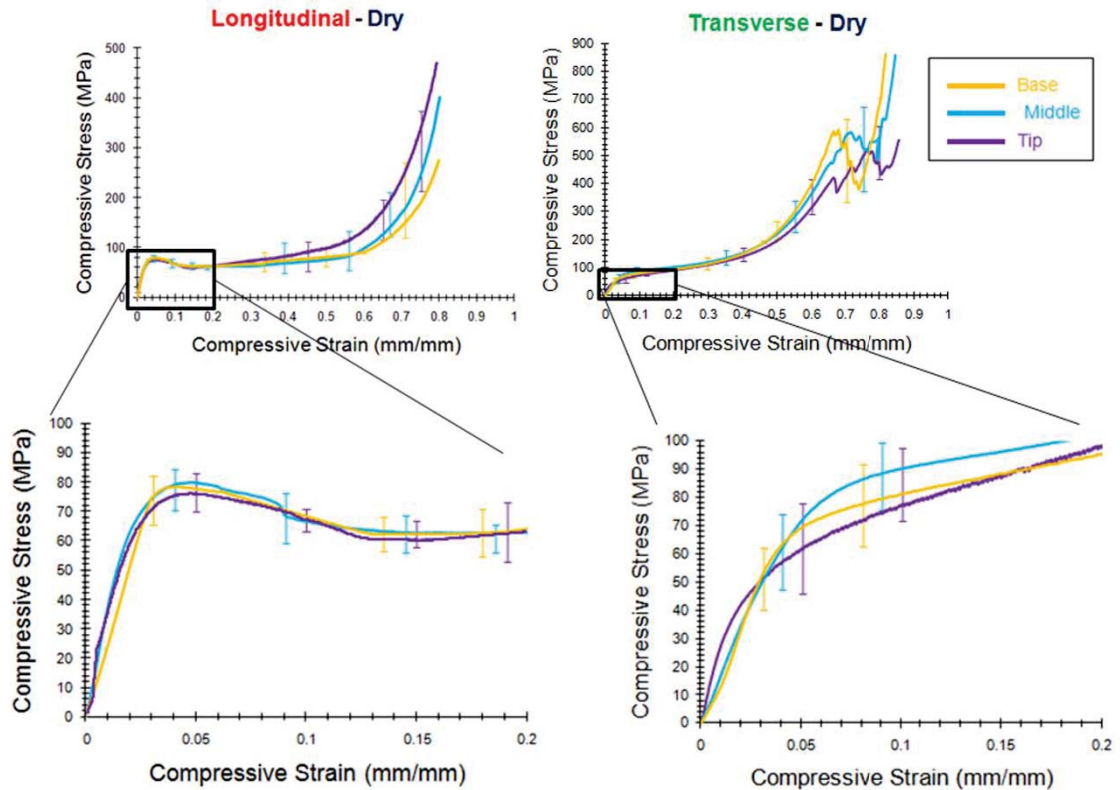
Figure 2.11   Average (n=5) longitudinal and transverse compressive stress-strain
response for horn keratin samples located in the base, middle, and tip
regions in the dry (10 wt.% water) condition.

The density of the horn keratin material as measured at base, middle, and tip was

determined to be 1.238, 1.237, and 1.237 g/cm^3, respectively. This indicates that similar

to the tensile and compressive stress-strain behavior, density also does not vary

significantly along the length of the horn. For comparison, Kevlar, a lightweight,

composite material widely used for penetration resistance, has a density of 1.439 g/cm^3,

27

and polycarbonate, a common polymer known for its high impact resistance has a density of about 1.21 g/cm^3 (Callister 2007).

Stress-State Dependence of Horn Keratin

When comparing the stress-state dependence of the horn keratin we see very different material responses, particularly when we compare the tension and compression behaviors. Figure 2.14(a) illustrates that for the dry horn keratin, the stress-strain behavior up to approximately 1% strain, the compression and tension curves are similar but deviate beyond 3% strain.

Another difference between tension and compression for the dry horn keratin is that the strain to failure is much greater for compression extending up to 20% before failure. Interestingly, the longitudinal stress-strain behavior was greater than the transverse behavior under tension, but under compression the opposite behavior was realized later in strain (after 10% strain). A similar behavior is observed for the wet horn keratin, as seen in Figure 2.14 (b). Also, for the wet horn keratin stress-strain behavior, one can observe that the tension curves are higher than the compression curves for the both the longitudinal and transverse directions.

When one compares the failure mechanisms under tension and compression, different modes arise. Figure 2.6 and Figure 2.15 show the fracture surfaces under tension and compression, respectively. As shown in Figure 2.15, the buckling of the lamellae under compression effectively decreases the "work hardening" in the stress-strain behavior when compared to the tensile loading. However, the tension failure strains are much lower than that of compression, even when the tensile failure strains are

28

increased because of water. The damage progression under compression from the longitudinal fracture specimens shown in Figure 2.15 (a) and (b) illustrate shear microbuckling followed by delamination.
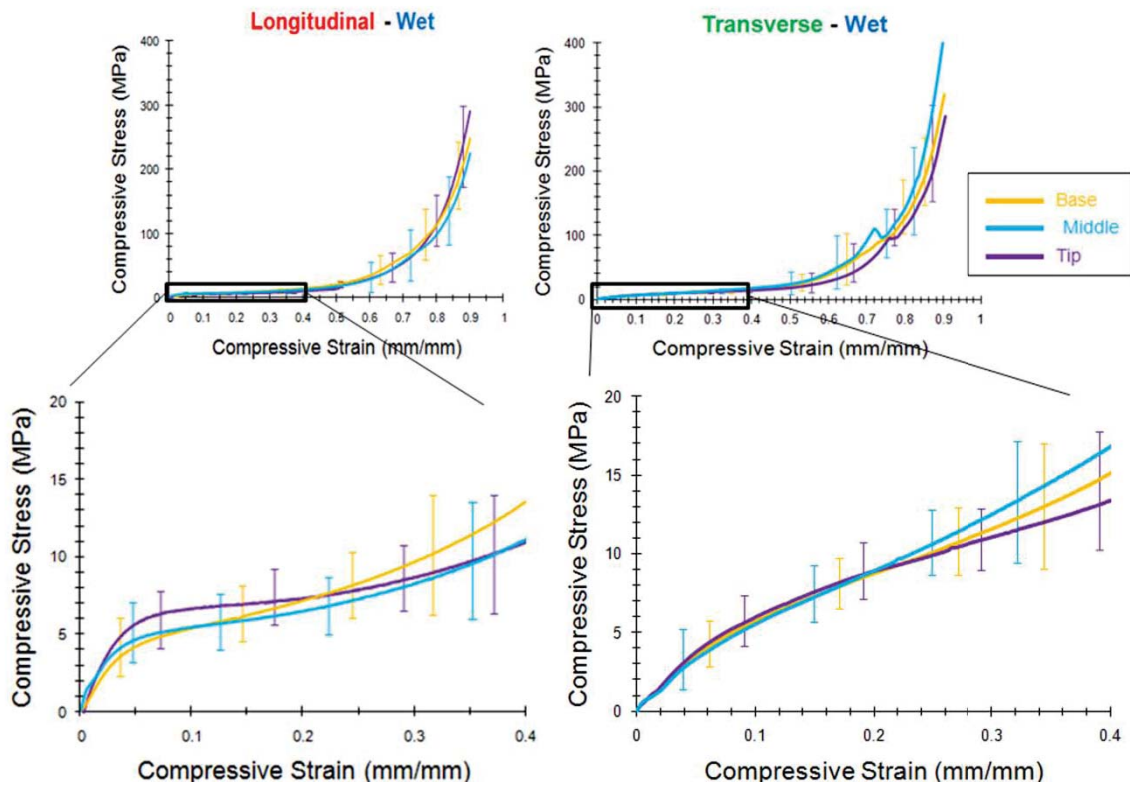
Figure 2.12   Average (n=5) longitudinal and transverse compressive stress-strain response for horn keratin samples located in the base, middle, and tip regions in the wet (35 wt.% water) condition.

This is quite different than the tensile fracture behavior, which was observed to be fiber failure in the dry specimen and ductile necking in the wet specimen. In the transverse direction (Figure 2.14 (c) and (d)), both the tension and compression loading fracture surfaces exhibited shear failure along the direction of maximum shear stress (45° to loading axis) with some delamination experienced in the compression specimens.

29
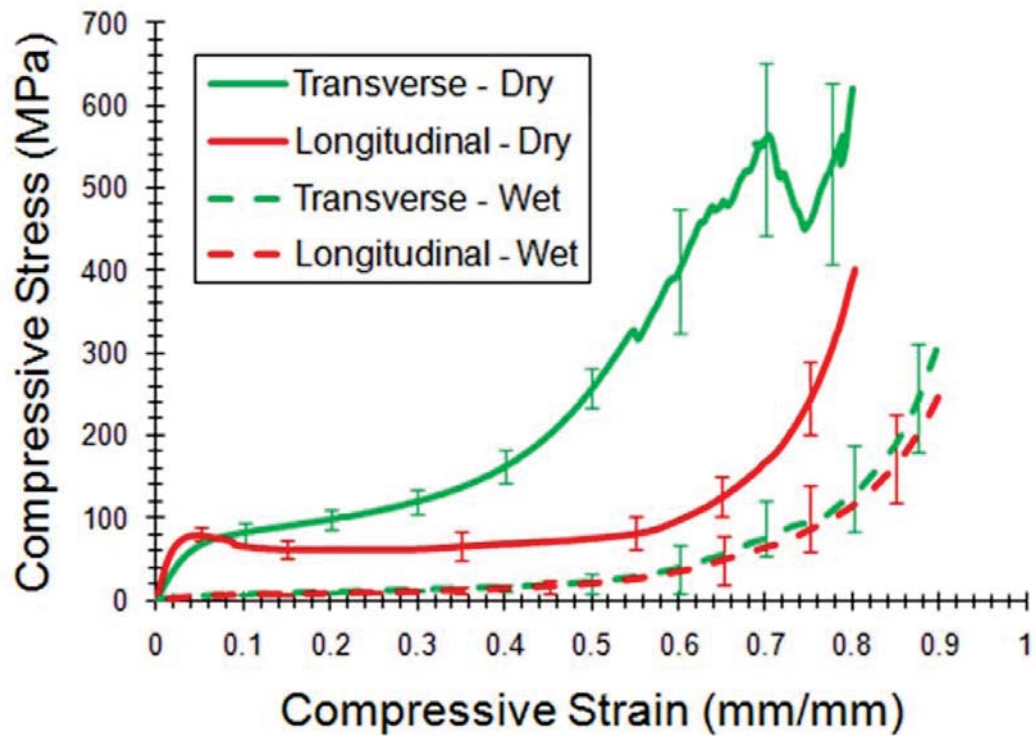
Figure 2.13   Average (n=15) compressive longitudinal and transverse stress-strain
response for horn keratin in the wet (35 wt.% water) and dry (10 wt.%
water) condition.

The incident strike onto the horn during head-butting induces a local compression
loading condition, so extending the energy absorption capability in compression is key.
With the microbuckling observed in compression, the energy absorption is extended
beyond what otherwise could be realized. This same microbuckling of lamellae to extend
the energy absorption was also observed in turtle shells (Rhee et al. 2009) and abalone
nacre (Menig et al. 2000). This microbuckling in compression to increase energy
absorption has also been observed in synthetic long fiber composites (Fleck and
Budiansky 1991, Fleck and Sridhar 2002) and metal foams (Gibson and Ashby 1999).

30
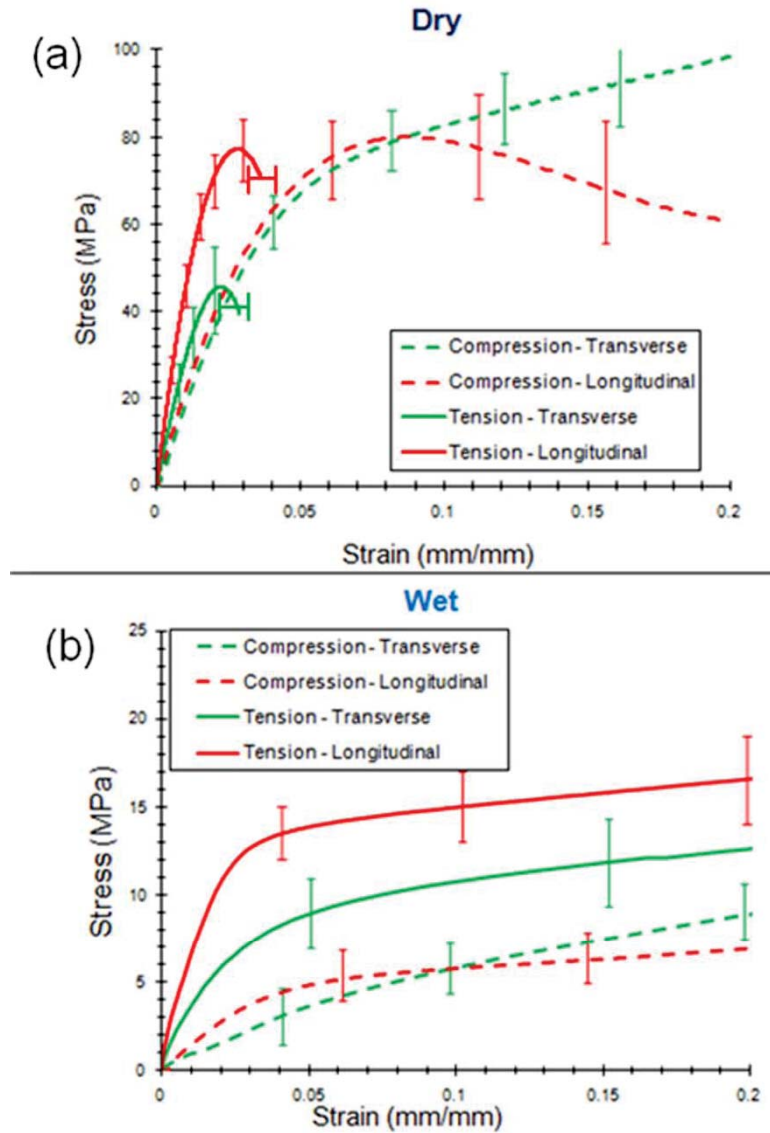
Figure 2.14   Stress-state dependence of ram horn keratin in the (a) ambient dry and (b) wet condition.

The compressive stress-strain behavior of the ram horn keratin, as seen in Figure 2.13, consists of three regimes: a linear elasticity region, a long collapse plateau, and finally densification. This type of compressive stress-strain behavior is characteristic of synthetic foams but has also been observed in biological materials such as turtle shells (Rhee et al. 2009) and bones (Currey 2002).

31
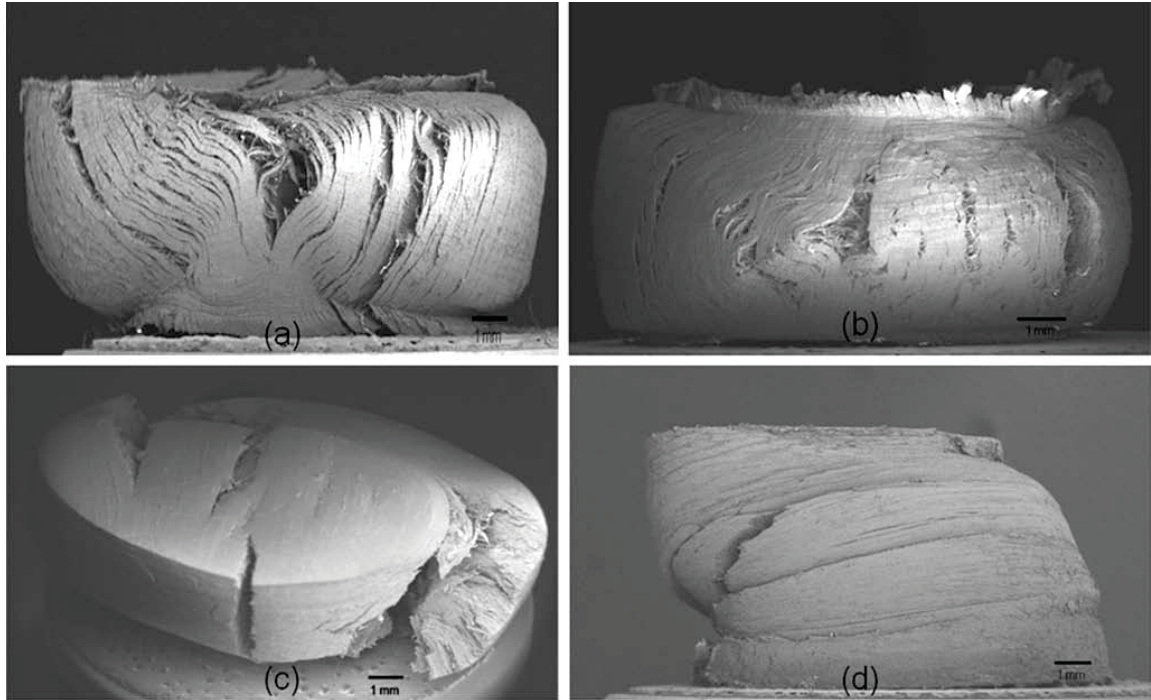
Figure 2.15   SEM micrographs of compressive (a) longitudinal dry, (b) longitudinal wet, (c) transverse dry, (d) transverse wet horn keratin fracture specimens.

Not only is the difference between tension and compression important to the mechanical response of the spiraled ram horn, but the unloading under each loading condition as well. The unloading can reveal how much of the forward loading is elastic, visocoelastic, or viscoplastic. Furthermore, the unloading can reveal more accurate elastic moduli measurements because of the absence of the machine compliance (the machine effect is very small, considering the elastic modulus of the horn keratin is ~ 2 GPa compared with steel at 200 GPa). Figure 2.16 shows tension and compression forward loading and unloading stress-strain data to illustrate the non-monotonicity of the material behavior. For both the wet and dry conditions, irreversible strains were evidenced with more exhibited for the wet condition. Because both reversible and irreversible strains arise from the loading-unloading sequence, both elasticity and

32
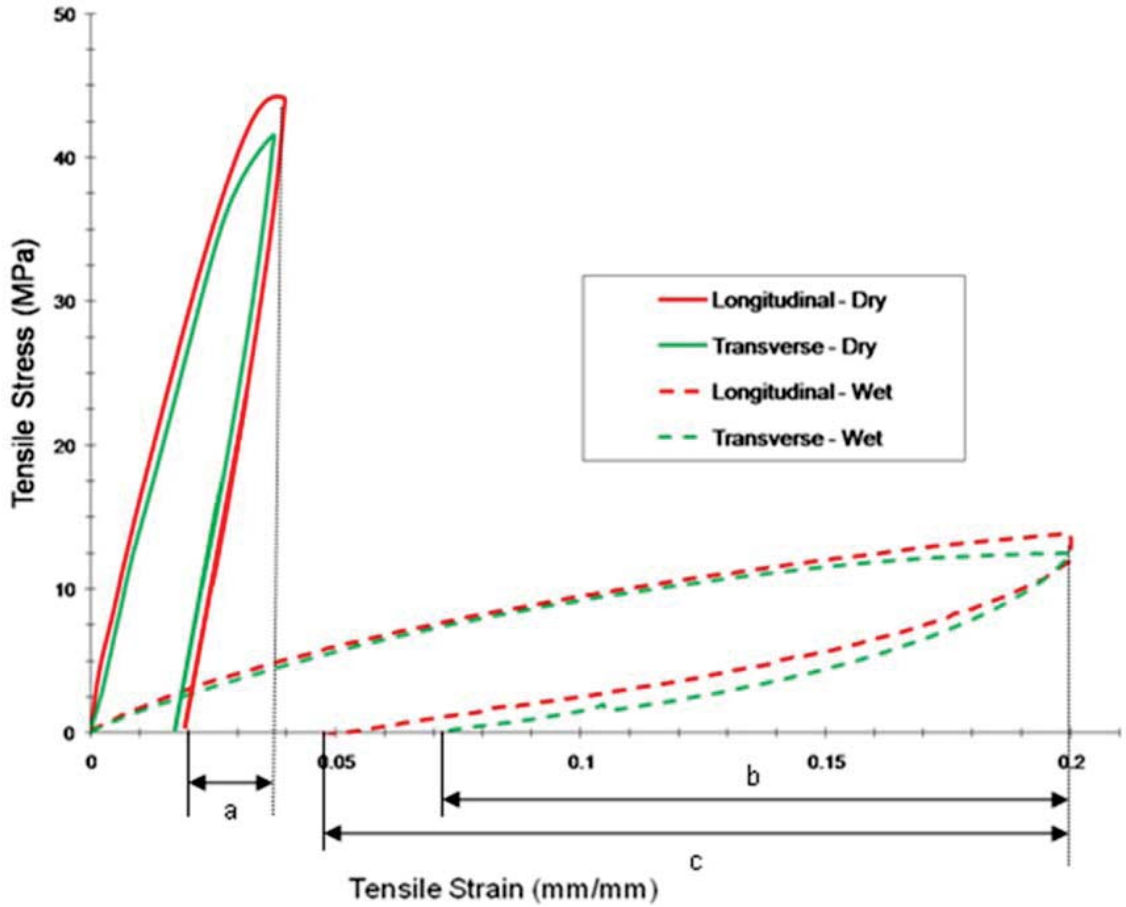
Figure 2.16   Longitudinal and transverse tensile stress-strain response with unloading for horn keratin in the wet (35 wt.% water) and dry (10 wt.% water) condition showing the inelastic strains for (a) dry horn keratin, (b) transverse – wet, and (c) longitudinal – wet horn keratin.

inelasticity have occurred upon the forward loading. From Figure 2.16, one can observe that in the dry condition for a total tensile strain of 4% that 2% of the strain was elastic and 2 % was inelastic. Hence, 50% of the total deformation was inelastic. For the wet conditions up to a tensile strain of 20%, the elastic strain ranged from 5 to 7.5% and the inelastic strain ranged from 12.5 to 15% for the longitudinal and transverse directions. Here, 60-75% of the deformation was inelastic. The inelasticity exhibited within the horn keratin under tension arose from the viscoplasticity of entangled molecular chains

33

inducing friction upon loading and also from the permanent damage that arose within the material near the failure strain, which finally led to fracture.

We also note that Figure 2.16 was used for the forward and unloading determination of the elastic modulus from our earlier discussion. As mentioned, the slope of the unloading curve generally provides a more accurate determination of elastic modulus since compliance of the testing machine is not a factor. The average longitudinal and transverse moduli obtained via unloading were measured as 4.0 GPa and 2.9 GPa, respectively, for the dry horn keratin. For the wet horn keratin, the longitudinal modulus was 0.5 GPa and the transverse modulus was 0.4 GPa. These values are in strong agreement with the moduli obtained via forward loading, indicating that the compliance of the machine did not affect the measurements.

Conclusions

The bighorn sheep (*Ovis canadensis*) horn keratin is adapted for excellent stiffness and strength under impact loading. When male bighorn sheep fight, their head-butts induce the largest impact forces among any other ram species. The combination of the horn spiral, the lessening of the mean diameter as the horn length is extended from the skull, the gradients of microstructure and associated mechanical properties from the horn's center to the outer radius all point to the stiffness and strength required for optimized impact resistance. Given the function of ram horn, a structure-property parametric study of bighorn sheep horn keratin was performed in order to quantify the influence of several factors believed to potentially affect the structure-property relations of horn. These factors included analysis of the stress-state dependence with the horn

34

keratin tested under tension and compression, the anisotropy of the material structure and mechanical behavior, the spatial location of the horn, and the wet-dry horn behavior.

The following conclusions can be made regarding this study:

- Horn keratin behaves in an anisotropic manner similar to a long fiber composite with strengthening fibers in a matrix in terms of the elastic moduli, strengths, and failure strains and mechanisms. However, the anisotropy is lessened as water is content is increased.

- The tubules serve to longitudinally stiffen the horn in tension and absorb energy in transverse compression.

- Water dominates the horn keratin material behavior more than the anisotropy, location on the horn, and the type of loading state. This makes moisture content the most relevant parameter in regards to influence on the mechanical behavior of horn keratin.

- A clear tension-compression asymmetry exists within the horn in which the tension stress-strain behavior exhibits a greater initial modulus that is exacerbated in the wet state. This early higher modulus in the tension curve leads to higher stress-states as a function of strain and eventual fracture sooner than compression.

- Tensile failure in the longitudinal direction occurred by matrix separation followed by fracture of the reinforcing tubules and some tubule pull-out. The ambient dry horn keratin failed in a much more brittle manner, while wet horn keratin was much more ductile.

35

- Tensile failure in the transverse direction occurred in wet horn keratin primarily because of matrix failure, with some transverse fiber pullout. However, ambient dry horn keratin exhibited delamination and tubule fracture.

- Compressive failure in the longitudinal direction occurred by shear microbuckling followed by delamination in both the wet and ambient dry conditions.

- Compressive failure in the transverse direction, both the wet and dry specimens exhibited a shear type failure mode.

CHAPTER III

GEOMETRIC EFFECTS ON ELASTIC STRESS WAVE MITIGATION

Introduction

Two motivations were the basis of the study presented in this chapter: the first comes from Einstein and the other from nature. In Kaku's (2004) book on Einstein's Cosmos, he discussed the guiding principle for The Theory of Relativity being the following: a geometry introduces an energy and an energy gives a force. Although Einstein was thinking of light, gravity, and the large scale cosmos, this principle was also a motivation for the present study. Another inspiration for this study stems from the curious geometries often found in biological structures that are subjected to dynamic loads. One such geometry is the natural spiral. A couple of examples of the appearance of the spiral in natural shock absorbing systems include the ram's horn and the woodpecker's hyoid. Does the reoccurrence of this curious shape throughout nature have some significance in regards to energy dissipation and shock absorption abilities inherent to its geometry? This is the question that we seek to answer. In other words, the question is: can geometries affect shock waves to change the energy states and in the end the forces (or stresses)?

Bio-inspired design has received a great deal of interest in recent literature - see for instance McKittrick et al. (2010) , Mohammed and Murphy (2009) , and Munch et al.

37

(2008). The bio-inspired design movement has prompted investigation into biological shock absorbing systems. The woodpecker's hyoid is one such system. This feature, not observed in other birds, aids the woodpecker in extending its tongue in order to evenly distribute incident mechanical excitations from drumming and to reinforce the head, i.e. the hyoid bypasses the vibrations generated from drumming (Sang-Hee and Sungmin 2011). Oda et al. (2006) used the finite element method (FEM) to show that the hyoid bone effectively protects the woodpecker's brain from shock damage. A similar study on the ram's horn is presented in Chapter 4.

The fundamentals of the physics of stress waves have been around a long time. Some recent references that discuss the history, capabilities, and phenomena include (Zukas et al. 1992, Zukas and Walters 1998, Meyers 1994). As a premise, it is worth summarizing the context of shock wave physics for this paper. If one were to neglect surface waves, then two main types of waves can propagate through elastic, isotropic solids: longitudinal waves and shear waves. Longitudinal (also called dilatational, pressure, primary, or P-) waves propagate with a characteristic wave speed and represent a volumetric change. Their motion is parallel to the direction of propagation of the wave. Shear (also called secondary, S-, or distortional) waves represent no volume change and propagate at a slower wave speed with respect to longitudinal waves. Their motion is normal to the direction of propagation (Davis 1988, Achenbach 1993). When either a longitudinal or shear wave impinges on a boundary, new waves are generated due to the reflective nature of waves. In a solid body with finite dimensions, these waves bounce back and forth between the bounding surfaces and interact with one another. These interactions can lead to wave amplification, cancellation, and other wave distortions.

38

The shock wave pressure can be integrated over time leading to the idea of an impulse. The impulse is equal to the change in momentum of the body. It is possible for a very brief force due to a shock to produce a larger impulse when compared to a smaller force acting over a much larger time period. Therefore, it is important to consider the transient forces, particularly those associated with shock phenomena.

The question remains then: how do the longitudinal and shear waves that arise from shocks induce associated pressures and impulses in different solid geometries? If Einstein's guiding principle of geometries creating energies and those energies creating forces is true, then we would expect to see different geometries admitting different pressures and impulses in a solid. The four geometries included in this study comprise a cylindrical bar, a tapered cylindrical bar, a spiral with a circular cross-section, and a tapered spiral (also with a circular cross-section). The cylindrical bar serves as a 'base-line' case. By comparing the response of the tapered cylinder to that of the uniform cylinder, we gain insight into how reducing the cross-sectional area influences the transient response of the structure. Similarly, comparison of the spiral geometry to the uniform cylinder leads to an understanding of the effects of increasing curvature on the wave propagation. Finally, analysis of the tapered spiral allows us to understand the coupled influence of increasing curvature and decreasing cross-sectional area on wave transients.

Although precious little has been studied on geometric shock waves in solids, some studies (mostly experimental and/or numerical since closed-form analytical solutions do not exist) have been performed on geometric effects on shock waves in gases. Setchell et al. (1972) conducted experiments with a conical converging geometry

39

that demonstrated a shock strengthening from the walls focusing the shock wave in air. Lind (1997) numerically studied shock waves with air in a cowl geometry illustrating that shock wave weakening could occur. Bond et al. (2009) conducted simulations employing an Eulerian framework and validated the simulations with experiments with a wedge design in carbon dioxide and nitrogen. The wedge was essentially a two dimensional linearly convergent geometry that focused the incoming shock repeatedly as multiple reflections increased the incoming pressure wave similar to the Setchell et al. (1972) results. Inoue (1993) numerically studied the geometry of a logarithmic spiral (log-spiral) duct to clarify the vortex formation behind the reflected shock wave in air. A purely computational approach employing finite element analysis has been chosen to study the wave propagation and reflection characteristics of these different geometric bodies. Finite element analysis is the most efficient technique to perform these types of studies and has become a widely accepted analysis tool (Hayashi, Song and Rose 2003, Demma et al. 2005, Gavric 1995, Treyssède 2008, Mace et al. 2005).

The purpose of this chapter is to show the geometric effects on shock waves transmitted through solid materials with an objective of garnering information for design of shock mitigating structures like those observed in nature. In particular two different geometric effects, a round tapered cone and a spiral, are presented with an analysis on the pressures and impulses. The following section describes the numerical methodologies and geometries employed. Subsequent sections show results, provide discussion, and draw conclusions based on the analyses.

Materials and Methods

Figure 3.1 depicts the four geometries that were studied along with the load and boundary conditions that were prescribed. The dimensions of each finite element model are provided in Table 3.1. The length and cross-sectional dimensions of each model were kept consistent. Also, the ratio of total length to cross-sectional diameter as well as the ratio of the large and small-end diameters was maintained among the four geometries, i.e. $L/d_1=10$ and $d_1/d_2=2$.

The finite element program ABAQUS/Explicit v6.10 (Dassault Systèmes - Simulia Corp.) was used as the numerical model in this study. Linear elastic material properties typical of steel were used; i.e. mass density, $\rho=7800$ kg·m^{-3}, Young's modulus, $E=207$ GPa, and Poisson's ratio, $\nu=0.3$. All geometries were meshed with 3-dimensional, 8-noded, continuum, linear, brick elements with reduced integration and hourglass control (C3D8R).

A ramped, compressive, pressure pulse was applied to the end of each bar as shown schematically Figure 3.1 and plotted in Figure 3.2. The peak amplitude and duration were set as $1 \cdot 10^5$ Pa and 38.8 μs, respectively. The relatively low pressure amplitude was chosen to ensure no departure from the elastic regime.

The nodes along the outer perimeter of the load-end were pinned ($u_1 = u_2 = u_3 = 0$) for each case. No additional constraints were prescribed. The resulting stress wave was allowed to propagate through the structure for 800 μs prior to terminating the calculation. To simplify future duplication of results, the ABAQUS input decks for each of the four geometries under investigation are provided in Appendix A.

41
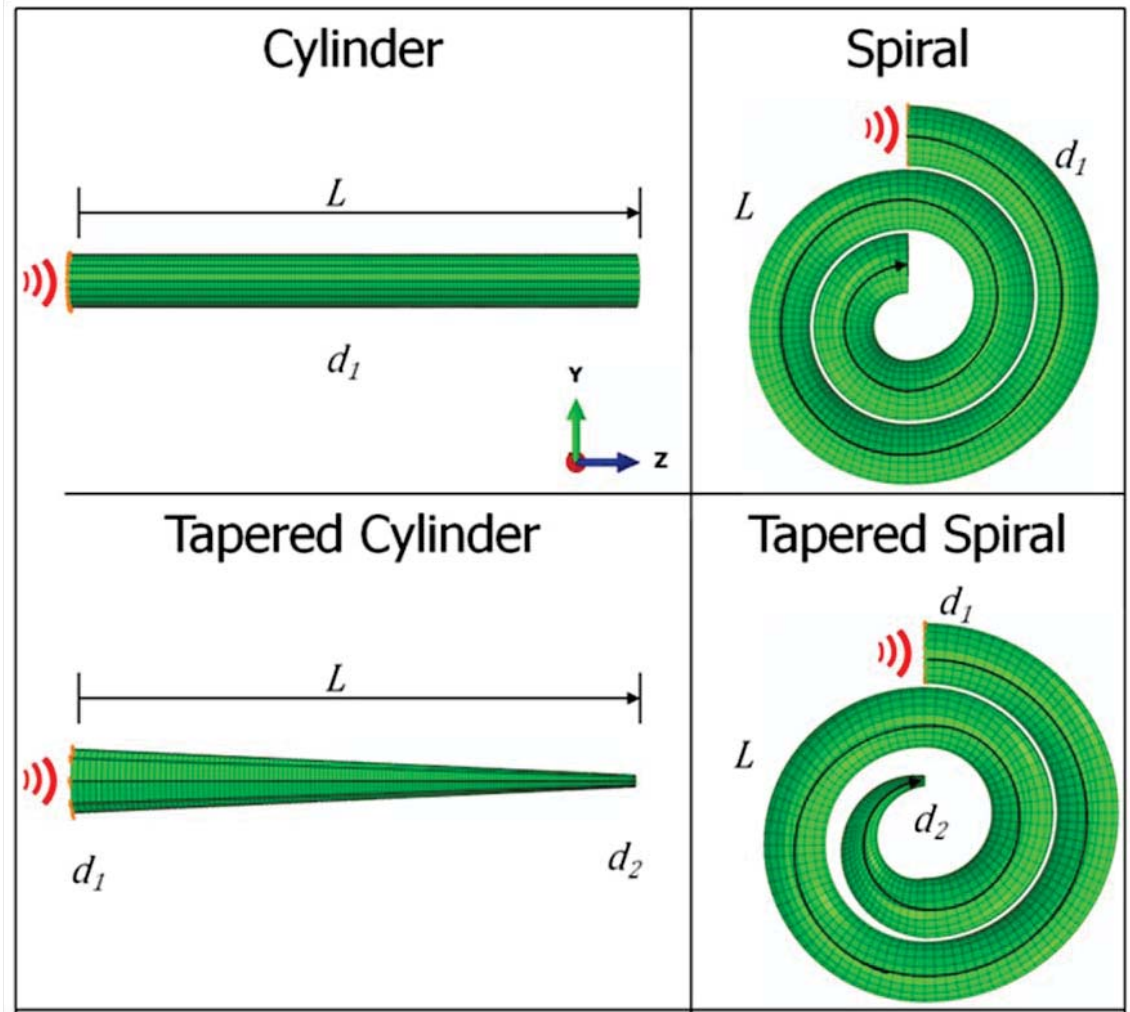
Figure 3.1   Schematic representation of the four finite element meshes illustrating the four different geometric configurations with the same length (and the same bar diameter where the pressure was applied) used in the analysis.

Post-processing of data was performed using ABAQUS/CAE v6.10 (Dassault Systèmes - Simulia Corp.). Wave propagation plots were generated by defining a path through each model that extended from the cross-sectional center of the fixed end to the cross-sectional center of the free end. Pressure and displacement response histories at the free-ends were generated by averaging the respective output of each node lying on the cross-section of the free end.

42
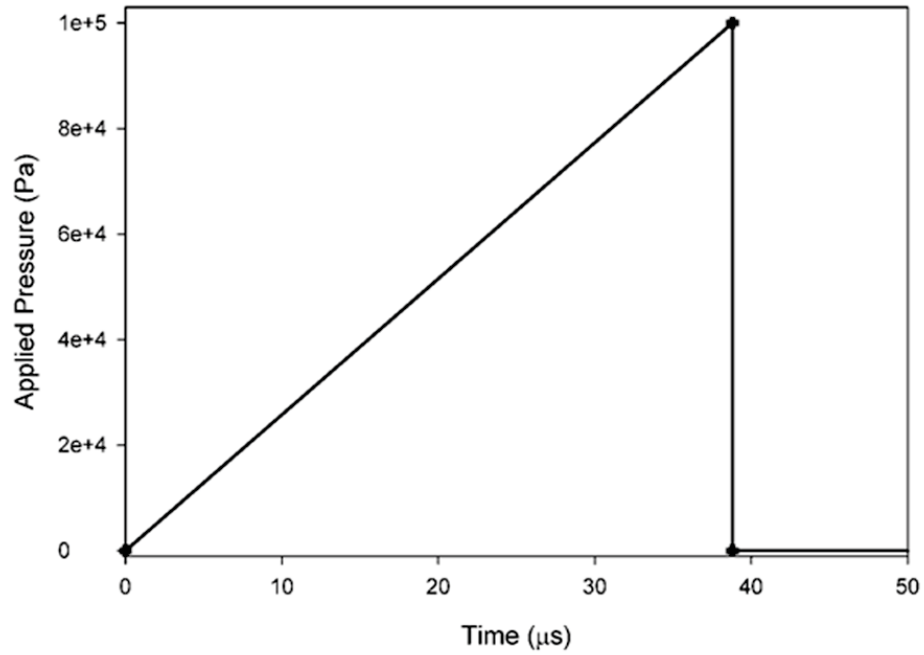
Figure 3.2   Ramped, pressure load history applied to fixed end of each geometry. The peak amplitude and duration are $1 \cdot 10^5$ Pa and 38.8 µs, respectively.

Results

The speed at which a longitudinal, elastic wave travels through a cylindrical, isotropic bar is given by:

$$c_L = \sqrt{E/\rho} \qquad (3.1)$$

where, E and ρ are the Young's modulus and mass density, respectively. Similarly, an elastic, shear wave travels through the same media at a speed given by:

$$c_S = \sqrt{G/\rho} \qquad (3.2)$$

where the shear modulus, G, is given by:

$$G = \frac{E}{2\ (1-\nu)} \qquad (3.3)$$

43

Table 3.1   Finite element model geometries and dimensions.

Geometry	Total Length, L (10^{-1} m)	Fixed-end Diameter, d_1 (10^{-2} m)	Free-end Diameter, d_2 (10^{-2} m)	Fixed-end Area, A_1 (10^{-3} m^2)	Free-end Area, A_2 (10^{-3} m^2)
Cylinder	7.04	7.04	7.04	3.89	3.89
Tapered Cylinder	7.04	7.04	3.52	3.89	0.97
Spiral	7.04	7.04	7.04	3.89	3.89
Tapered Spiral	7.04	7.04	3.52	3.89	0.97

Substitution of the typical steel values given above yields $c_L = 5.152 \cdot 10^3$ m/s and $c_S = 3.196 \cdot 10^3$ m/s. With the wave speed and length of the bar known, the time at which the wave strikes the free end can be easily calculated. The time it takes for the longitudinal wave to traverse the length of the uniform cylinder (L=0.704 m) is $t_L = 136$ µs. The time it takes the shear wave to travel the same distance is $t_L = 220$ µs.

Figure 3.3 shows the displacement contour and wave propagation plots for the cylinder, tapered cylinder, spiral, and tapered spiral. These plots illustrate that the displacement wave propagates differently through each of the geometries despite all the geometries having the same length and initial diameter. The plots for $t = 40$ µs show the displacement wave immediately following release of the applied pressure pulse. At $t = 104$ µs, the displacement wave is traveling through the structures in the $+Z$ direction. Because the primary and secondary waves travel at different speeds, at time $t = 184$ µs, the longitudinal wave has already reflected from the free end, but the shear wave has yet

44

to impinge upon the free boundary. And, at $t = 256$ µs, the reflected waves are traveling back toward the pinned end in the -Z direction.

Associated plots to Figure 3.3 are the pressure and the von Mises stress provided in Figure 3.4 and Figure 3.5, respectively. The pressure is related to the first stress invariant, which is also associated with the hydrostatic stress, where the von Mises stress is related to the second stress invariant, which is associated with shearing. When comparing the cylinder to the tapered cylinder, one might expect that the internal deformation, as reflected in the first two invariants, would be greater for the tapered geometry based upon those findings of a shock wave in a fluid (Setchell et al. 1972).

Figure 3.4 and Figure 3.5 indeed show that the tapered cylinder geometry induced greater hydrostatic and shear stresses as the dynamic wave propagated towards the small end of the bar. Hence, the focused deformation and associated stresses resulting from the convergent solid geometry played an important role in with this particular comparison.

If the deformation was an important factor in distinguishing between the cylinder and tapered cylinder, then one might expect to see the same trend for the spiral and the tapered spiral. However, Figure 3.4 and Figure 3.5 do not show this trend. But, for good reason: the dissipation of the wave from internal deformations, although important, does not have as much of an influence on the wave as the rigid free end displacements do. This is due to the transverse shearing loads inherent to the spiral geometry.

www.manaraa.com
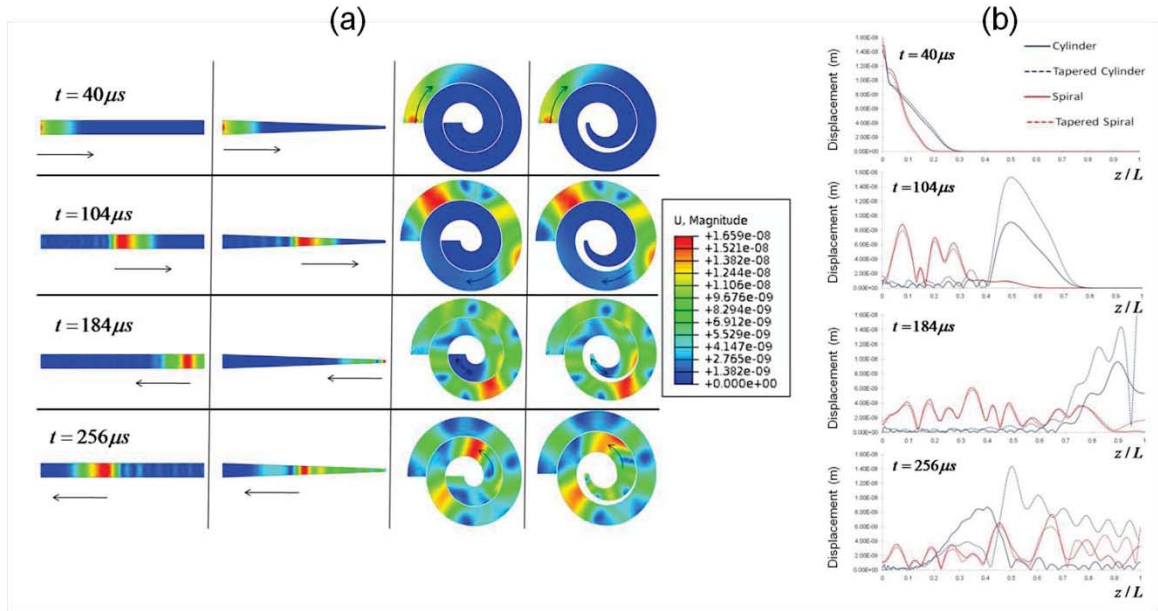
Figure 3.3   Displacement (a) contour and (b) wave propagation plots for $t = 40$ µs, $t = 104$ µs, $t = 184$ µs, and $t = 256$ µs.
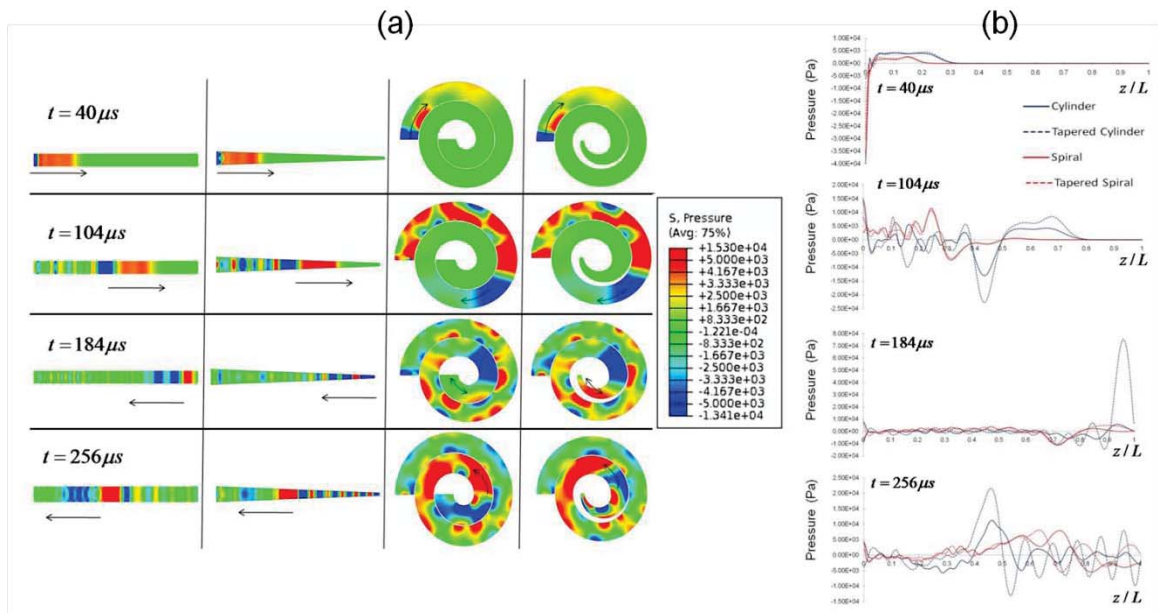
Figure 3.4   Pressure (a) contour and (b) wave propagation plots for $t = 40$ µs, $t = 104$ µs, $t = 184$ µs, and $t = 256$ µs.

46
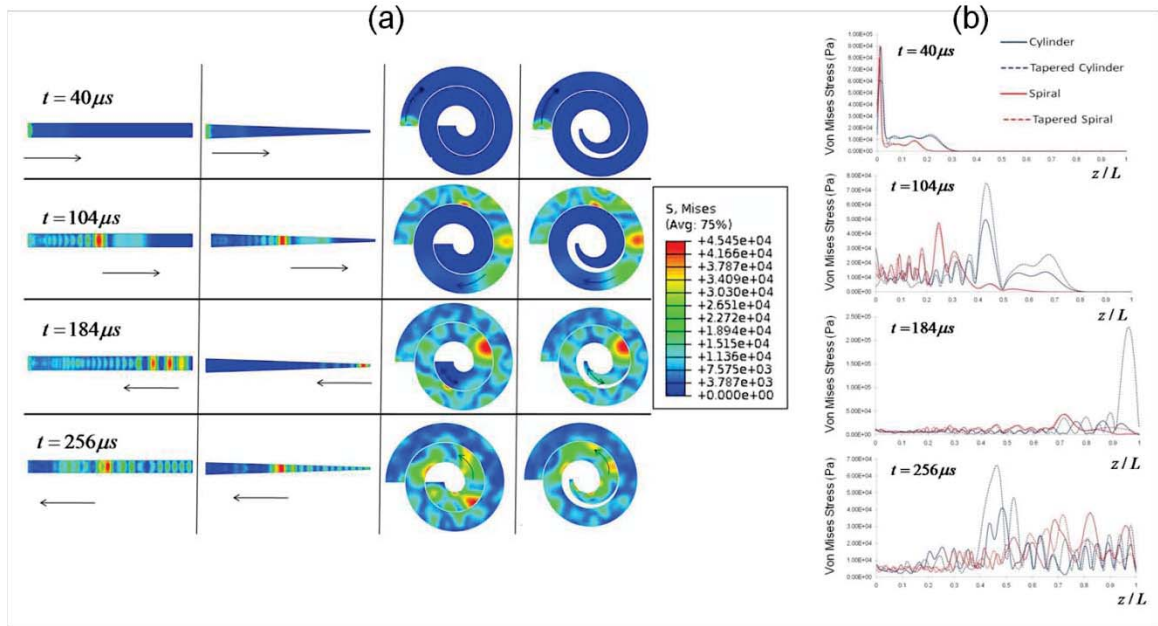
Figure 3.5   Von Mises stress (a) contour and (b) wave propagation plots for $t = 40$ μs, $t = 104$ μs, $t = 184$ μs, and $t = 256$ μs.

Figure 3.6 (a) shows the transverse displacements of the four geometries. There is an obvious, dramatic increase in transverse motion in the spiral case. On the lower abscissa, $\tau_L = t \cdot (c_L / L) = 1$ is the time at which the longitudinal wave first reaches the free end. The first and second reflected longitudinal wave arrive back at the free end at $\tau_L = 3$, and $\tau_L = 5$, respectively. Similarly, on the upper abscissa, $\tau_S = t \cdot (c_S / L) = 1$ corresponds to the time at which the shear wave reaches the free end and $\tau_S = 3$ represents the arrival of the reflected wave back to the free end. As shown in Figure 3.6 (a), the tapered spiral geometry incurred dramatically more transverse displacement than the spiral geometry with no taper. Furthermore, the cylinder and tapered cylinder geometries admitted negligible transverse displacements since only longitudinal stress waves were realized in those particular simulations. In contrast to the purely transverse displacements shown in

47
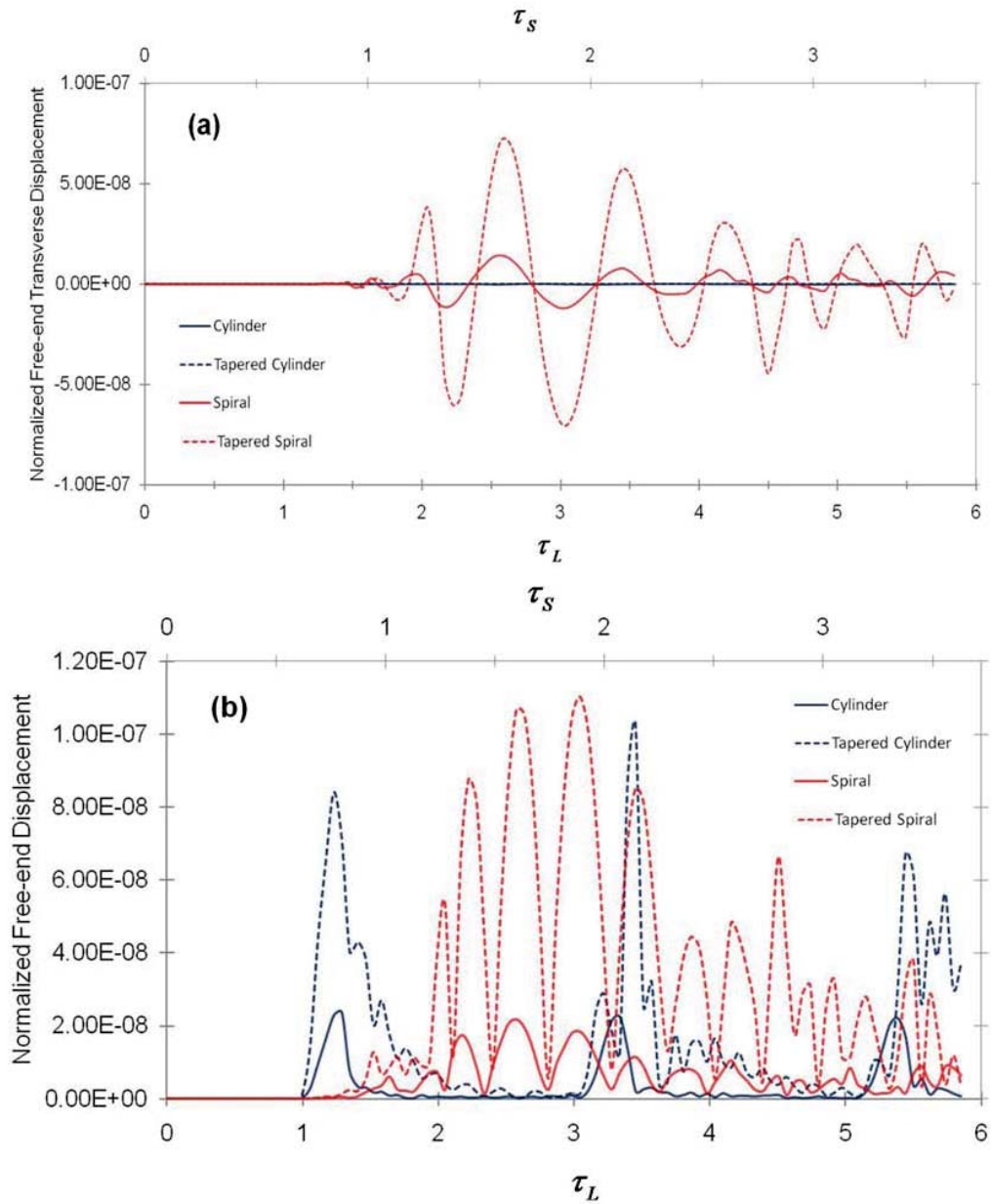
Figure 3.6   (a) Normalized free-end transverse displacement response and (b) total displacement response of a cylinder, tapered cylinder, spiral, and tapered spiral. On the lower abscissa, $\tau_L = t \cdot (c_L / L) = 1$ is the time at which the longitudinal wave first reaches the free end. The reflected longitudinal wave arrives back at the fixed end at $\tau_L = 2$ and so on. Similarly, on the upper abscissa, $\tau_S = t \cdot (c_S / L) = 1$ corresponds to the time at which the shear wave reaches the free end.

48
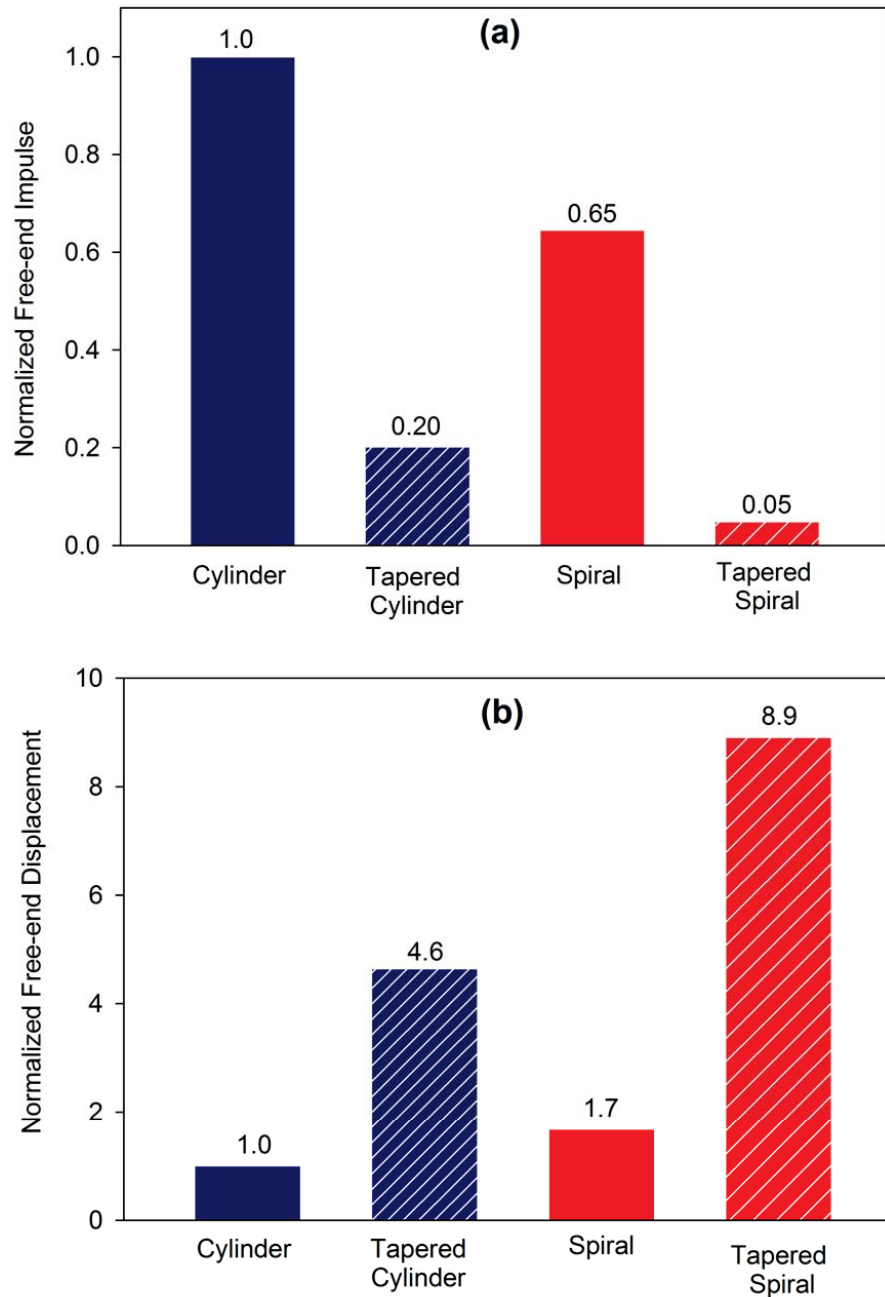
Figure 3.7   Normalized (a) impulse and (b) displacement at the free end. Impulse is found by multiplication of the free-end pressure history by the respective free-end area of each geometry followed by integration of the resulting force history (where negative values are neglected). Free-end displacement is taken as the area under the free-end displacement history curve. The free-end impulse and displacement values of the cylinder are used to normalize the results.

Figure 3.6 (a), the total free-end displacement responses for the four geometries are shown in Figure 3.6 (b).

Figure 3.7 (a) compares the normalized impulse at the free end. The impulse is calculated by multiplication of the free-end pressure history by the respective free-end area followed by integration of the resulting force history (where negative values are neglected. Figure 3.7 (b) is a comparison of the normalized free-end displacement. Free-end displacement is taken as the area under the free-end displacement history curve. The free-end impulse and displacement values of the cylinder are used to normalize the results and provide simple comparison. As clearly seen in Figure 3.7 (a), the cylinder admitted the greatest impulse throughout the wave motion and the tapered spiral best mitigated the impulse.

Discussion

If a designer were to choose a geometry to allow for the greatest transfer of the pressure and impulse based on the aforementioned simulations, then one would choose the cylinder, the most simple geometry. However, if the designer were to choose a geometry that allowed for the greatest dissipation of the pressure and impulse, then one would choose the tapered spiral. What caused the tapered cylinder to incur the greatest dissipation? Two things: first, the tapered geometry admitted greater internal deformations as the convergent boundary focused the pressure and it introduced some shear stresses and second, the spiral induced intense shearing that introduced fairly large transverse displacements.

50

Related to the impulse reduction let us first consider the aspect of time. If some of the geometries are introducing shear waves, although only longitudinal waves were initially introduced, then one might expect a difference in the timing of the wave impulses. Shear waves travel slower than the longitudinal waves. Therefore, when the waves arrive at the boundary at different times, dispersion and/or cancellation of the wave will result and a lower impulse near the free end of the rods will in turn arise. For the spiral geometries $t = 184$ µs was an interesting time, because the longitudinal wave reached the free end but the geometrically induced shear wave had not. The interaction of the longitudinal and shear waves at different times induced total dispersion of the waves that lowered the pressure and impulse.

From Figure 3.3, one can observe when comparing $t = 40$ µs and $t = 104$ µs for the cylinder and tapered cylinder that the wave travels through the cylinder and tapered cylinder at approximately the same velocity indicating that only minor shearing was introduced in the tapered cylinder. However, as time progressed, the wave in the tapered cylinder slowed down due to the focusing and the introduction of a shear wave. When the wave in the tapered cylinder reached the free end at $t = 184$ µs, the wave in the uniform cylinder had already reflected from the free end. When examining the wave speeds on the reflections, one can also see that the taper had already introduced the shear wave due to the slowness and also confirmed by examining the shear stresses within both of the geometries.

When comparing the impulses in Figure 3.7, clearly the tapered geometry introduced more mitigation than the spiral geometry but when both were introduced, a synergistic mitigation arose. Interestingly, in the tapered cylinder the longitudinal

51

displacement was magnified by the increasing uniaxial stress as the wave moved through the reduced cross-sectional area. However, the tapered cylinder did not introduce large transverse displacements like the spiral geometry. The introduction of the shear wave due to the spiral introduced the large transverse displacements and the shear stresses for the spiral geometry were much greater than those introduced by the tapered geometry. Consequently, when both the taper and spiral geometries were added together, the most shock mitigating geometry arose. One might expect even more mitigation in a three-dimensional toroidal (conical helix) geometry, like the ram's horn or woodpecker hyoid, since the other shear stresses would be introduced into the wave dispersion.

Conclusions

The following conclusions can be made regarding this study:

- A tapered geometry will lower the impulse due to the convergent boundary and a continually decreasing cross sectional area such that greater uniaxial stresses and subsequent axial deformation arises. Furthermore, the tapered geometry introduces small shear stresses that further decrease the impulse.

- A spiral geometry will lower the impulse due to the introduction of shear stresses along the length of the spiral. These shear stresses introduce transverse displacements that function to lessen the impulse.

- When both the tapered and spiral geometry are included in a design, their synergistic effects multiplicatively reduce the impulse.

CHAPTER IV

FINITE ELEMENT ANALYSIS OF A RAM IMPACT

Introduction

Bighorn sheep (*Ovis canadensis*) are among the most forceful fighting ram species (Geist 1971, Schaller 1977). During a typical ram fight, the two combatants back away from one another a good distance (up to 10 m (Welles and Welles 1961)) and charge at their opponent. In the last part of their charge, the ram stands on his hind legs, lowers his head, and clashes horns with his rival at full tilt (Schaffer 1968, Geist 1971). The impact is an awe-inspiring event. Even more remarkable is the fact that most of the time the animals sustain no injury from the dramatic head-on collision. The impact forces received during these sparring events are estimated to be at least 60 times greater than the impact forces necessary to cause fracture in a human skull (Gurdijian, Webster and Lissner 1949). The ram's ability to absorb such large amounts of energy without injury is intriguing. How (and where) all this energy gets dissipated is not fully understood.

When a ram receives a blow to the horns, a sudden increase in stress arises at the impact location. This stress then propagates through the horns to the rest of the skull and body of the animal in the form of stress waves. The intensity of the stress waves resulting from an impact as extreme as those sustained by fighting rams is undoubtedly large enough to significantly damage something as delicate as a brain. Therefore, the stress

53

wave must be somehow dissipated and/or concentrated away from the fragile brain tissue to prevent injury or death.

A ram's head contains several candidate features that could serve shock absorbing functions. Sheep craniums contain several suture lines located near the horns. These sutures are a type of joint between the plate-like skull bones. Jaslow and Biewener (1995) showed that these sutures drop the strain levels up to 50%, when traversing across the two mating cranial bones under impact loading. Hence, the cranial sutures certainly contribute to the energy absorption in the goat's skull, acting somewhat like a spring and damper system to allow cranial bone movement. However, the magnitude of that contribution is most likely a small one, because the cranial sutures are only allowed to expand or contract a few microns at best, while total head displacements are a few millimeters (three orders of magnitude more displacement).

Another shock absorbing component in the ram's head is the large frontal sinus system. The rostrum of the ram's skull is full of seemingly oversized cavities. It has been hypothesized that these hollow spaces function to insulate the brain from shock damage. Farke (2008) tested this hypothesis using finite element analysis (FEA) models with a varying morphology, i.e. impact was simulated on FEA models with various sinus morphologies as well on models with the sinus cavities completely removed. The results of study by Farke (2008) were only partially consistent with the hypothesis that the sinus system acts as a shock absorber leading to his conclusion that the large cavities are most likely due to the removal of mechanically unnecessary bone. Farke (2008) went on to hypothesize that the keratinous horn sheaths probably played a larger role in dissipating

54

the impact energy experienced by head-butting rams. The present study tests this hypothesis.

Horn keratin is the outermost constituent of the horn and is the material that actually suffers the impact blow. Horn keratin has been shown to be a very tough material, capable of absorbing large amounts of energy (McKittrick et al. 2010, Tombolato et al. 2010). Like most other biological materials, the mechanical properties of horn keratin are dependent on many factors, e.g. moisture level, age, stress-state, temperature, loading direction, and so on. Furthermore, living materials are in a constant state of flux, constantly rebuilding and adapting to their environment. The material 'constants' in biological materials are in reality not constant at all. However, moisture content has been shown to be the dominant parameter in regards to influencing the mechanical behavior of horn keratin (Trim et al. 2010). To make the problem more tractable, we focus this study primarily on the effects of horn keratin moisture (two moisture states: wet and dry) with regards to choosing the material parameters.

The horn keratin grows from a thick layer of germinative epithelium (here referred to as skin) (O'Gara and Matson 1975, Kitchener 1991). This skin layer is sandwiched between the keratin sheath and the bony horn core. Skin is often overlooked as a shock absorbing component in a ram's head. However, skin is the most compliant material in the head (neglecting the cranial organs of course), which leads to the notion that the skin is able to sustain elastic deformations orders of magnitude greater than the very stiff cranial bone. Materials capable of sustaining large elastic deformation are generally very tough. Therefore, the skin that separates the bony core from the horn keratin could certainly play a role in dissipating some of the impact energy.

55

Another plausible contributor to the shock being absorbed in a ram's head is the geometry of the horns themselves. The tapered spiral shape of the horn is curious and is found in other shock absorbing natural structures such as the woodpecker hyoid (Sang-Hee and Sungmin 2011). Does this curious geometry play a role in protecting the delicate cranial organs? The study in Chapter 3 showed that a tapered spiral will indeed reduce the total impulse when compared to a solid cylindrical geometry by up to 80%. Chapter 3 focused on two dimensional studies of steel; to further this effort, we test the functional effects of the horn geometry by simulating a ram's head impact using finite element analysis (FEA) with horns and with the horns digitally removed.

In this chapter, FEA is used to simulate a dynamic head-butting impact of a bighorn sheep. Emphasis is placed on the contributions of the moisture content of the horn keratin and the horn geometry to the overall shock absorbing ability of the system. Four FEA models are used: 1) a bighorn sheep head with horns and dry horn keratin, 2) a bighorn sheep head without horns and dry horn keratin, 3) a bighorn sheep head with horns and hydrated horn keratin, and 4) a bighorn sheep head without horns and hydrated horn keratin. To our knowledge, these are the first three dimensional, explicit finite element simulations of a ram's head impact.

FEA Model Generation

A ram's skull with a horn keratin layer still attached was obtained from Skulls Unlimited, Inc. The skull was scanned using computed tomography (CT) with a 0.625 mm in-plane pixel resolution and inter-slice spacing of 1.25 mm. The digital CT slices were then imported into the MIMICS (Materialise, Inc.) software, which was used to

56

discretize the geometry. The digital head model was then separated into three material sections based on CT gray scale values.

The three materials were identified as horn keratin, bone, and skin. Keratin comprised the outermost part of the horns, covering them like a sheath. The cranium was composed of bone. Bone also extended through ~2/3 the length of each horn. Sandwiched between the horn keratin and bone was a layer of epithelium from which the keratin grew.

To investigate the effects of the horn geometry, the original finite element model (FEM) was used to a construct another model. The horns were digitally severed about 80 mm away from their base using HyperMesh (Altair Engineering, Inc.) software. The original FEM and the model with the horns removed are shown in Figure 4.1.

The meshes used eight node brick (C3D8) elements. The final mesh of the FEM with horns consisted of 847,809 nodes and 673,059 elements. The mesh of the FEM without horns comprised 309,834 nodes and 246,233 elements. The average element volume was 8×10^{-3} mm^3. Owing to the size and complexity of the models, it was not feasible to perform mesh density convergence tests. The final meshes were exported to the preprocessing software ABAQUS/CAE (Dassault Systèmes - Simulia Corp.) which was used to assign boundary and loading conditions, and assign material and time step parameters.

A fixed time increment of 5×10^{-6} s was found to produce stable results. The total time period of each simulation was 1 s, so each simulation contained 2×10^5 time steps. The default linear bulk viscosity parameter (0.06) was used, while the quadratic bulk viscosity parameter was set to zero for each case. Field and history output were requested

57

at 0.05 s increments. Each problem was decomposed into 24 parallel domains and ran on 24 Intel 2.8-GHz Westmere processors using 48 GB of memory. Each simulation required about 12 hours of computational time.
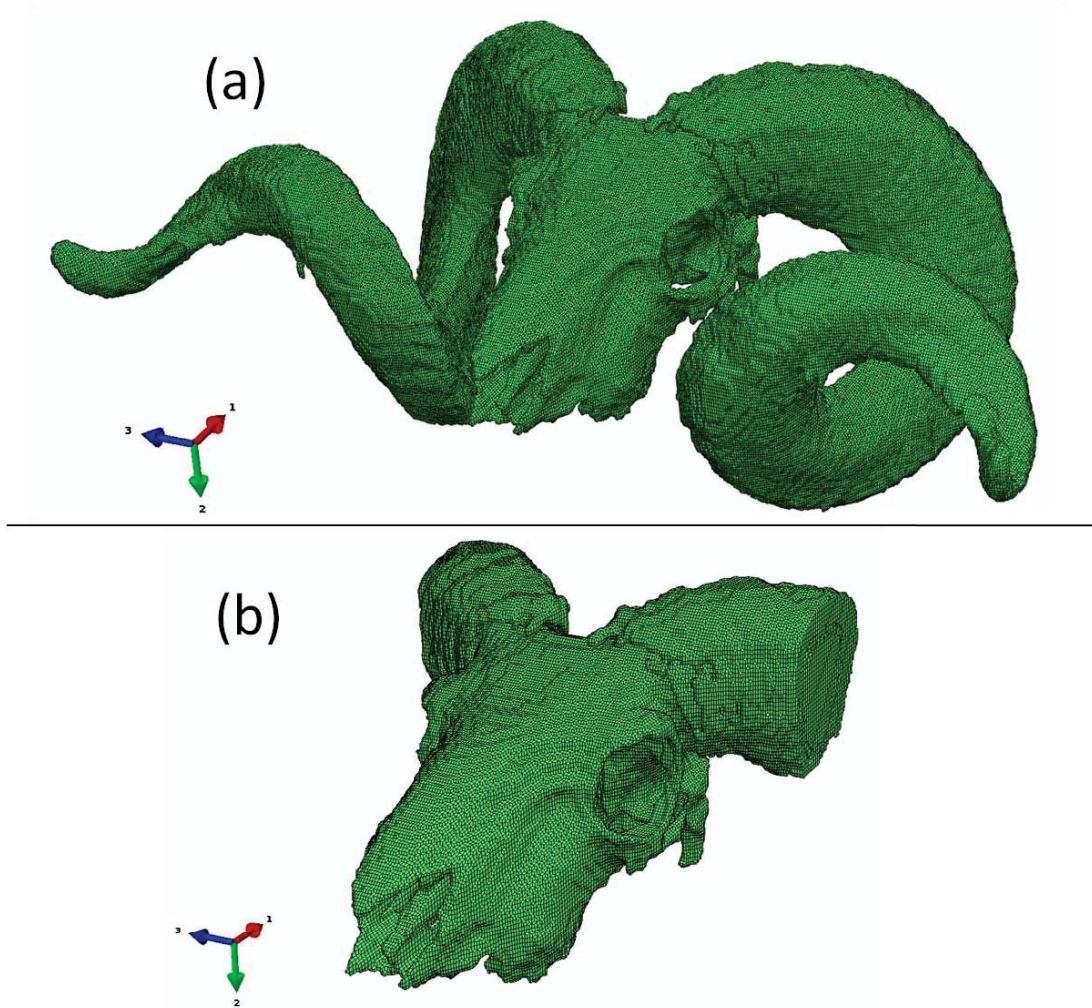
Figure 4.1   Finite element model of ram head (a) with horns and (b) with horns removed.

Boundary and Loading Conditions

The loading data for the simulations were adapted from film analysis of bighorn sheep fights performed by Kitchener (1988). The peak deceleration was measured as

$a = \cdot 34$ m s^{-2} (Kitchener 1988). Using the average ram's body mass, $m = 100$ kg (Geist 1971), Newton's second law $(F = ma)$ provides the maximum sustained force, $F_{max} = 3400$ N. This force was converted to a pressure load by distributing it over approximately 100 nodes on the anterior keel of each horn sheath, a typical impact location (Schaller 1977). The corresponding area was $A = 2,200$ mm^2. The peak pressure amplitude was given by $P_{max} = F_{max} / A = 1.7$ MPa. The duration of impact, also estimated from Kitchener's (1988) data, was 200 ms. Since the deceleration linearly increased over the impact duration, a linearly increasing (ramped) pressure pulse was used. The applied pressure pulse is plotted in Figure 4.2.
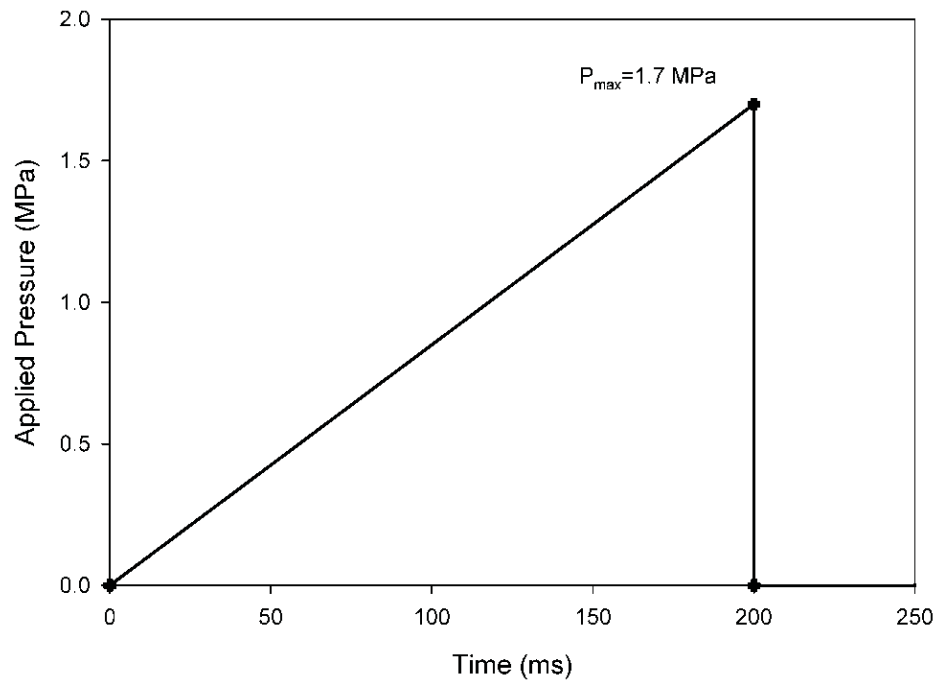
Figure 4.2   Applied pressure pulse used in all finite element simulations.

59

Surface-based tie constraints were used to join each material section, i.e. the inner surface of the horn keratin was tied to the outer surface of the skin and the inner surface of the skin was then tied to the outer surface of the bony horn core.
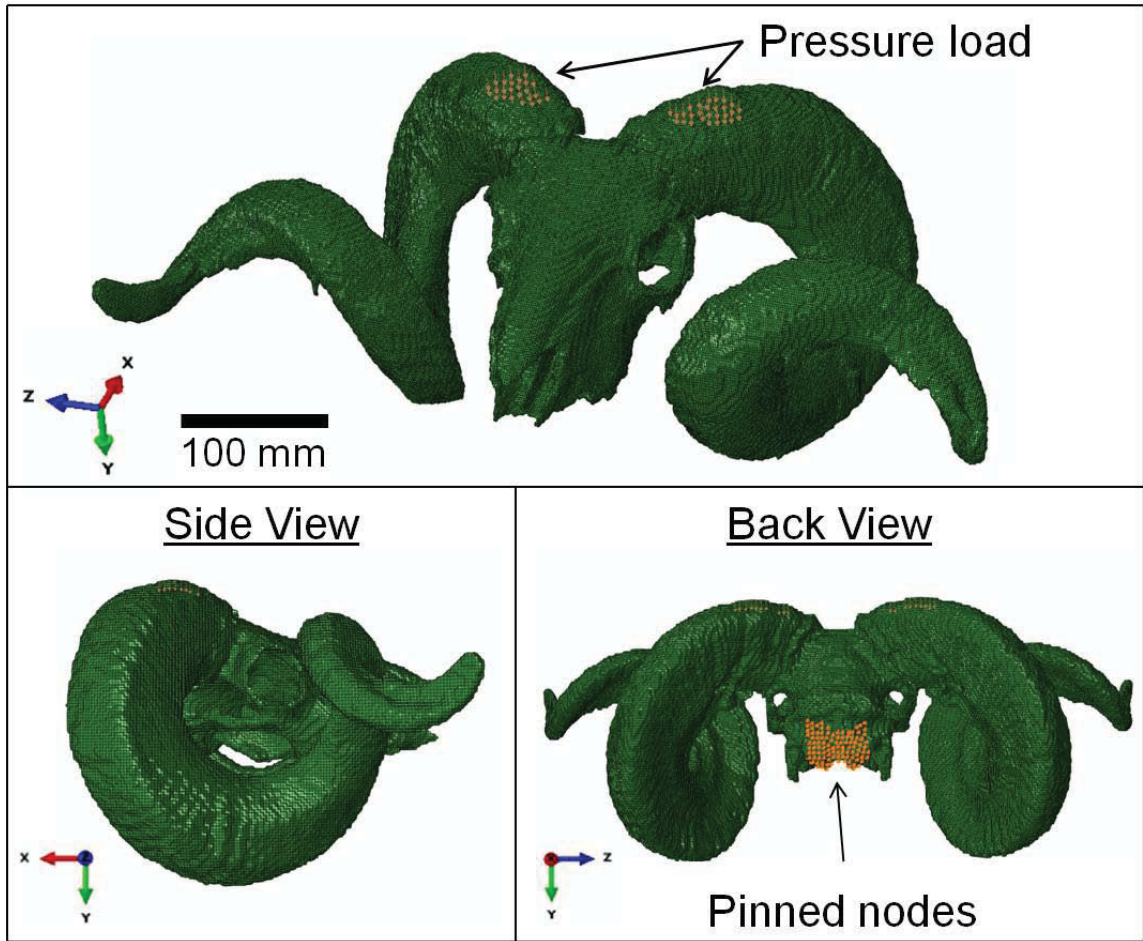
Figure 4.3   Finite element model of ram head showing load and boundary conditions. The model where the horns were removed is loaded and constrained at the same locations as the full model including the horns shown here.

Additional boundary conditions were assigned to the area at the base of the skull representing the location where the skull would attach to the spine and neck musculature of the animal. The surface nodes corresponding to this area were pinned (free to rotate

60

but not translate), i.e. $u_1 = u_2 = u_3 = 0$. The FEA model of the ram skull with boundary and loading conditions is shown in Figure 4.3.

Constitutive Modeling

      The constitutive modeling procedures for the three materials comprising the FEA model (bone, horn keratin, and skin) are outlined below. The constitutive model used for each material, the associated parameters, and data sources are listed in Table 4.1. The experimental stress-strain behaviors for the various materials and model calibrations are shown in Figure 4.4. Justification for the modeling techniques and chosen parameters are outlined for each material in the following subsections.

Table 4.1   Material models and associated parameters used in finite element analyses. E is Young's modulus, ν is Poisson's ratio, ρ is mass density, α is a strain hardening exponent, μ is shear modulus.

Material	Model	Model Parameters	Reference
Horn Keratin			
Dry	Linear	ρ=1.3 g·cm^{-3}, E=3.5 GPa, ν=0.3	Trim, et al.(2010)
Hydrated	Marlow	ρ=1.3 g·cm^{-3}, uniaxial test data	Trim, et al.(2010)
Bone	Linear	ρ=1.8 g·cm^{-3}, E=20 GPa, ν=0.3	Currey (2002)
Skin	Ogden	ρ=1.3 g·cm^{-3}, α=3.5 GPa, μ=2.2MPa	Shadwick, et al.(1992)
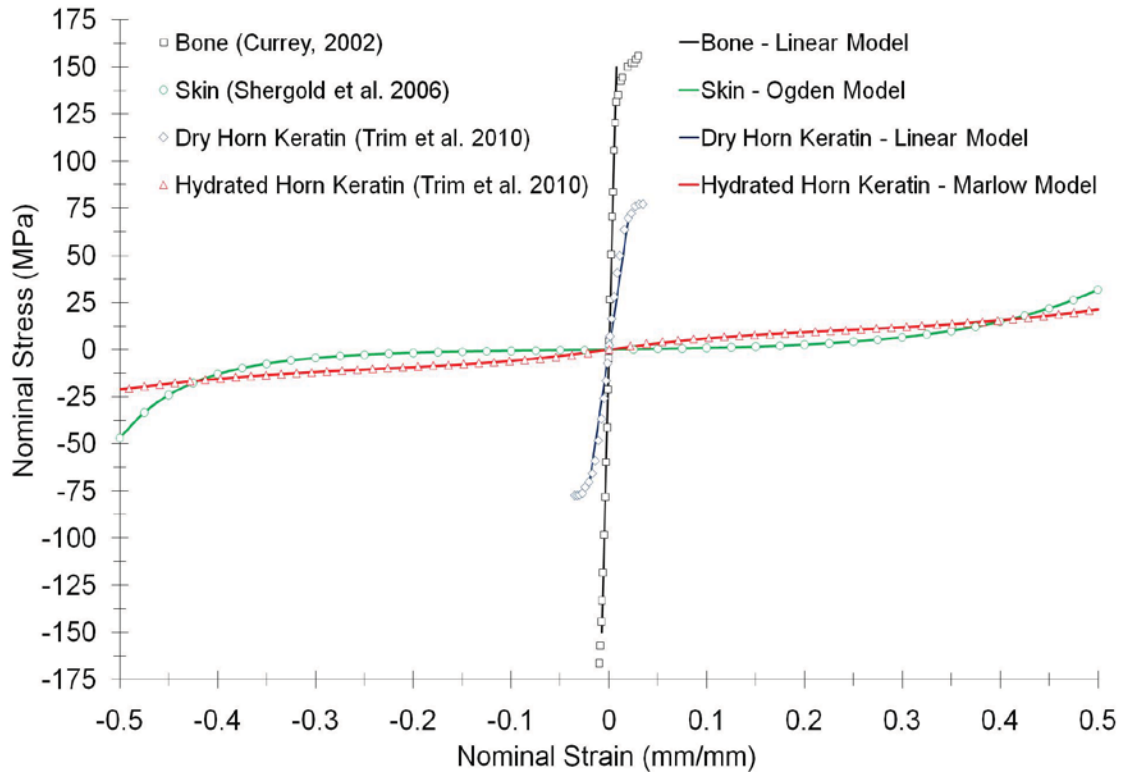
Figure 4.4   Nominal stress-strain response and model predictions for bone, skin, dry horn keratin, and hydrated horn keratin. Negative values indicate compression and positive values indicate tension.

Constitutive Modeling of Bone

Bone is significantly stiffer than the other constituent materials of the head. Because of its rigidity, it experiences relatively little strain upon loading. During *in vitro* impact loading, Jaslow and Biewener (1995) measured maximum tensile and compressive strains in goat's skulls to be about 7×10^{-4} and 2×10^{-3}, respectively. The compressive and tensile stress-strain response of bone is linear up to about 7×10^{-3} strain (Currey 2002). Therefore, a linear elastic assumption for the bone material was assumed in our calculations. This assumption makes defining the constitutive response of bone straight forward, requiring only three material parameters: mass density, ρ, Young's

modulus, *E*, and Poisson's ratio, *v*. The parameters for cranial bone are $\rho = 1.8$ g cm^{-3}, $E = 20$ GPa, $v=0.3$ (Currey 2002). This is also consistent with many FEA results, assuming linear elastic behavior for cranial bone, that have been validated through experimental data, e.g. (Farke 2008, Chafi, Karami and Ziejewski 2010, Willinger, Kang and Diaw 1999).

In reality, bone is slightly viscoelastic and its stiffness is dependent to some extent on the strain-rate. Currey (1988, 2002) asserted that bone is not markedly strain-rate dependent and notes that a thousand-fold increase in strain rate results in only about a 40% increase in stiffness. The properties of bone are also slightly dependent on moisture level, age, stress-state, temperature, loading direction, and so on. Furthermore, living materials are in a constant state of flux, rebuilding and adapting to their environment. This makes the choice and applicability of the property data (and model to fit it) all the more difficult.

Constitutive Modeling of Horn Keratin

Moisture content has been shown to be a dominant parameter in regards to influencing the mechanical behavior of horn keratin (Trim et al. 2010). Water makes the horn keratin less susceptible to damage (Vincent 1990) and also increases its toughness (Trim et al. 2010, Kitchener 1987b). To understand the extent to which the moisture dependence affects the overall response of the ram's skull during impact, separate simulations were performed using mechanical property data for dry (10 wt.% water) and hydrated (35 wt.% water) horn keratin, which were taken from Trim, et al. (2010). Vincent (1990) stated that fresh horn keratin contains about 20 wt.% water. However, the actual moisture content of horn will vary depending on environmental conditions. So, the

dry and hydrated horn keratin data provide limiting bounds. The response of fresh horn keratin would fall between these two extreme cases.

As seen in Figure 4.4 Nominal stress-strain response and model predictions for bone, skin, dry horn keratin, and hydrated horn keratin. Negative values indicate compression and positive values indicate tension.

Dry horn keratin behaves as a brittle material, showing little ductility prior to fracture. The initial stress-strain response of dry horn keratin is linear elastic. The Young's modulus of dry horn keratin is 3.5 GPa, the Poisson's ratio is 0.3, and the mass density is $\rho = 1.2$ g cm^{-3} (Trim et al. 2010). These three material parameters adequately define the response of dry horn keratin assuming a linear elastic, isotropic, homogenous material.

The stress-strain behavior of hydrated horn keratin is a bit more complex. When hydrated, horn keratin behaves like a hyperelastic material, as observed in Figure 4.4. Hyperelastic constitutive models use a strain energy potential function to define the strain energy density stored in the material in terms of the strain at that point in the material. Constitutive modeling of hydrated horn has never been performed, so several hyperelastic models, e.g. Ogden (1972), Arruda-Boyce (1993), Marlow (2003), Mooney-Rivlin (1940, 1948), were tested to determine which produced the best curve fit. The best model correlation to the experimental data was found using the Marlow (2003) model included in ABAQUS (Dassault Systèmes - Simulia Corp.). The form of the Marlow (2003) strain energy potential, ϕ, is defined as:

$$\phi = \phi_{dev}(\bar{\lambda}_1^2, \bar{\lambda}_2^2, \bar{\lambda}_3^2) \tag{4.1}$$

64

where ϕ_{dev} is the deviatoric part of the strain energy per unit of reference volume, the deviatoric stretches, $\bar{\lambda}_i = J^{-1/3} \lambda_i$, with J being the total volume ratio. The use of the Marlow model does not require input of parameters; the model is instead implemented using uniaxial test data. The experimental response of hydrated horn keratin and the fit provided by the Marlow model is shown in Figure 4.4.

Constitutive Modeling of Skin

Because mechanical property data for germinative epithelium (here referred to as 'skin') in bighorn sheep does not exist, the properties for porcine skin were substituted. Shergold et al. (2006) measured the compressive response of porcine skin at various strain rates and found that a one-term Ogden strain energy density function adequately described the measured response. For an incompressible, isotropic, hyper-elastic solid, the Ogden (1972) strain energy potential is the following:

$$\phi = \frac{2\mu}{\alpha^2}(\lambda_1^\alpha + \lambda_2^\alpha + \lambda_3^\alpha - 3), \tag{4.2}$$

where ϕ is the strain energy density per unit of reference volume, μ is the shear modulus, α is a strain hardening exponent, and λ_i are the stretch ratios in the three principal directions. The Ogden constants for porcine skin for a medium strain rate $(\dot{\varepsilon} = 40 \text{ s}^{-1})$ are $\alpha = 12$ and $\mu = 2.2$ MPa (Shergold et al. 2006). The mass density of skin is $\rho = 0.9$ g cm^{-3} (Shadwick et al. 1992). The comparison of the experimental stress-strain behavior and the Ogden model correlation for skin are shown in Figure 4.4.

65

Simulation Results

A path was defined to track the von Mises stresses, hydrostatic pressure, and displacement from the point of impact to the brain cavity in each of the four models. The path (shown in Figure 4.5) originates at the surface node on the left horn in the middle of the region where the pressure load was applied. The pathway followed the shortest straight line route from the point of impact to the brain.
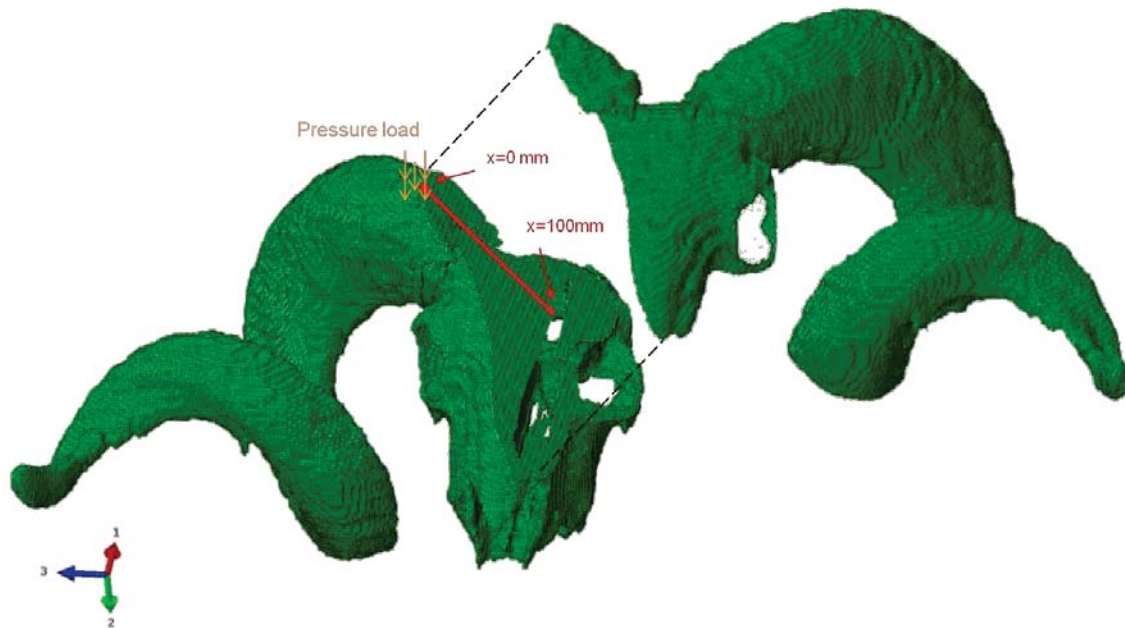
Figure 4.5   Exploded view of finite element model showing path along which von Mises stress, hydrostatic pressure, and displacement are measured. The pathway follows the shortest straight line route from the point of impact on the left horn (x=0 mm) to the brain cavity (x=100 mm). The path traverses ~32 mm of horn keratin, ~23 mm of skin, and ~45 mm of bone.

The path traversed the horn keratin, skin, and bone until it finally terminated at the brain cavity. The total length of the path was ~100 mm, the first ~32 mm was through the horn keratin, the next ~23 mm traversed the skin, and the last portion of the path passed through ~45 mm of bone. The values for the von Mises stress, hydrostatic

66

pressure, and displacement along this path are plotted in Figure 4.6, Figure 4.7, and Figure 4.8, respectively.

Figure 4.9 (a) shows force magnitude versus time at the tip of the horn. For the models with horns attached, force and displacement were measured at 50 nodes laying on the same cross-sectional plane at the tip each horn and then averaged. For the models where the horns were removed, force and displacement measurements were taken at 50 nodes on the cross section where the cut was made (~80mm from the base of the horn) and then averaged. The same technique was used to generate Figure 4.9 (b), which shows the average displacement magnitude of those same nodes.

Figure 4.10 compares the impulse at the horn tip for the FEA models with and without horns using dry and hydrated horn keratin. The impulse is the integral of force with respect to time, i.e. the area under the force-time curve. The impulse for the models with horns was calculated as 0.23 N·s for the model with dry horn keratin and 0.75 N·s for the model with hydrated horn keratin. The impulse for the models where the horns were removed was 3.9 N·s for the model using dry horn keratin and 2.0 N·s for the hydrated horn keratin model.

The strain energy versus time for the four simulations is plotted in Figure 4.11. Strain energy was calculated by multiplying the total strain energy density output from ABAQUS (Dassault Systèmes - Simulia Corp) by the respective volume of the model, which was determined by the summation of the volume of every element in the model. The FEMs with horns and without horns had a total volume of $3.21 \cdot 10^6$ mm^3 and $1.17 \cdot 10^6$ mm^3, respectively.

67
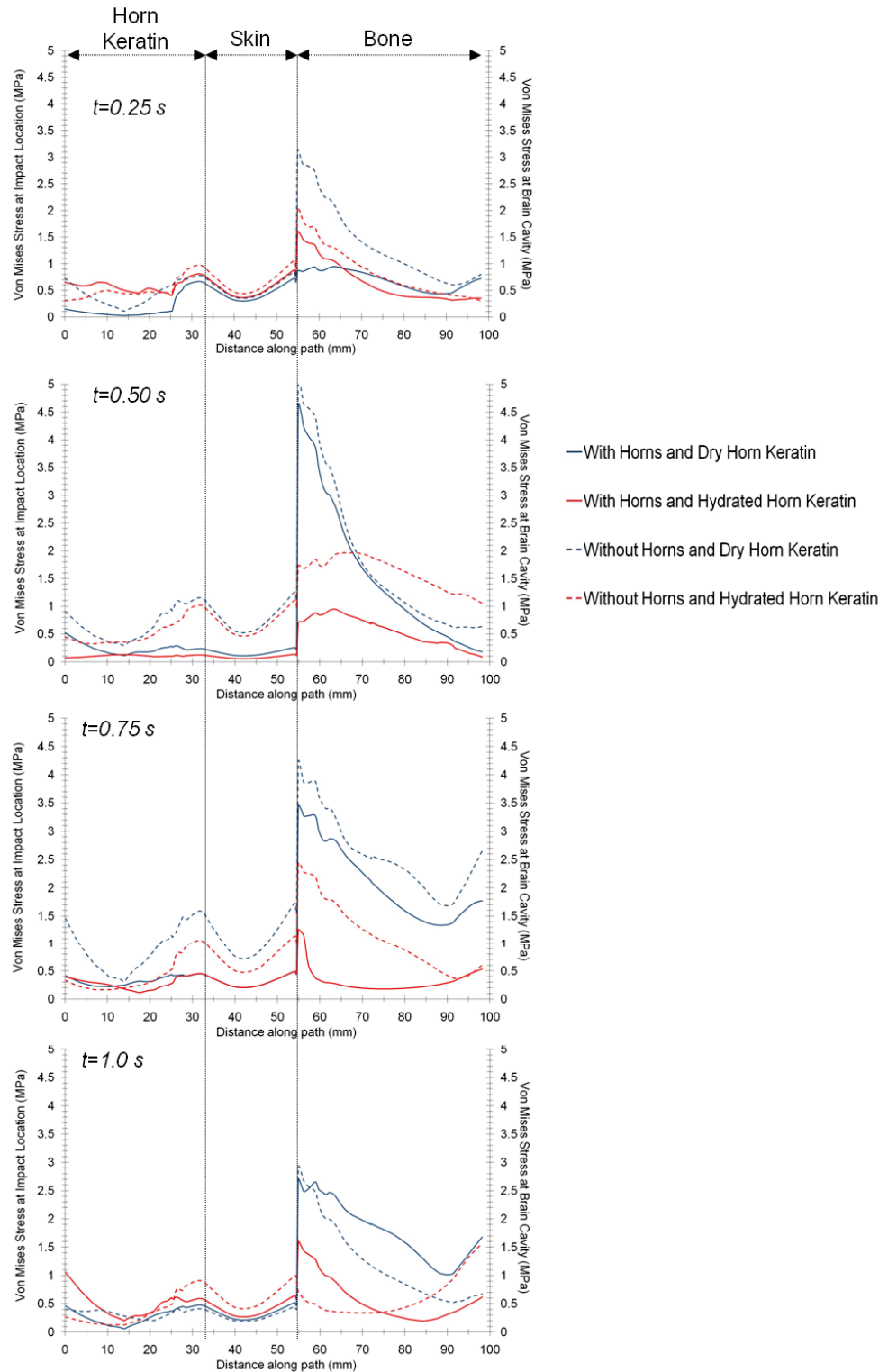
Figure 4.6   Plots of von Mises stress along the path originating at the point of impact on the left horn (x=0 mm) and terminating at the brain cavity (x=100 mm) at times t=0.25 s, t=0.5 s, t=0.75 s, and t=1.0 s.

68
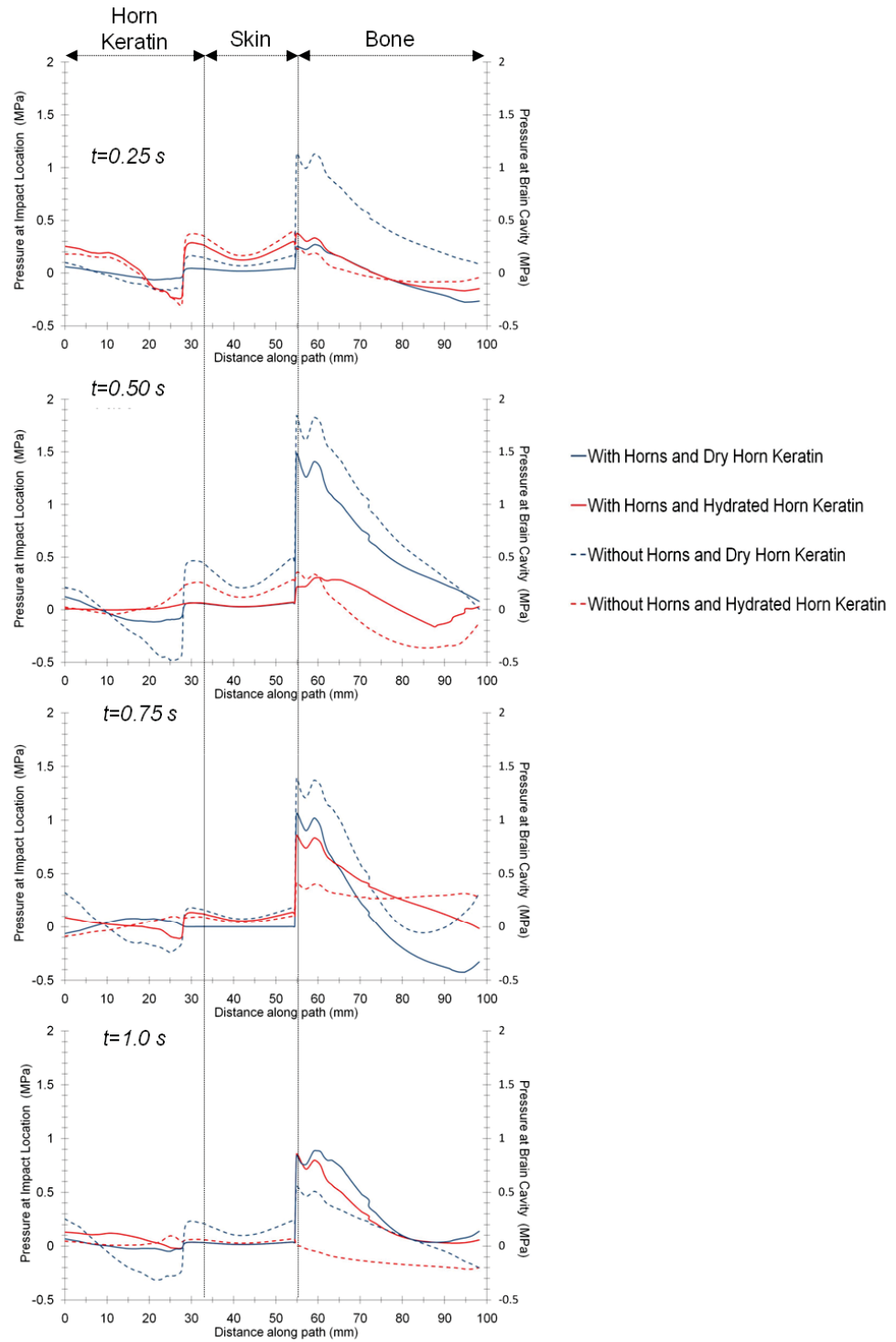
Figure 4.7   Pressure plots at times t=0.25 s, t=0.5 s, t=0.75 s, and t=1.0 s along the path originating at the point of impact on the left horn (x=0 mm) and terminating at the brain cavity (x=100 mm). Positive and negative values indicate compression and tension, respectively.

69
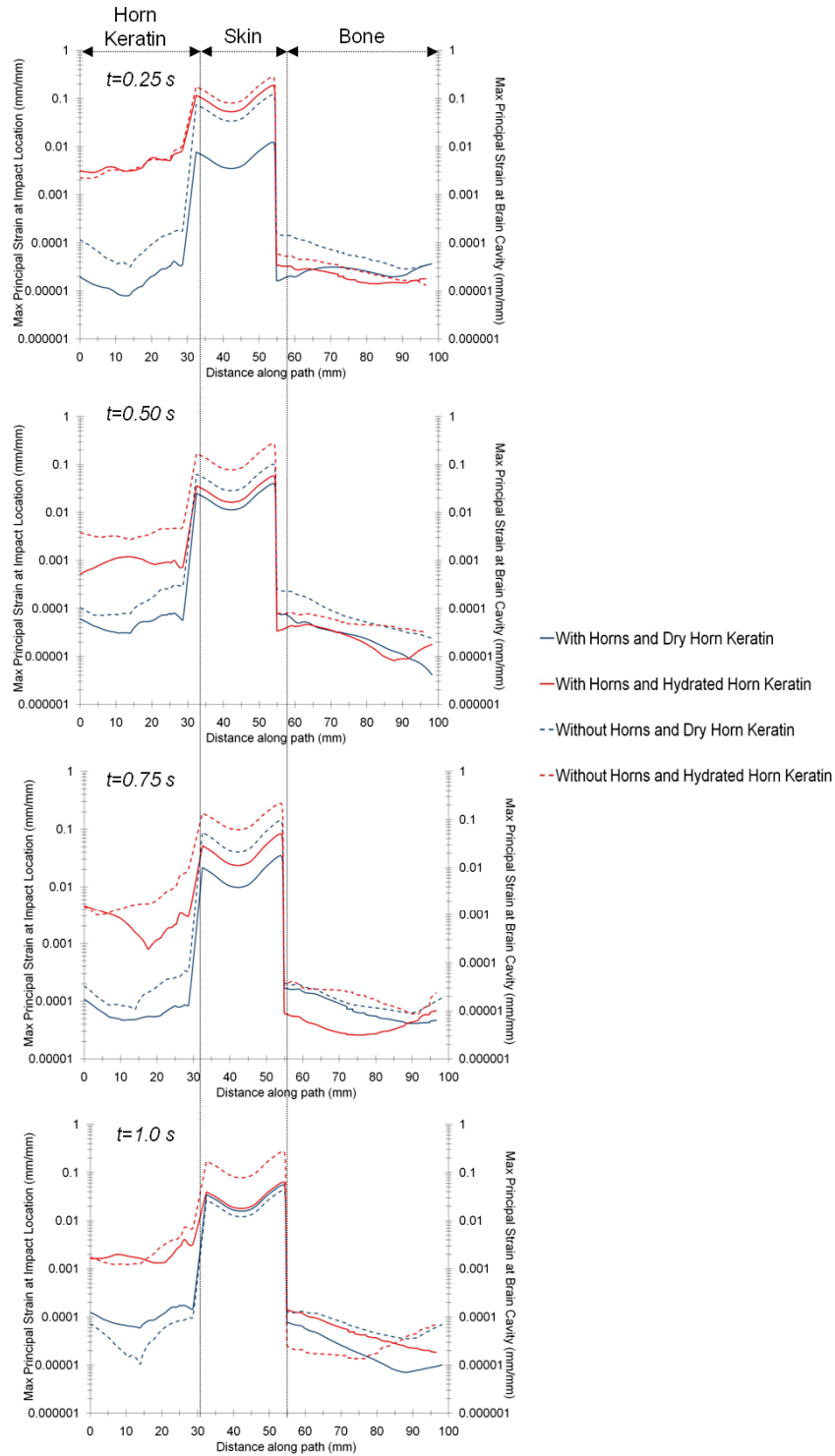
Figure 4.8   Plots of maximum principal strain along the path originating at the point
of impact on the left horn (x=0 mm) and terminating at the brain cavity
(x=100 mm) at times t=0.25 s, t=0.5 s, t=0.75s, and t=1.0 s.

Discussion

When considering the von Mises stresses, which reflect the distortional or shearing within the material, Figure 4.6 indicates that one limiting response was the case where full length horns with hydrated keratin and another limiting response was the model where the horn was cut-off and dry keratin properties were used. Figure 4.6 reveals that the largest von Mises stress (σ_m = 2.6 MPa) was experienced at the brain cavity at t=0.75 s for the FEM without horns and with dry keratin; alternatively, for the mesh with horns and moistened keratin σ_m = 0.5 MPa, a 5× reduction. The results clearly show that both the wet keratin and the geometry of the horn reduce the stresses received by the brain. Not only to the brain, Figure 4.6 also reveals that the meshes without horns and the meshes with dry keratin also transferred the highest stresses to the bone throughout the entire simulation time.

Another important point revealed by Figure 4.6 is the stresses increase much more as time proceeds forward when the shock wave was in the keratin and the skin for the meshes that did not have the full horns. This indicates that the initial shock and the shock wave reflections from the free surfaces help focus the stresses to intensify them within the keratin and the skin. For the meshes with full horns, the initial shock waves from the applied pressure-time history would be the same as for the meshes without the horns.

However, the reflected shock wave interactions were much different. The full horns allowed the shock wave to travel down the full length of the horn and dissipate at the end due to transverse displacements and the introduction of shearing throughout the geometry (cf., Chapter 3). Hence, the reflected shock waves were much lower for the FEM with full horns when compared to the FEM with the horns cut-off. As such, the

71
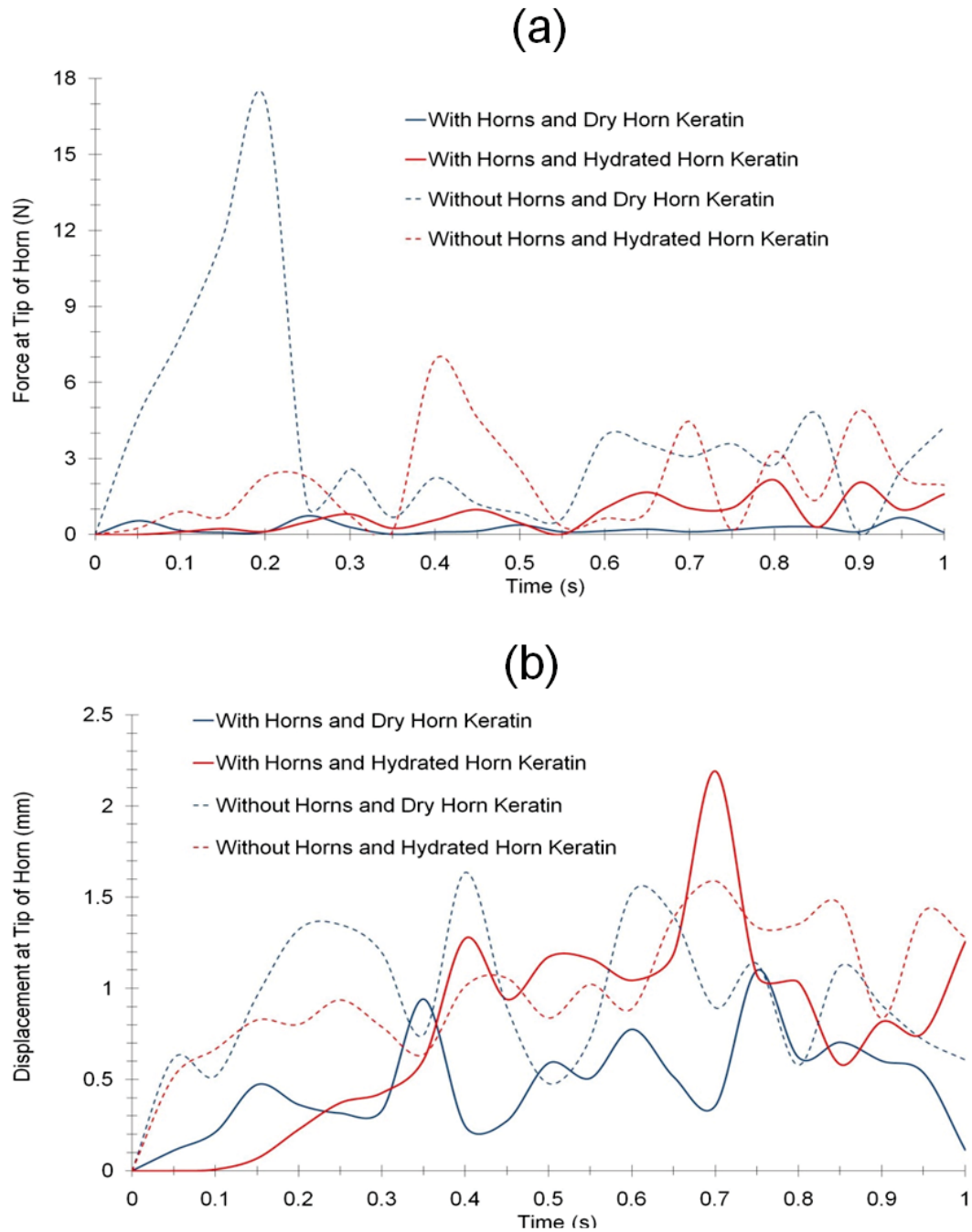
Figure 4.9   (a) Force and (b) displacement history at the tip of horn. For the models with horns attached, force and displacement were measured at 50 nodes laying on the same cross-sectional plane at the tip each horn and then averaged. For the models were the horns were removed, force and displacement measurements were taken at 50 nodes on the cross section where the cut was made (~80mm from the base of the horn) and then averaged.
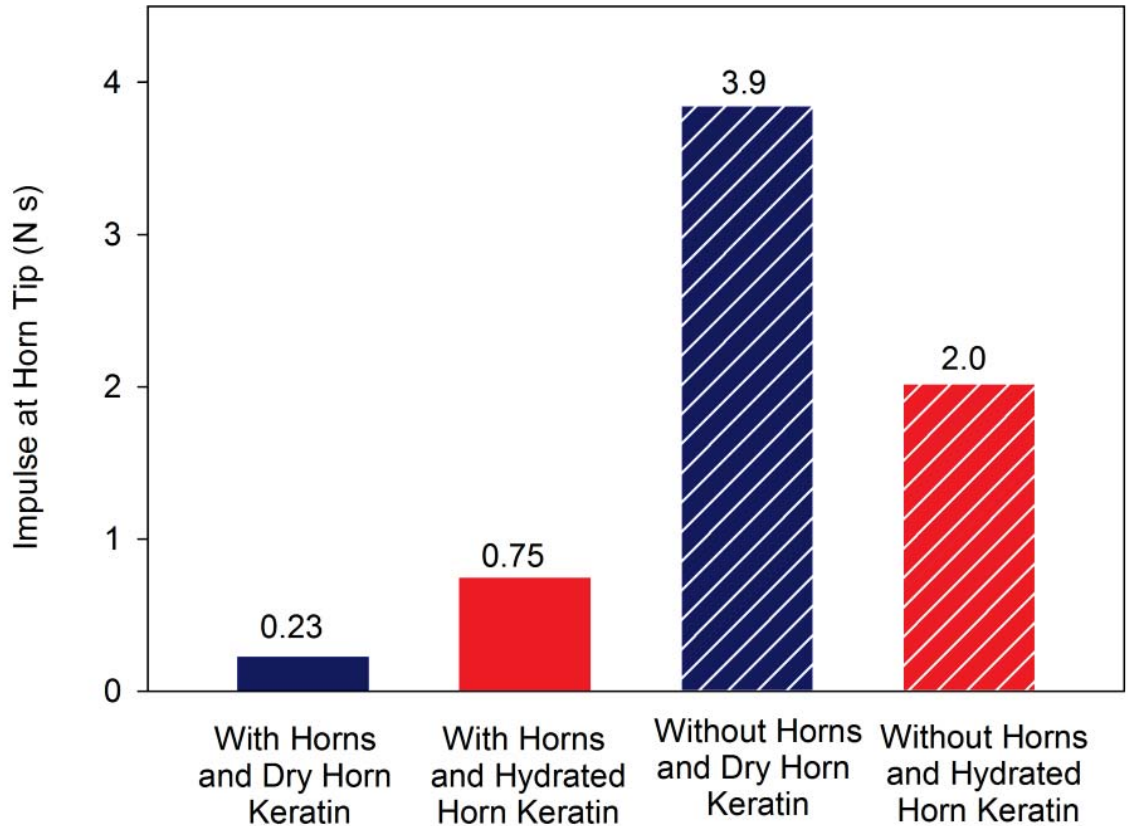
Figure 4.10   Comparison of impulse at the horn tip for horned and dehorned models with dry and hydrated horn keratin. The impulse was taken as the integral of force with respect to time, i.e. the area under the force-time curve.

reflections induced greater von Mises stresses that impacted the "would-be" brain for the simulations that had the horns cut-off, as illustrated in Figure 4.6. Because a complete connectivity was assumed at the skin-bone interface, all of the energy from the shock was essentially transmitted through that boundary. As a result, the stiffer bone did not admit large strains but did admit much greater stresses. Note that the largest von Mises stresses occurred at the bone-skin interface on the bone side due to the skin's compliance and the bone's rigidity.

73
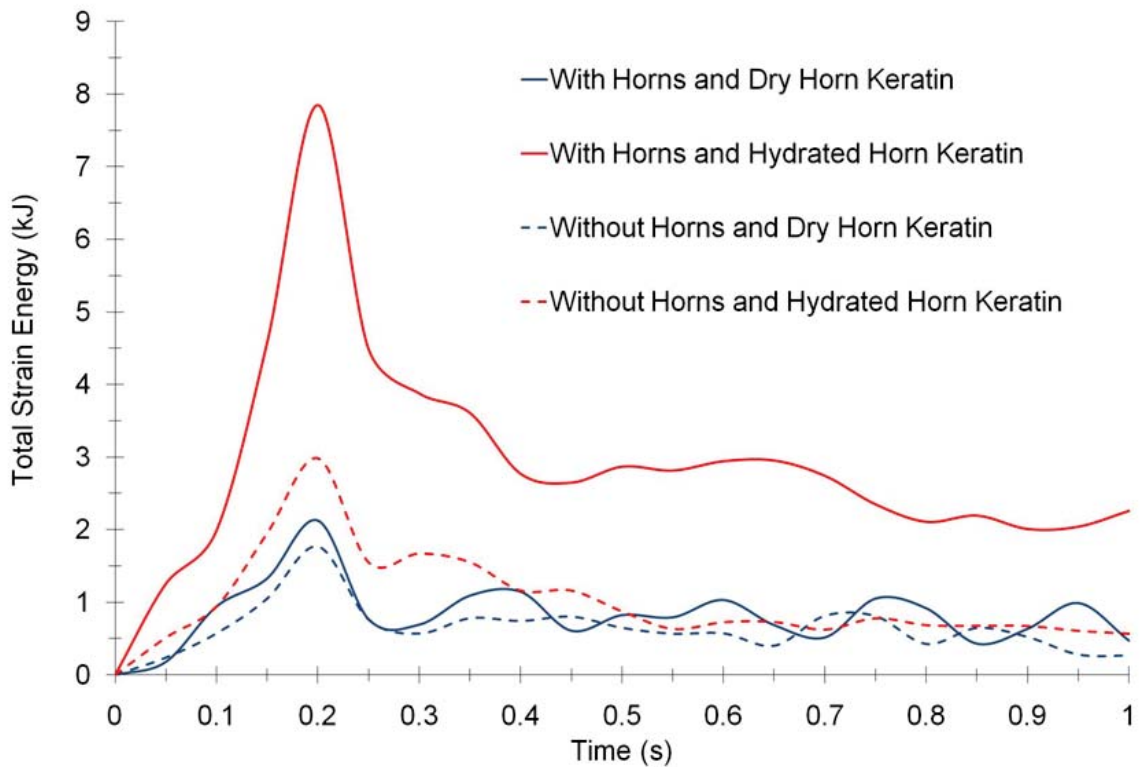
Figure 4.11   Strain energy history plot for models with and without horns using dry and hydrated horn keratin material. Strain energy was calculated by multiplying the total strain energy density of the finite element model by the total volume of the model The volume of the model with and without horns was $3.21 \cdot 10^6$ mm^3 and $1.17 \cdot 10^6$ mm^3 , respectively.

Not only did the simulation with the FEM with full horns and wet keratin give the lowest von Mises stresses, it also allowed the least amount of pressure to reach the cranial cavity. Figure 4.7 shows that almost no pressure was realized by the brain cavity for the full horn morphology when hydrated keratin properties were used, whereas the dehydrated keratin and cut-off horn morphologies admitted higher pressures to the brain cavity, which would be more deleterious to the animal. From Figure 4.7, one can also note that at some time points in the dynamic simulations, tensile stresses were realized in the keratin and bone materials for the dehorned and dry keratin models. A tensile stress-

74

state can be very deleterious to a structure, generally causing mechanical damage and fracture at lower magnitudes in comparison to a compressive stress-state.

In contrast to Figure 4.6 and Figure 4.7, Figure 4.8 reveals the deformation related aspect of energy absorption through each material. The maximum strains were experienced by the skin followed by the keratin followed by the bone as shown in Figure 4.8. This indicates the skin and keratin, which admitted more elastic deformation (and hence strain energy), played an important role in the energy absorption. Also from Figure 4.8, one can see that the hydrated horn keratin admitted much greater strains than the dry horns.

From Figure 4.10, the FEA with the long horn with dry keratin showed ~94% less impulse than the FEA with the cut-off horns. The FEA with horns and hydrated keratin exhibited ~63% less impulse than the same model without horns. This indicates that the horn geometry mitigated the stress wave significantly. It was shown in Chapter 3 that tapering and spiraling geometries introduced lateral displacements and mitigated more impulse than simpler geometries without these features, i.e. tapered, spiraled geometries dissipate more energy.

Figure 4.9 (b) shows the hydrated horn keratin allowed greater displacements at the horn tips over the entire simulation time than did the dry horn keratin. Since all deformation in the models was elastic, the larger displacements in the hydrated horn also indicate that more dissipation occurred in those models. The animations of the simulations also showed the large deflections once the stress wave reached the end of the long horn and the wave did not reflect back to due the dissipation in the deflections.

75

Finally, Figure 4.11 confirms the notion of the full horn providing the greatest energy absorption when compared to the cut-off horn.

The strain energy, shown in Figure 4.11, represents the elastic energy absorbed from the impact load by the entire FEM. Clearly, the model with full horns and hydrated horn keratin was able to provide the largest maximum strain energy (U_{max}=8 kJ). For the model with horns and dry horn keratin, U_{max}=2 kJ. Hence, the hydrated horn keratin effectively increased the strain energy by a factor of four. The dehorned models realized a strain energy, U_{max}=3 kJ when the horn keratin was hydrated, and U_{max}=1.5 kJ when the horn keratin was desiccated. Hence, in the case of the cut-off horns, the hydrated horn keratin allowed twice the amount of energy storage.

Comparing the results from both hydrated simulations shows that the presence of the full length horn provided 5 kJ more maximum strain energy. This effect is much less in the simulations with the dry horn keratin, where only a 0.5 kJ increase in the maximum strain energy was achieved by the presence of the horns. From this we can conclude that the moisture level of the horn keratin is the most influential factor with regard to the strain energy.

Conclusions

The following conclusions can be made regarding this study:

- Three dimensional dynamic, explicit finite element simulations with calibrated constitutive materials to experimental data showed clear parametric trends of the shock mitigation capabilities of a ram striking another ram and quantitative results related to the stresses, pressures, strains, impulses, and energy absorption.

76

- The brain cavity would experience the greatest stresses and pressures from the impact where very short ram's horn was present and the horn was dry. Alternatively, the brain cavity would experience the least amount of stresses and pressures from an impact where a hydrated keratin full ram's horn was present.

- The hydrated keratin ram's horn incurred the greatest displacements at the unconstrained end, incurred the greatest energy dissipation, and admitted the lowest pressures and stresses.

- The skin in between the keratin and bone layers of the horn plays an important role in shock mitigation.

- Hydrated horn keratin is more effective at dissipating an impact induced stress wave than dry horn keratin.

- Long spiral horns that continually reduce in cross-sectional area attenuate the shock such that no reflections back to the skull and brain occur.

CHAPTER V

ENERGY ABSORBENT MATERIALS DESIGN:

LESSONS FROM NATURE

Introduction

While the primary focus of the present work is on the structure-property relations

and energy dissipation mechanisms of ram horns, there are other natural materials that are

just as interesting and deserve attention. This chapter compares the material structures,

mechanical properties, and compressive deformation behavior of ram horn to turtle shell

and armadillo shell, whose function is also to resist penetration and absorb energy.

Interestingly, the turtle shell, armadillo shell, and ram horn are all comprised of

the same structural protein: keratin. Keratin is also found in many other tough materials,

e.g., skin, hair, fur, claws and hooves. Keratin is classified as either α- or β-keratin,

depending on its molecular structure. The protein m6lecules in α-keratin are arranged in a

helic6l 6 tte6n, 6where, 6he 6 rotein 6m6lecules 6n β-keratin are arranged in a sheet-like

pattern (Earland, Blakey and Still 1962). The α form 6f keratin is found in mammals,

while keratin found in birds and reptiles h6s the β arrangement (Fraser et al. 1972).

Turtles are reptiles of the order *Testudines*, most of whose body is shielded by a

special bony or cartilaginous shell developed from their ribs (Alderton 1988).The turtle

shell is usually a fairly firm and rigid structure, although in a few cases, such as the soft-

78

shelled turtles, this covering is softer. Divided into two parts, the turtle shell's upper part is known as the carapace, and the lower part is called the plastron. The turtle's vital organs are well protected by these dorsal and ventral shields and when threatened, the turtle's head, legs, and tail can also be contracted into its portable fortress. The dorsal and ventral shields are strongly connected together for structural support by bony bridges that are located between the front and hind limbs on each side of the body. The strength and rigidity of the turtle shell itself results from an inner bony casing of fused plates, which in turn are covered by a horny shield made of keratin scutes or laminae (Alderton 1988).

Armadillos are small placental mammals of the order *Cingulata*, known for having a leathery armor shell. There are approximately 10 extant genera and around 20 extant species of armadillo, some of which are distinguished by the number of bands on their armor. Nine-banded armadillos (*Dasypus novemcinctus*) are found in South, Central, and North America and have the largest range of any extant species of armadillo. The nine-banded armadillo is only armadillo species found in the United States. Like many other armadillos, the nine-banded armadillo is covered by an outer body armor made up of bony plates covered in a leathery keratinous skin.

Armadillo armor consists of plates of dermal bone covered in relatively small, overlapping epidermal scales. The scales (also called scutes or osteoderms) are composed of bone and are covered by a layer of keratin. Most species of armadillo have rigid shields over the shoulders and hips and several rigid band shields covering their back and flanks. Flexible skin separates each band shield to give the armadillo greater mobility. These osteodermal scales provide a hard but flexible covering and additional

79

bony/keratinous scales partially cover the top of the head, the upper parts of the limbs, and the tail. The underside of the nine-banded armadillo is the only part that lacks armored protection as it is simply covered with soft skin and fur (Dickman 2001). However, when threatened, the banded armadillo rolls up into a ball so that armor covers ever exposed surface. The flexibility of the armadillo is attributed to the loosely connected band shields along its back.

Bighorn sheep (*Ovis canadensis*) horn is designed for excellent stiffness and strength under impact loading, which occurs during sparring between males. Horns are made up of a sheath of keratin and a core of cancellous bone (Packer 1983). The keratin sheath is the outermost horn constituent, and therefore the primary impact load bearing material. Horn keratin is a composite material comprised of tough, crystalline fibers made of α-keratin set in a compliant, amorphous keratin matrix (Fraser et al. 1972, Kitchener 2000, Vincent 1990). The keratin fibers serve to strengthen and stiffen the structure by forming long, hollow, fiber-like tubules. This dispersed tubule microstructure has been observed in other tough biological materials such as hoof, bone, antler, and dentin (McKittrick et al. 2010). In horn, the keratin fibers run parallel to the growth direction and are stacked in a lamellar fashion through the thickness of the horn. Because of the random fiber distribution through the cross section, material behavior in the other two directions (transverse and radial) is nearly identical. Therefore, a horn is a transversely isotropic material, i.e., isotropic in the transverse and radial directions.

McKittrick, et al. (2010) recently reviewed the structure-property relationships in several energy absorbent, mammalian, structural materials, i.e., bones, antlers, teeth, tusks, and hooves, and found that several commonalities permeate through these

80

seemingly very different materials. We extend this study, by investigating the structure-property relationships of a few natural (biological) armor systems, namely turtle shells, armadillo shells, and ram horns. Furthermore, we identify the energy absorbing strategies utilized in these materials and suggest a potential bio-inspired material design based on our findings.

Methodology

The structures and fracture surfaces of turtle shells, armadillo shells, and ram horns were investigated using optical microscopy (OM) and scanning electron microscopy (SEM). Sectioned specimens were cleaned by an ultrasonic cleaner and then cold mounted in epoxy. The mounted specimens were then sputter-coated with gold and examined under a SUPRA-40 field emission gun (FEG)-SEM (CarlZeiss SMT Ltd.).

Compression tests were performed at strain rates of 0.001, 0.01, and 0.1/s. These tests were performed on an Instron 3367 Dual Column Testing System equipped with a 30 kN load cell. The compression specimens were prepared according to ASTM D790. The specific energy absorption during initial deformation was taken as the area under the stress-strain curve up to 0.1 strain, normalized by the density of the material. While, the energy absorbed during collapse was calculated as the area below the curve, normalized by the porosity of the material, bounded from 0.1 to 0.4 strain. The porosity of each material was found by analyzing cross-sectional images using the Image-Analyzer software package developed by the Center for Advanced Vehicular Systems (CAVS) at Mississippi State University.

81

Results and Discussion

Structural Characterization

The multiscale hierarchy and structure of the armadillo shell, turtle shell, and ram horn are shown in Figures 5.1-5.3. An overarching design similarity is the presence of a hierarchy of multiple distinct reinforcing layers, allowing for outstanding energy absorption and unique deformation mechanisms. There are only two basic fiber forming polymers in nature, polypeptides (proteins) and polysaccharides (celluloses), yet nature has overcome this limit in material variation through multi-scale structural (hierarchical) organization. The hierarchical structures present in biological materials have the advantage of providing multiple, redundant loading paths. The mechanical properties of biomaterials are modulated, tailored, and optimized by controlled interactions between the hierarchies.

Microstructural observations on the nine-banded armadillo shell revealed a multiphase composite material that is arranged in a hierarchical fashion. The multiscale hierarchical structure of the nine-banded armadillo shell is depicted in Figure 5.1. The nine-banded armadillo is covered by an outer body armor made up of plates called scutes covered in a leathery keratinous skin. These osteodermal scales provide a hard but flexible covering. The osteoderms are typically hexagonal or pentagonal in the forward and rear shells and are rectangular with alternating triangular pattern in the band shell. The armor plate is divided into three parts, each covering a specific part of the body: a shield on the shoulder region (forward shell), a pelvic shield (rear shell), and the characteristic bands between the forward and rear shells.

82
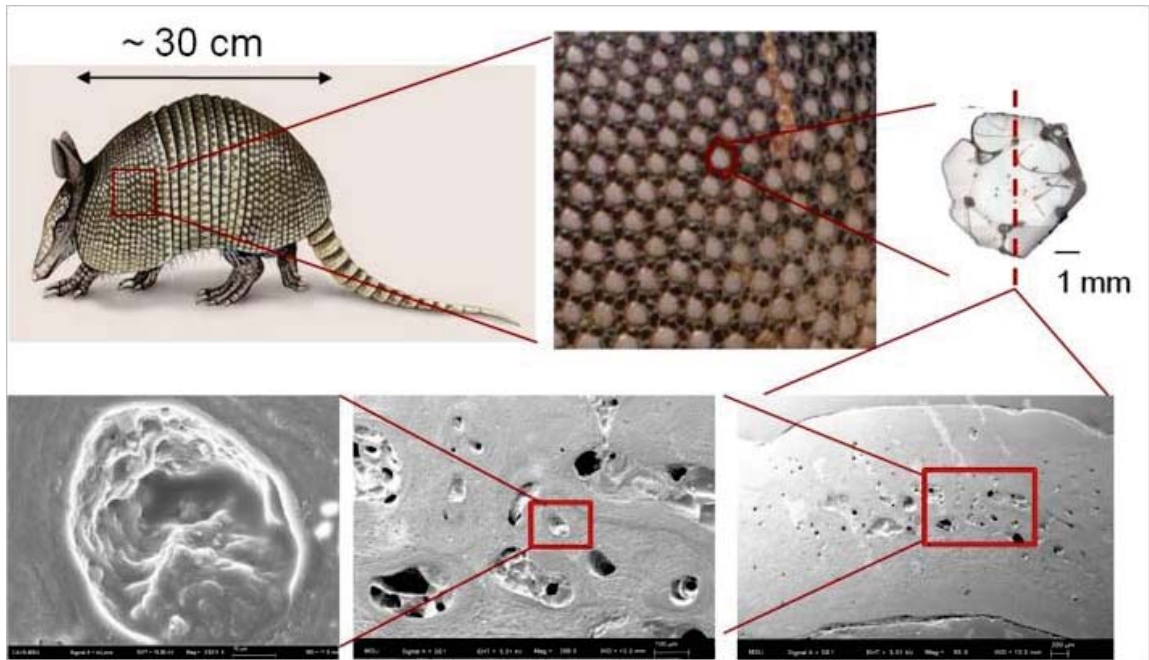
Figure 5.1   Multiscale hierarchy and structure of the armadillo shell. The armadillo shell comprises thousands of bony scutes covered by a keratinous skin. The scutes resemble a functionally graded material (FGM) having a relatively dense exterior and a porous core (adapted from Rhee, Horstemeyer and Ramsay (2011)).

In the band shell region, each band is overlapped and separated by a thin epidermal layer, which imparts mobility to the banded armadillo. A forward shell of the nine-banded armadillo is made up of a sandwich composite structure of functionally graded material (FGM) having relatively denser exterior layers and an interior foam-like layer. The exterior layer showed a much denser and smooth surface structure than the interior layer at 65   magnification, whereas the interior layer comprised a closed-cell structure with some fibrous structure inside the network. These features are very similar to those found in the turtle shell carapace reported by Rhee et al. (2009). Exterior layers observed from the top and bottom surfaces showed almost fully dense surface structure at the same level of magnification. However, some pores were observed in the SEM

83

micrographs since these specimens were mechanically polished. Image analysis revealed the internal porosity for armadillo shell to be approximately 2%.

The dermal shell of the nine-banded armadillo is comprised of a sandwich composite structure similar to a FGM. The exterior layer is denser than the foam-like bony network interior. The band shell revealed a more complicated structure and adjacent bands in the band shell region are partially overlapped and connected with each other to provide flexibility in addition to protection. This is very different when compared to turtle shells which have a harder, stronger joint but less ductile joint than the armadillo shell.

Structural observations on the turtle shell revealed a multiphase composite material that is also arranged as a multiscale hierarchy. The multiscale hierarchical structure of the turtle shell carapace is depicted in Figure 5.2. Similar to the armadillo shell, the turtle shell comprises a series of connected individual plates covered with a layer of keratinized scutes. The scutes are made of β-keratin, which comprises the scales of many other reptiles as well (Fraser and Parry 1996). These scutes overlap the seams between the shell bones and serve to reinforce the overall protection to the shell. The carapace is made of a sandwich composite structure, having relatively denser exterior layers and an interior fibrous foam-like layer. SEM micrographs clearly revealed such fibrous structure inside of the cell. In addition, the results of image analysis revealed the average porosity level of the turtle shell to be approximately 65%.
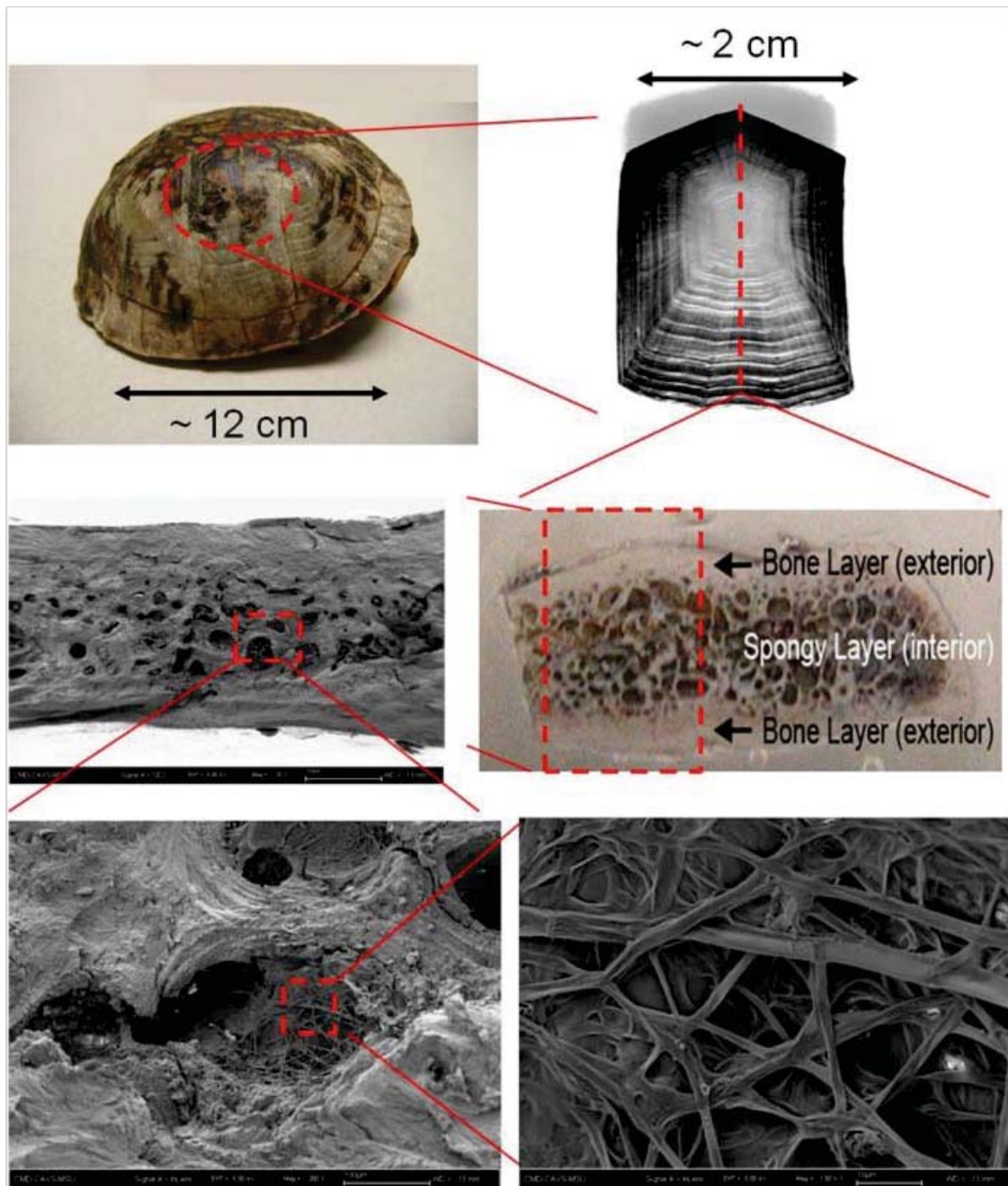
Figure 5.2   Multiscale hierarchy and structure of the turtle shell carapace. Similar to the armadillo shell, the turtle shell comprises a series of connected individual plates covered with a layer of keratinized scutes. The carapace is made of a sandwich composite structure, having relatively denser exterior layers and an interior fibrous foam-like layer (adapted from Rhee et al. (2009)).

Similar to turtle and armadillo shell, ram horn is a hierarchical material with the outermost layer being the tough keratin protein. The multiscale hierarchical structure of the ram horn is shown in Figure 5.3. Horn comprises a keratin sheath, surrounding a core of cancellous bone. At the molecular level, horn keratin consists of helical, α-keratin protofibrils. These protofibrils assemble into rope-like structures called intermediate filaments (Feughelman 1997). The crystalline intermediate filaments are oriented along the growth direction and coil up into hollow, elliptically shaped tubules. These tubules, which resemble hollow reinforcing fibers, are embedded in an amorphous keratin matrix. The matrix is akin to a randomly oriented, chopped fiber composite.

The average porosity of horn keratin, determined using image analysis, was found to be approximately 6%. However, there is a porosity gradient through the thickness of the horn keratin, with the highest porosity being at the outer surface. This is in contrast to the turtle and armadillo shells, which are very dense at the outer surface. The surface porosity directly correlates with the permeability of keratin to water. The mechanical properties of keratin are highly sensitive to moisture content (Feughelman 1997, Bertram and Gosline 1987, Fraser et al. 1972, Kitchener and Vincent 1987). In fact, moisture content was shown to be the most influential parameter in regards to the mechanical behavior of horn keratin in Chapter 2. The high surface porosity of horn keratin allows moisture to enter the keratin material. Hydrated keratin has a higher toughness, capable of absorbing more energy, but hydrated horn also allows greater deformation. Rams display an interesting behavior known as horning, where they frequently rub their horns in mud and against wet vegetation prior to fighting to take advantage of this effect (Kitchener 1987b).

86
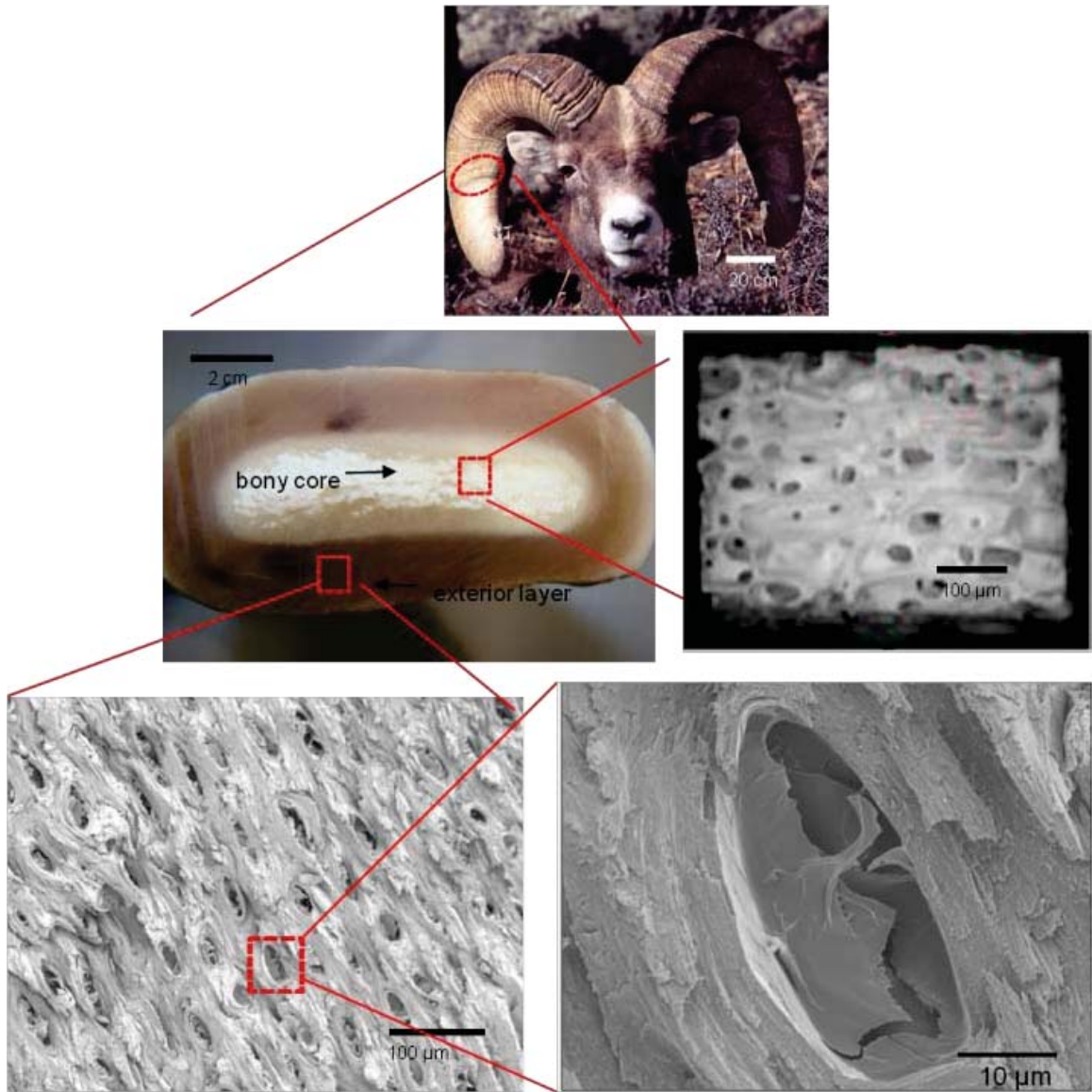
Figure 5.3   Multiscale hierarchy and structure of the ram horn. Horn comprises a keratin sheath, surrounding a core of cancellous bone. The crystalline keratin fibers are oriented along the growth direction and coil up into hollow, elliptically shaped tubules. These tubules, which resemble hollow reinforcing fibers, are embedded in an amorphous keratin matrix.

In contrast, turtles and armadillos rely on the rigidity of their keratin shell for protection. The surface porosity of their keratin shell is extremely low, which prevents water from being absorbed by the material and becoming significantly more pliant. If the

87

stiffness of the turtle and armadillo shell were to decrease substantially, as would be the case if moisture entered the keratin, the animals would be much more venerable to injury.

A striking similarity among the structures of the turtle shell, armadillo shell, and ram horn is that each material has an outermost layer of keratin, surrounding a closed-cell, foam-like core. The porous cores function to absorb large amounts of energy during collapse at a low cost in weight and also provide toughening mechanisms such as crack deflection and crack arrest.

Mechanical Characterization

The compressive stress-strain responses for armadillo shell, turtle shell and ram horn at strain rates of 0.001, 0.01, and 0.1/s are shown in Figure 5.4. Compression test results revealed a typical deformation behavior of cellular solids showing three distinctive regions: an initial linear elastic deformation, a plateau of deformation, and another period of near linear deformation with a fairly high modulus. The favorable deformation mechanisms of these materials in compressive conditions can be explained by those of synthetic foams found elsewhere (Gibson and Ashby 1999, Rhee et al. 2009).

The three materials showed varying levels of strain rate dependence. The ram horn had the highest strain rate sensitivity, while the armadillo and turtle shell showed considerably strain rate dependence in the range that was tested. The Young's modulus for each material increased with increasing strain rate, which is a typical phenomenon among polymeric materials. When loaded at a low strain rate, the molecular chains have sufficient time to adjust to the imposed stress and the modulus value is lower than for the

88
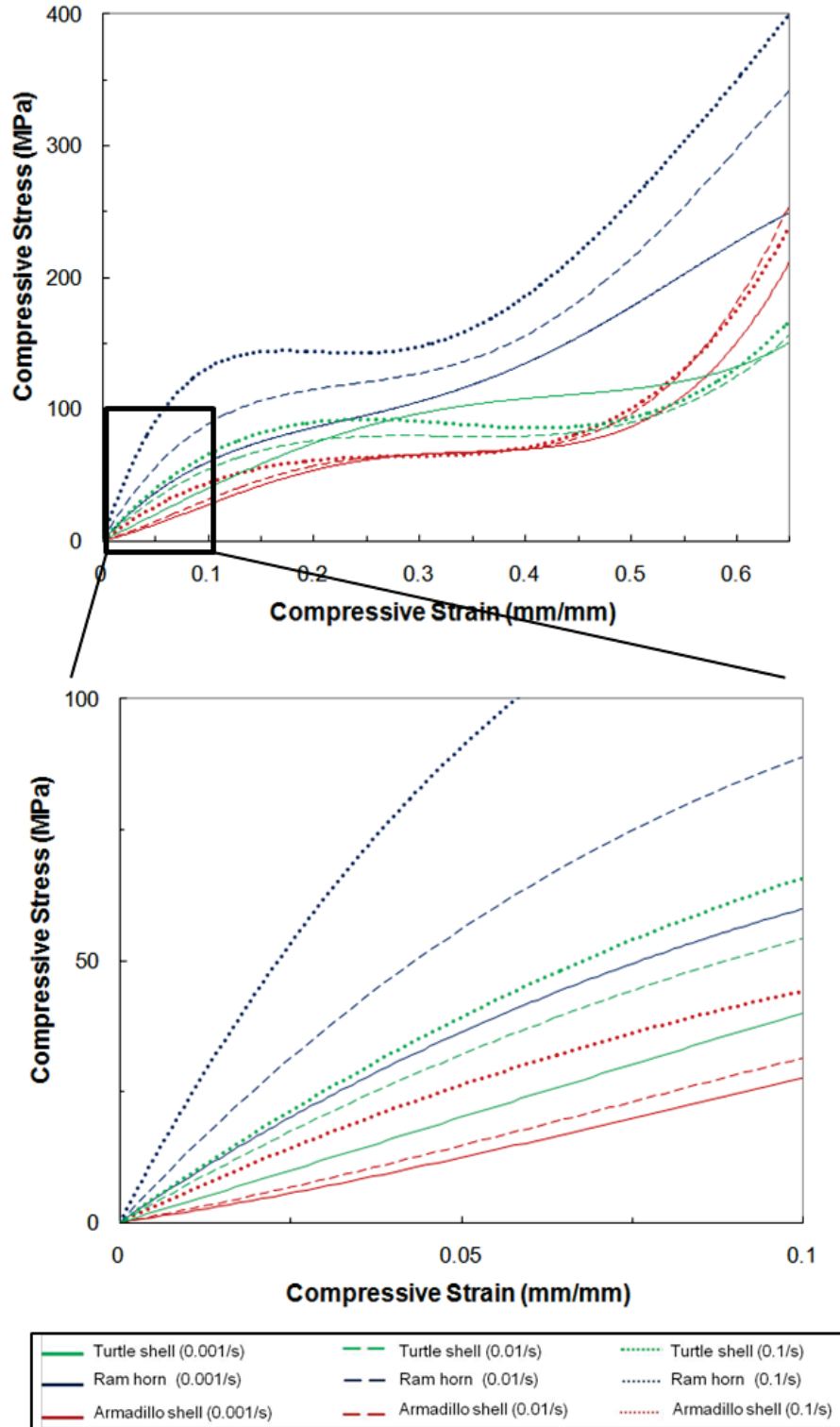
Figure 5.4   Compressive stress-strain response for turtle shell, armadillo shell, and ram horn for strain rates of 0.001, 0.01, and 0.1/s.

89

case where the same material is loaded at a higher strain rate and the molecular chains do not have enough time to untangle (Goble and Wolff 1993).

Figure 5.5 provides a comparison of specific energy absorption obtained from the compression test results. Density and porosity levels of the test specimens are factored into this normalized data. The specific, elastic energy absorption (strain energy) of each material increased with increasing strain rate because the modulus increased with strain rate. This yielded more area under the stress-strain curve in the initial elastic regime, which is considered here to be from 0 to 0.1 strain.

However, the majority of the energy is absorbed in the deformation plateau (between 0.1 and 0.4 strain). In this regime of the stress-strain curve, the foam-like cores collapse by micro-buckling, yielding or crushing; this allows strain to continually increase with little or no increase in stress.

The total specific energy absorption for the turtle shell, ram horn, and armadillo shell increased with increasing strain rate. This effect has been observed in polymeric, metallic, and biomaterial foams (Chakravarty 2010, Yi et al. 2001). The porosity contributes significantly to specific energy absorption. This is evidenced by the fact that the turtle shell, with 65% porosity, gives the largest amount of energy absorption, while the armadillo shell, with only 2% porosity, shows the least amount of energy absorption.

Each material yielded a considerable plateau of deformation, which is a model index of good energy absorbing materials. The combining information of these two plots in Figures 5.4 and 5.5 is very important to design the optimum energy absorbing composite material. For example, composite foam materials can be tailored to give the

90

best combination of properties for a given package by choosing the right combination of the cell wall materials, relative density, reinforcement phases, and so on.
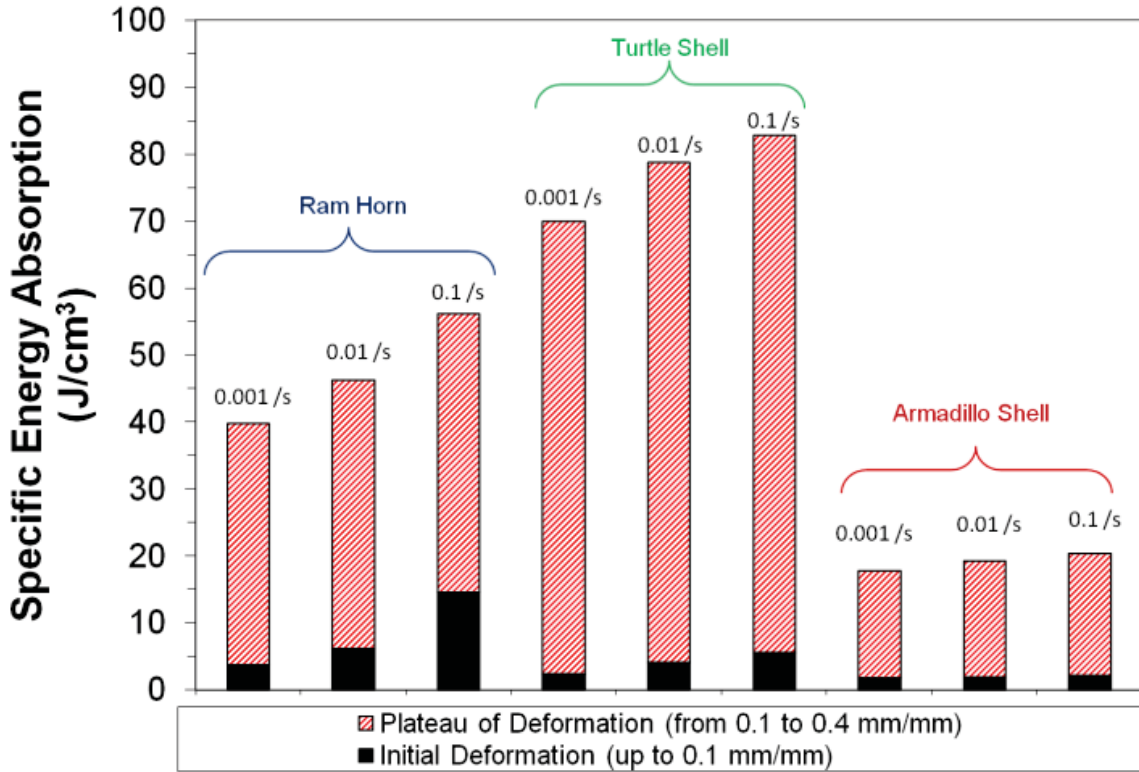
Figure 5.5   Specific energy absorption for ram horn, turtle shell, and armadillo shell at strain rates of 0.001, 0.01, and 0.1/s.

Conclusions

Several conclusions can be garnered from this study of the structure-property relations of the energy absorbent, keratinous turtle shell, armadillo shell, and ram horn materials.

- The materials each have a multiscale, hierarchical material structure. Each material also has a sandwich composite structure, with a high porosity, foam-like interior core.

91

- Ram horns have a high surface porosity, which allows water to penetrate into the horn, increasing its toughness. Turtle and armadillo shells have little or no surface porosity, making them impermeable to water and thereby not compromising the shells' rigidity.

- Compression test results for the turtle shell, ram horn and armadillo shell showed a typical nonlinear deformation behavior recognizant of synthetic foams.

- The compressive response of each material had an initial nearly linear, elastic regime, followed by a plateau of deformation, which preceded the eventual material densification.

- There is a high degree of interaction and synergism between the protein skin and the foam-like core that strongly enhances the mechanical properties. In fact, the structures are so well organized that biological composites can achieve properties greater than their constituent materials and thus overcome the mixtures law.

We can use these lessons from nature as inspiration for development of lightweight, armor systems for soldiers and armored vehicles. A possible bio-inspired design strategy entails encasing a metallic foam core with a fiber-polymer composite laminate. This sandwich structure mimics the structure found in turtle and armadillo shells, and ram horns. The skin of this design serves to resist penetration whilst the central core functions to absorb large amounts of energy at a low cost in weight. Good adhesion between skin and the metallic core is crucial for the design to succeed and is an excellent opportunity for future research.

92

CHAPTER VI

SUMMARY AND FUTURE WORK

Summary

A recently emerging engineering design approach entails studying the brilliant design solutions found in nature with an aim to develop design strategies that mimic the remarkable efficiency found in biological systems. This novel engineering approach is referred to as bio-inspired design. In this context, The present study quantified the structure-property relations in bighorn sheep (*Ovis canadensis*) horn keratin, qualitatively characterized the effects of a tapered spiral geometry (the same form as in a ram's horn) on pressure wave and impulse mitigation, described the stress attenuation capabilities and features of a ram's head, and compared the structures and mechanical properties of some energy absorbent natural materials. The results and ideas that were presented can be used in the development of lightweight, energy absorbent, bio-inspired material designs.

Among the most notable conclusions garnered from this research include:

- Horn keratin behaves in an anisotropic manner similar to a long fiber composite.

- Moisture content dominates the material behavior of horn keratin more than anisotropy, age, and stress-state. This makes moisture content the most influential parameter on the mechanical behavior of horn keratin.

93

- Tapered geometries mitigate the impulse generated by a stress wave due to the convergent boundary and a continually decreasing cross sectional area such that greater uniaxial stresses and subsequent axial deformation arises. Furthermore, the tapered geometry introduces small shear stresses that further decrease the impulse.

- Spiral geometries attenuate the impulse generated by a stress wave by the introduction of shear stresses along the length of the spiral. These shear stresses introduce transverse displacements that function to lessen the impulse.

- When both a taper and spiral geometry are used in a design, their synergistic effects multiplicatively reduce the impulse

- Tough natural materials have a high porosity, which makes them light-weight, while increasing their compressive energy absorption ability.

- Biomaterials whose functions include protection and energy absorption feature a multiscale, hierarchical, composite structure. The constituent materials are arranged in such ways to achieve a synergistic effect, where the properties of the composite exceed the properties of its constituents. Biological materials are therefore not confined to the law of mixtures.

Future Work

The following subsections describe topics related to those in the present work worthy of further research.

94

Determination of High Rate Tensile Response of Horn Keratin

In the mechanical property evaluation of horn keratin described in Chapter 2, the quasi-static tensile and compressive response of horn keratin was determined. The high rate compressive response was also determined, and was published in a separate work (McKittrick et al. 2010). The effects of strain rate on the radial and longitudinal compressive response of bighorn sheep horn keratin are shown in Figure 6.1.

However, the inability to manufacture Hopkinson bar tension specimens prevented determining the high rate tensile response of horn keratin. In addition to the data in Chapter 2, the high rate longitudinal and transverse tensile response of both wet and dry horn keratin would completely characterize the anisotropy, stress-state, moisture, and strain-rate dependence of horn keratin. These data would be sufficient to development of a constitutive model that could accurately capture the response of horn keratin for various stress-states, strain-rates, moisture levels. A precision water-jet cutting machine would be the ideal method of preparing the small dog bone specimens for the Hopkinson tension bar.

Investigation of Material Dependence on Stress Wave Mitigation

In Chapter 3, FEA was used to show the show the geometrical effects on pressure and impulse are mitigation within a solid. Linear elastic material properties typical of steel were used in the study. Time constraints prevented determining if the solutions were material dependent. While it is probable that the trends will be the same, it is likely that a non-linear, viscoelastic material will give a different response than the linear elastic

95
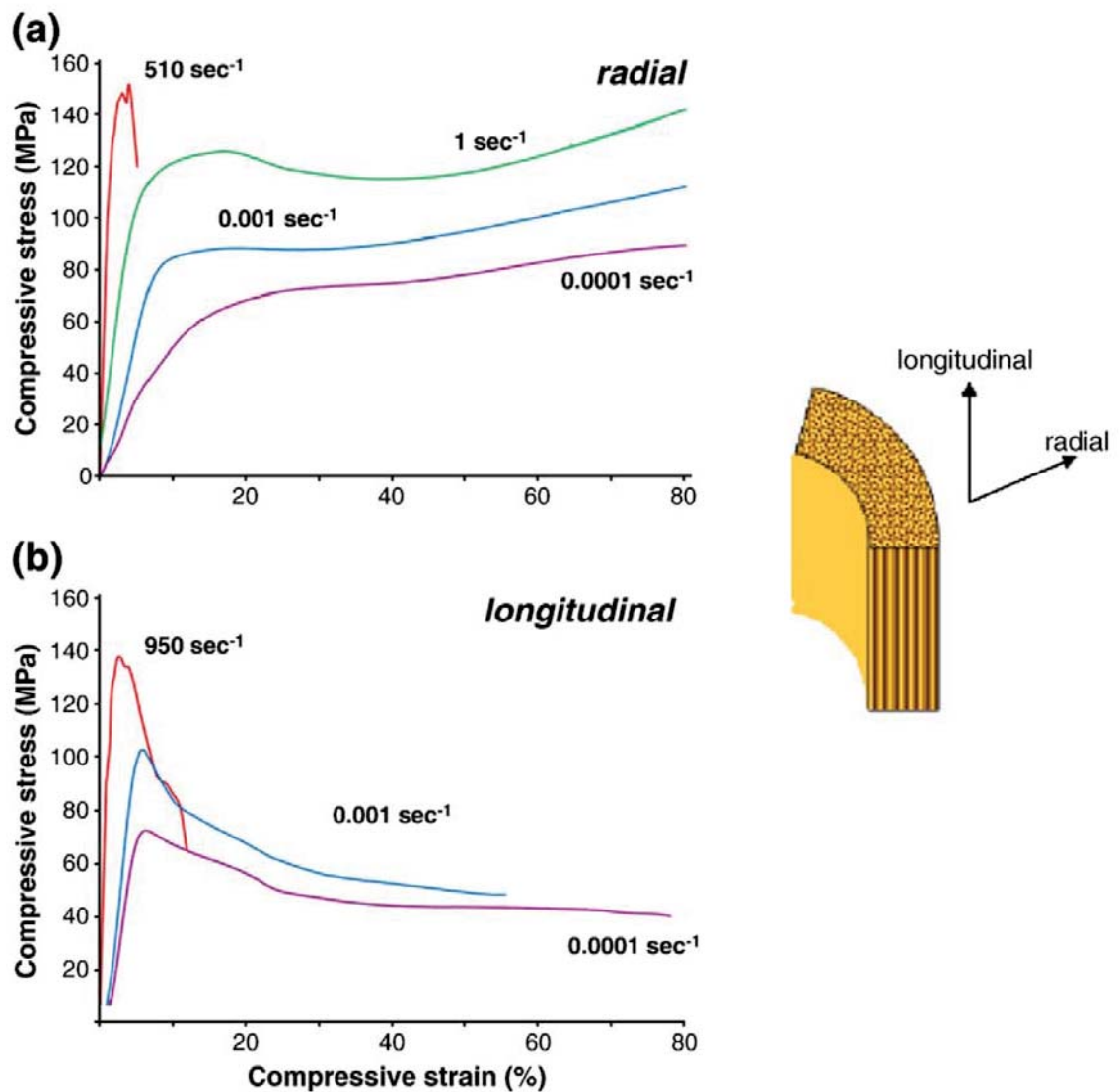
Figure 6.1   Strain rate effects on the compressive stress–strain response for bighorn sheep horn keratin in the (a) radial and (b) longitudinal directions (taken from McKittrick et al. (2010).

material that was used. Also, in consideration of the fact that we are attempting to simulate natural materials and structures, a supplemental study to the one presented in Chapter 3 is merited. The supplemental study should employ material parameters similar to those found in nature, which generally give a non-linear, viscoelastic stress-strain response. The ABAQUS input decks used in this study are provided in Appendix A.

96

Modifying the original input decks should make material substitution a relatively straight forward process.

Validation of Ram Impact Simulations

Chapter 4 presented a FEA of a ram impact. As is the case with most all FEA modeling, several assumptions and simplifications had to be made. The validity of these assumptions and the accuracy of the results should be verified experimentally. An ideal validation would require measurement of stresses and strains during an actual ram fight. Gathering this data may prove unfeasible. An alternative method would include impact tests similar to those done by Jaslow and Biewener (1995). However, one must keep in mind that the FEA results showed that the thick layer of skin between the horn keratin and bone was an important contributor to the energy absorption ability of the ram skull. Therefore, the tests would require fresh specimens with this skin still intact.

Mesh Convergence Study and Remeshing of Ram Head Model

The specimens used to construct the FEA meshes for the ram impact simulations presented in Chapter 4 had inherent flaws. These flaws required tedious manipulation of the models. It was not possible to fully remove every flaw in the models due to the complex geometry. A scan of a high quality ram head specimen would produce a significantly better mesh. High quality specimens can be obtained from Skulls Unlimited, Inc.

Also, new software, i.e. Simpleware (Simpleware, Ltd.), has recently become available and is superior to the MIMICS (Materialise, Inc.) software that was used to

97

generate the FEA mesh used in this study. One advantage of Simpleware is that it is not limited to brick elements. Using tetrahedral elements on the surfaces would produce more accurate topologies and prevent the voxelated effect inherent to brick elements, which produce artificial stress concentrations on the surfaces. To reduce computational expense, half symmetry could be used on the new ram head model. This would also make a mesh convergence study feasible since the size of the model will be significantly reduced.

Development of a Constitutive Model for Biomaterials

Currently, a constitutive model capable of capturing the response of biomaterials for various strain rates, moisture levels, stress-states, loading direction, age, and temperature does not exist. The material modeling, as described in Chapter 4, required making several simplifying assumptions to make use of the models available. Ideally, a physics based constitutive model for biomaterials would be able to capture the effects of the aforementioned factors. The development of such a model is by far the most daunting of all the tasks suggested in this section.

REFERENCES

Achenbach, J. D. 1993. *Wave propagation in elastic solids*. North-Holland.

Alderton, D. 1988. *Turtles & Tortoises of the World*. New York: Facts on File.

Arciszewski, T. & C. J. 2006. Bio-inspiration: Learning creative design principia. In *Intelligent computing in engineering and architecture*, 32-53. Ascona, Switzerland.

Arruda, E. M. & M. C. Boyce (1993) A three-dimensional constitutive model for the large stretch behavior of rubber elastic materials. *Journal of the mechanics and physics of solids,* 41**,** 389-412.

Ball, P. (2001) Life's lessons in design. *Nature,* 409**,** 413-416.

Bertram, J. E. A. & J. M. Gosline (1987) Functional design of horse hoof keratin: The modulation of mechancial properties through hydration effects. *Journal of Experimental Biology,* 130**,** 121-136.

Bond, C., D. J. Hill, D. I. Meiron & P. E. Dimotakis (2009) Shock focusing in a planar convergent geometry: Experiment and simulation. *Journal of Fluid Mechanics,* 641**,** 297-333.

Callister, W. D. 2007. *Materials Science and Engineering: An Introduction*. New York, NY: John Wiley & Sons.

Chafi, M., G. Karami & M. Ziejewski (2010) Biomechanical Assessment of Brain Dynamic Responses Due to Blast Pressure Waves. *Annals of Biomedical Engineering,* 38**,** 490-504.

Chen, L., R. Ballarini, H. Kahn & A. H. Heuer (2007) Bioinspired micro-composite structure. *Journal of Materials Research,* 22**,** 124-131.

Currey, J. D. (1988) Strain rate and mineral content in fracture models of bone. *Journal of orthopedic research,* 6**,** 32-38.

---. 2002. *Bones: Structure and Mechanics*. Princeton: Princeton University Press.

--- (2005) Hierarchies in Biomineral Structures. *Science,* 309**,** 253-254.

Davis, J. L. 1988. *Wave Popagation in Solids and Fluids*. New York, NY: Spring-Verlag Inc.

Demma, A., P. Cawley, M. Lowe & B. Pavlakovic (2005) The effect of bends on the propagation of guided waves in pipes. *Journal of Pressure Vessel Technology, Transactions of the ASME,* 127**,** 328-335.

Dickman, C. R. 2001. In *The New Encyclopedia of Mammals,* ed. D. W. Macdonald. Oxford: Oxford University Press.

Dighe, M. D., A. M. Gokhale & M. F. Horstemeyer (2002) Effect of loading condition and stress state on damage evolution of silicon particles in an Al-Si-Mg-Base cast alloy. *Metallurgical and Materials Transactions A,* 33**,** 555-565.

Druhala, M. & M. Feughelman (1974) Dynamic mechanical loss in keratin at low temperatures. *Colloid and Polymer Science,* 252**,** 381-391.

Earland, C., P. R. Blakey & J. P. Still (1962) Molecular orientation of some keratins. *Nature,* 196**,** 1287-1291.

Elices, M. 2000. Structural Biological Materials: Design and Structure-Property Relationships. In *Pergamon Materials Series,* ed. R. W. Cahn. Kidlington: Elsevier Science.

Farke, A. A. (2008) Frontal sinuses and head-butting in goats: a finite element analysis. *J Exp Biol,* 211**,** 3085-3094.

Feughelman, M. 1997. *Mechanical Properties and Structure of Alpha-Keratin Fibres*. Sydney: University of New South Wales Press.

Fleck, N. A. & B. Budiansky. 1991. Compressive failure of fibre composites due to microbuckling. In *Inelastic deformation of composite materials*, 235-273. Troy, NY, USA: Springer-Verlag New York Inc,.

Fleck, N. A. & I. Sridhar (2002) End compression of sandwich columns. *Composites Part A: Applied Science and Manufacturing,* 33**,** 353-359.

Fraser, R. D., T. P. MacRae, D. A. Parry & E. Suzuki (1986) Intermediate filaments in alpha-keratins. *Proceedings of the National Academy of Sciences,* 83**,** 1179.

Fraser, R. D. B. & T. P. MacRae. 1980. Molecular structure and mechanical properties of keratins. In *The Mechanical Properties of Biological Materials,* eds. J. Vincent & J. Currey, 211-246. Cambridge: Cambridge University Press.

Fraser, R. D. B., T. P. MacRae & G. E. Rogers. 1972. *Keratins*. Springfield, IL: Bannerstone House.

Fraser, R. D. B. & D. A. D. Parry (1996) The molecular structure of reptilian keratin. *International Journal of Biological Macromolecules,* 19**,** 207-211.

Frasier, R. D. B. & T. P. MacRae. 1980. Molecular structure and mechanical properties of keratins. In *The Mechanical Properties of Biological Materials,* ed. J. V. a. J. Currey, 211-246. Cambridge: Cambridge University Press.

Fratzl, P. & R. Weinkamer (2007) Nature's hierarchical materials. *Progress in Materials Science,* 52**,** 1263–1334.

Gavric, L. (1995) Computation of propagative waves in free rail using a finite element technique. *Journal of Sound and Vibration,* 185**,** 531-543.

Geist, V. 1971. *Mountain sheep: A study in behavior and evolution*. Chicago: Chicago University Press.

Gibson, L. J. & M. F. Ashby. 1999. *Cellular solids: structure and properties*. Cambridge Univ Pr.

Goss, R. J. 1983. *Deer antlers - regeneration, function and evolution*. New York: Academic Press.

Gurdijian, E. S., J. E. Webster & R. H. Lissner (1949) Studies on skull fracture with particular reference to engineering factors. *Am J Surg.,* 78**,** 736-742.

Hayashi, T., W. J. Song & J. L. Rose (2003) Guided wave dispersion curves for a bar with an arbitrary cross-section, a rod and rail example. *Ultrasonics,* 41**,** 175-183.

Inoue, O., N. Takahashi & K. Takayama (1993) Shock wave focusing in a log-spiral duct. *AIAA journal,* 31**,** 1150-1152.

Jaslow, C. R. & A. A. Biewener (1995) Strain patterns in the horncores, cranial bones and sutures of goats (*Capra hircus*) during impact loading. *J. Zool.,* 235**,** 193-210.

Ji, B. & H. Gao (2004) Mechanical properties of nanostructure of biological materials. *Journal of the mechanics and physics of solids,* 53**,** 1963-1990.

Johnston, N. J. 1987. *Toughened Composites*. Houston, TX: ASTM STP 937.

Kaku, M. 2004. *Einstein's Cosmos: How Albert Einstein's Vision Transformed the Understanding of Space and Time*. New York, NY: W.W. Nortons & Co., Inc.

101

Kasapi, M. A. & J. M. Gosline (1999) Micromechanics of the equine hoof wall: Optimizing crack control and material stiffness through modulation of the properties of keratin. *Journal of Experimental Biology,* 202**,** 377-391.

Kitchener, A. (1987a) Effect of water on the linear viscoelasticity of horn sheath keratin. *Journal of Materials Science Letters,* 6**,** 321-322.

--- (1987b) Fracture toughness of horns and a reinterpretation of the horning behaivor of bovids. *Journal of Zoology London,* 213**,** 621-639.

--- (1988) An analysis of the forces of fighting of the blackbuck (Antilope cervicapra) and the bighorn sheep (Ovis canadensis) and the mechanical design of the horns of bovids. *Journal of Zoology London,* 214**,** 1-20.

---. 1991. The evolution and mechanical design of horns and antlers. In *Biomechanics in evolution,* eds. J. M. V. Rayner & R. J. Wootton, 229 - 253. Cambridge University Press.

---. 2000. Fighting and the mechanical design of horns and antlers. In *Biomechanics in animal behaviour,* eds. P. Domenici & R. W. Blake. Oxford: BIOS Scientific Publishers.

Kitchener, A. & J. F. V. Vincent (1987) Composite theory and the effect of water on the stiffness of horn keratin. *Journal of Materials Science,* 22**,** 1385-1389.

Leuthold, W. 1977. *African ungulates: A comparitive review of their ethology and behavioral ecology*. Cambridge: Cambridge University Press.

Lind, C. A. (1997) Effect of geometry on the unsteady type-IV shock interaction. *Journal of Aircraft,* 34**,** 64-71.

Mace, B. R., D. Duhamel, M. J. Brennan & L. Hinke (2005) Finite element prediction of wave motion in structural waveguides. *Journal of the Acoustical Society of America,* 117**,** 2835-2843.

Marlow, R. S. 2003. A general first-invariant hyperelastic constitutive model. In *Constitutive models for rubber III*, 157-160. Swets and Zeitlinger, The Netherlands.

Mayer, G. (2005) Rigid biological systems as models for synthetic composites. *Science,* 310**,** 1144-1147.

McKittrick, J., P. Y. Chen, L. Tombolato, E. E. Novitskaya, M. W. Trim, G. A. Hirata, E. A. Olevsky, M. F. Horstemeyer & M. A. Meyers (2010) Energy absorbent natural materials and bioinspired design strategies: A review. *Materials Science and Engineering: C,* 30**,** 331-342.

Menig, R., M. H. Meyers, M. A. Meyers & K. S. Vecchio (2000) Quasi-static and dynamic mechanical response of Haliotis rufescens (abalone) shells. *Acta Materialia,* 48**,** 2383-2398.

Meyers, M. A. 1994. *Dynamic Behavior of Materials*. New York, NY: John Wiley & Sons, Inc.

Meyers, M. A., A. Y. M. Lin, Y. Seki, P.-Y. Chen, B. K. Kad & S. Bodde (2006) Structural Biological Composites: An Overview. *JOM.*

Mohammed, J. S. & W. L. Murphy (2009) Bioinspired Design of Dynamic Materials. *Advanced Materials,* 21**,** 2361-2374.

Mooney, M. (1940) A Theory of Large Elastic Deformation. *Journal of Applied Physics,* 11**,** 582-592.

Munch, E., M. E. Launey, D. H. Alsem, E. Saiz, A. P. Tomsia & R. O. Ritchie (2008) Tough, Bio-Inspired Hybrid Materials. *Science,* 322**,** 1516-1520.

O'Gara, B. W. & G. Matson (1975) Growth and casting of horns by pronghorns and exfoliation of horns by bovids. *Journal of Mammalogy,* 56**,** 829-846.

Oda, J., J. Sakamoto & K. Sakano (2006) Mechanical Evaluation of the Skeletal Structure and Tissue of the Woodpecker and Its Shock Absorbing System. *JSME International Journal Series A Solid Mechanics and Material Engineering,* 49**,** 390-396.

Ogden, R. W. (1972) Large deformation isotropic elasticity - on the correlation of theory and experiment for incompressible rubberlike solids. *Proc. R. Soc. London,* A326**,** 565-584.

Oliver, W. C. & G. M. Pharr (1992) An improved technique for determining hardness and elastic modulus using load and displacement sensing indentation experiments. *J. Mater. Res.,* 7**,** 1564-1583.

Packer, C. (1983) Sexual Dimorphism: The Horns of African Antelopes. *Science,* 221**,** 1191-1193.

Rhee, H., M. F. Horstemeyer, Y. Hwang, H. Lim, H. El Kadiri & W. Trim (2009) A study on the structure and mechanical behavior of the Terrapene carolina carapace: A pathway to design bio-inspired synthetic composites. *Materials Science and Engineering: C,* 29**,** 2333-2339.

Rhee, H., M. F. Horstemeyer & A. Ramsay (2011) A study on the structure and mechanical behavior of the *Dasypus novemcinctus* shell. *Materials Science and Engineering: C,* 31**,** 363-369.

103

Rivlin, R. S. (1948) Large Elastic Deformations of Isotropic Materials. IV. Further Developments of the General Theory *Philosophical Transactions of the Royal Society of London. Series A. Mathematical and Physical Sciences,* 241**,** 379-397.

Sanchez, C., H. Arribart & M. M. Giraud Guille (2005) Biomimetism and bioinspiration as tools for the design of innovative materials and systems. *Nat Mater,* 4**,** 277-288.

Sang-Hee, Y. & P. Sungmin (2011) A mechanical analysis of woodpecker drumming and its application to shock-absorbing systems. *Bioinspiration & Biomimetics,* 6**,** 016003.

Schaffer, W. M. (1968) Intraspecific Combat and the evolution of the caprini.

Schaller, G. B. 1977. *Mountain Monarchs*. Chicago: Chicago University Press.

Setchell, R. E., E. Storm & B. Sturtevant (1972) Investigation of Shock Strengthening in a Conical Convergent Channel. *Journal of Fluid Mechanics,* 56**,** 505-522.

Shadwick, R. E., A. P. Russell & R. F. Lauff (1992) The Structure and Mechanical Design of Rhinoceros Dermal Armour. *Philosophical Transactions: Biological Sciences,* 337**,** 419-428.

Shergold, O. A., N. A. Fleck & D. Radford (2006) The uniaxial stress versus strain response of pig skin and silicone rubber at low and high strain rates. *International Journal of Impact Engineering,* 32**,** 1384-1402.

Srinivasan, A. V., G. K. Haritos, F. L. Hedberg & W. F. Jones (1996) Biomimetics: Advancing man-made materials through guidance from nature - An update. *Applied Mechanics Reviews,* 49**,** 194-200.

Taya, M. 2003. Bio-inspired Design of Intelligent Materials. 54-65. San Diego, CA, United States: The International Society for Optical Engineering.

Thompson, D. A. 1917. *On Growth and Form*. New York: Dover.

Tombolato, L., E. E. Novitskaya, P.-Y. Chen, F. A. Sheppard & J. McKittrick (2010) Microstructure, elastic properties and deformation mechanisms of horn keratin. *Acta Biomaterialia,* 6**,** 319-330.

Treyssède, F. (2008) Elastic waves in helical waveguides. *Wave Motion,* 45**,** 457-470.

Trim, M. W., M. F. Horstemeyer, H. Rhee, H. El Kadiri, L. N. Williams, J. Liao, K. B. Walters, J. McKittrick & S.-J. Park (2010) The effects of water and microstructure on the mechanical properties of bighorn sheep (*Ovis canadensis*) horn keratin. *Acta Biomaterialia,* 7**,** 1228-1240.

Tucker, M. T., M. F. Horstemeyer, P. M. Gullett, H. El Kadiri & W. R. Whittington (2009) Anisotropic effects on the strain rate dependence of a wrought magnesium alloy. *Scripta materialia,* 60**,** 182-185.

Vincent, J. 1990. *Structural Biomaterials*. Princeton: Princeton University Press.

Von Mises, R. (1913) Mechanik der festen Körper im plastisch deformablen Zustand. *Gottingen Nachrichten, Math. Phys,* 4**,** 582-592.

Weiner, S., L. Addadi & H. D. Wagner (2000) Materials design in biology. *Materials Science and Engineering: C,* 11**,** 1-8.

Welles, R. E. & F. B. Welles (1961) The bighorn of death valley. *Fauna of the National Parks of the U.S.,* Fauna series no. 6.

Willinger, R., H.-S. Kang & B. Diaw (1999) Three-Dimensional Human Head Finite-Element Model Validation Against Two Experimental Impacts. *Annals of Biomedical Engineering,* 27**,** 403-410.

Yu, S.-H. (2007) Bio-inspired Crystal Growth by Synthetic Templates. *Top Curr Chem,* 271**,** 79–118.

Zhang, D., D. Arola, R. Reprogel, W. Zhang, U. Tasch & R. Dyer (2007) A method for characterizing the mechanical behaviour of hoof horn. *Journal of Material Science,* 42**,** 1108-1115.

Zhou, B. L. (2000) Bio-inspired study of structural materials. *Materials Science and Engineering C,* 11**,** 13-18.

Zukas, J. A., T. Nicholas, H. F. Swift, L. B. Greszczuk & D. R. Curran. 1992. *Impact Dynamics*. Malabar, FL: Krieger Publishing Co.

Zukas, J. A. & W. P. Walters. 1998. *Explosive Effects and Applications*. New York, NY: Springer-Verlag, Inc.

APPENDIX A

ABAQUS INPUT DECKS FOR FINITE ELEMENT ANALYSES

ABAQUS Input Deck for Cylindrical Geometry

Node and element numbers and coordinates have been removed from this input deck for brevity. The complete input deck can be found at: \\samba-cavs.hpc.msstate.edu\cmd\data1\common\ geometric_simulations\cyl\

```
*Heading
** Job name: cyl Model name: Model-1
** Generated by: Abaqus/CAE 6.10-2
*Preprint, echo=NO, model=NO, history=NO, contact=NO
**
** PARTS
**
*Part, name=Bar
*End Part
**
**
** ASSEMBLY
**
*Assembly, name=Assembly
**
*Instance, name=Cyl-1, part=Cyl
*Node (NODE SET OMITTED FOR BREVITY)
*Element, type=C3D8R  (ELEMENT SET OMITTED FOR BREVITY)
*Nset, nset=_PickedSet5, internal, generate (NSET OMITTED FOR
BREVITY)
*Elset, elset=_PickedSet5, internal, generate (ELSET OMITTED FOR
BREVITY)
** Section: BarSection
*Solid Section, elset=_PickedSet5, material=Steel
*End Instance
**
*Nset, nset=_PickedSet30, internal, instance=Cyl-1
(NSET OMITTED FOR BREVITY)
*Elset, elset=_PickedSet30, internal, instance=Cyl-1
(ELSET OMITTED FOR BREVITY)
*Elset, elset=__PickedSurf29_S3, internal, instance=Cyl-1
(ELSET OMITTED FOR BREVITY)
*Elset, elset=__PickedSurf29_S4, internal, instance=Cyl-1
(ELSET OMITTED FOR BREVITY)
*Elset, elset=__PickedSurf29_S2, internal, instance=Cyl-1
(ELSET OMITTED FOR BREVITY)
*Surface, type=ELEMENT, name=_PickedSurf29, internal
__PickedSurf29_S3, S3
__PickedSurf29_S4, S4
__PickedSurf29_S2, S2
*End Assembly
*Amplitude, name=blast-ramp
```

107

```
          0.,             0.,       9.7e-06,         0.25,
1.94e-05,           0.5,     2.91e-05,         0.75
    3.88e-05,            1.,   3.8801e-05,          0.
**
** MATERIALS
**
*Material, name=Steel
*Density
7800.,
*Elastic
 2.07e+11, 0.3
** ----------------------------------------------------------------
**
** STEP: BlastLoad
**
*Step, name=BlastLoad
Apply pressure load pulse
*Dynamic, Explicit
, 0.0008
*Bulk Viscosity
0.06, 0.
**
** BOUNDARY CONDITIONS
**
** Name: BC-1 Type: Displacement/Rotation
*Boundary
_PickedSet30, 1, 1
_PickedSet30, 2, 2
_PickedSet30, 3, 3
**
** LOADS
**
** Name: Blast load   Type: Pressure
*Dsload, amplitude=blast-ramp
_PickedSurf29, P, 100000.
**
** OUTPUT REQUESTS
**
*Restart, write, number interval=1, time marks=NO
**
** FIELD OUTPUT: F-Output-1
**
*Output, field, variable=PRESELECT, number interval=100
**
** HISTORY OUTPUT: H-Output-1
**
*Output, history
*Energy Output
ALLAE, ALLCD, ALLCW, ALLDC, ALLDMD, ALLFD, ALLIE, ALLKE, ALLMW,
ALLPD, ALLPW, ALLSE, ALLVD, ALLWK, ETOTAL
```

108

```
*End Step
```

ABAQUS Input Deck for Tapered Cylindrical (Cone) Geometry

Node and element numbers and coordinates have been removed from this input

deck for brevity. The complete input deck can be found at: \\samba-

cavs.hpc.msstate.edu\cmd\data1\common\ geometric_simulations\tap-cyl\

```
*Heading
** Job name: tap_cyl Model name: Model-1
** Generated by: Abaqus/CAE 6.10-2
*Preprint, echo=NO, model=NO, history=NO, contact=NO
**
** PARTS
**
*Part, name=tap_cyl
*End Part
**
**
** ASSEMBLY
**
*Assembly, name=Assembly
**
*Instance, name=tap_cyl, part=tap_cyl
*Node                  (NODE SET OMITTED FOR BREVITY)
*Element, type=C3D8R  (ELEMENT SET OMITTED FOR BREVITY)
*Nset, nset=_PickedSet2, internal, generate
(NSET OMITTED FOR BREVITY)
*Elset, elset=_PickedSet2, internal, generate
(ELSET OMITTED FOR BREVITY)
** Section: BarSection
*Solid Section, elset=_PickedSet2, material=Steel
1.,
*End Instance
**
*Nset, nset=_PickedSet39, internal, instance=tap_cyl
(NSET OMITTED FOR BREVITY)
*Elset, elset=_PickedSet39, internal, instance=tap_cyl
(ELSET OMITTED FOR BREVITY)
*Elset, elset=_load_S1, internal, instance=tap_cyl
(ELSET OMITTED FOR BREVITY)
*Surface, type=ELEMENT, name=load
_load_S1, S1
*Elset, elset=__PickedSurf27_S1, internal, instance=tap_cyl
(ELSET OMITTED FOR BREVITY)
*Surface, type=ELEMENT, name=_PickedSurf27, internal
__PickedSurf27_S1, S1
```

109

```
*End Assembly
*Amplitude, name=blast-ramp
            0.,            0.,       9.7e-06,          0.25,
1.94e-05,            0.5,     2.91e-05,          0.75
    3.88e-05,            1.,   3.8801e-05,          0.
**
** MATERIALS
**
*Material, name=Steel
*Density
7800.,
*Elastic
 2.07e+11, 0.3
** ----------------------------------------------------------------
**
** STEP: BlastLoad
**
*Step, name=BlastLoad
Apply pressure load pulse
*Dynamic, Explicit
, 0.0008
*Bulk Viscosity
0.06, 0.
**
** BOUNDARY CONDITIONS
**
** Name: BC-1 Type: Displacement/Rotation
*Boundary
_PickedSet39, 1, 1
_PickedSet39, 2, 2
_PickedSet39, 3, 3
**
** LOADS
**
** Name: Blast load   Type: Pressure
*Dsload, amplitude=blast-ramp
_PickedSurf27, P, 100000.
**
** OUTPUT REQUESTS
**
*Restart, write, number interval=1, time marks=NO
**
** FIELD OUTPUT: F-Output-1
**
*Output, field, number interval=100
*Node Output
A, RF, U, V
*Element Output, directions=YES
LE, PE, PEEQ, PEEQVAVG, PEVAVG, S, SVAVG
**
```

110

```
** HISTORY OUTPUT: H-Output-1
**
*Output, history, time interval=8e-06
*Energy Output
ALLAE, ALLCD, ALLCW, ALLDC, ALLDMD, ALLFD, ALLIE, ALLKE, ALLMW,
ALLPD, ALLPW, ALLSE, ALLVD, ALLWK, ETOTAL
*End Step
```

ABAQUS Input Deck for Spiral Geometry

Node and element numbers and coordinates have been removed from this input

deck for brevity. The complete input deck can be found at: \\samba-

cavs.hpc.msstate.edu\cmd\data1\common\ geometric_simulations\ spiral\

```
*Heading
** Job name: spiral Model name: Model-1
** Generated by: Abaqus/CAE 6.10-2
*Preprint, echo=NO, model=NO, history=NO, contact=NO
**
** PARTS
**
*Part, name=spiral
*End Part
**
**
** ASSEMBLY
**
*Assembly, name=Assembly
**
*Instance, name=spiral-1, part=spiral
*Node                   (NODE SET OMITTED FOR BREVITY)
*Element, type=C3D8R  (ELEMENT SET OMITTED FOR BREVITY)
*Nset, nset=_PickedSet2, internal, generate
(NSET OMITTED FOR BREVITY)
*Elset, elset=_PickedSet2, internal, generate
(ELSET OMITTED FOR BREVITY)
** Section: spiral_section
*Solid Section, elset=_PickedSet2, material=Steel
1.,
*End Instance
**
*Nset, nset=_PickedSet53, internal, instance=spiral-1
(NSET OMITTED FOR BREVITY)
*Elset, elset=_PickedSet53, internal, instance=spiral-1
(ELSET OMITTED FOR BREVITY)
*Elset, elset=__PickedSurf52_S2, internal, instance=spiral-1
(ELSET OMITTED FOR BREVITY)
*Surface, type=ELEMENT, name=_PickedSurf52, internal
```

111

```
__PickedSurf52_S2, S2
*End Assembly
*Amplitude, name=blast-ramp
            0.,            0.,      9.7e-06,          0.25,
1.94e-05,          0.5,    2.91e-05,          0.75
    3.88e-05,            1.,   3.8801e-05,           0.
**
** MATERIALS
**
*Material, name=Steel
*Density
7800.,
*Elastic
 2.07e+11, 0.3
** ----------------------------------------------------------------
**
** STEP: BlastLoad
**
*Step, name=BlastLoad
Apply pressure load pulse
*Dynamic, Explicit
, 0.0008
*Bulk Viscosity
0.06, 0.
**
** BOUNDARY CONDITIONS
**
** Name: BC-1 Type: Displacement/Rotation
*Boundary
_PickedSet53, 1, 1
_PickedSet53, 2, 2
_PickedSet53, 3, 3
**
** LOADS
**
** Name: Blast load   Type: Pressure
*Dsload, amplitude=blast-ramp
_PickedSurf52, P, 100000.
**
** OUTPUT REQUESTS
**
*Restart, write, number interval=1, time marks=NO
**
** FIELD OUTPUT: F-Output-1
**
*Output, field, number interval=100
*Node Output
A, RF, U, V
*Element Output, directions=YES
LE, PE, PEEQ, PEEQVAVG, PEVAVG, S, SVAVG
```

112

```
**
** HISTORY OUTPUT: H-Output-1
**
*Output, history, time interval=8e-06
*Energy Output
ALLAE, ALLCD, ALLCW, ALLDC, ALLDMD, ALLFD, ALLIE, ALLKE, ALLMW,
ALLPD, ALLPW, ALLSE, ALLVD, ALLWK, ETOTAL
*End Step
```

ABAQUS Input Deck for Tapered Spiral Geometry

Node and element numbers and coordinates have been removed from this input

deck for brevity. The complete input deck can be found at: \\samba-

cavs.hpc.msstate.edu\cmd\data1\common\geometric_simulations\tapered_spiral\

```
*Heading
** Job name: tap-spiral Model name: Model-1
** Generated by: Abaqus/CAE 6.10-2
*Preprint, echo=NO, model=NO, history=NO, contact=NO
**
** PARTS
**
*Part, name=tap-spiral
*End Part
**
**
** ASSEMBLY
**
*Assembly, name=Assembly
**
*Instance, name=tap-spiral-1, part=tap-spiral
*Node                     (NODE SET OMITTED FOR BREVITY)
*Element, type=C3D8R  (ELEMENT SET OMITTED FOR BREVITY)
*Nset, nset=_PickedSet2, internal, generate
(NSET OMITTED FOR BREVITY)
*Elset, elset=_PickedSet2, internal, generate
(ELSET OMITTED FOR BREVITY)
** Section: Section-2
*Solid Section, elset=_PickedSet2, material=Steel
,
*End Instance
**
*Nset, nset=_PickedSet87, internal, instance=tap-spiral
(NSET OMITTED FOR BREVITY)
*Elset, elset=_PickedSet87, internal, instance=tap-spiral
(ELSET OMITTED FOR BREVITY)
*Elset, elset=__PickedSurf86_S1, internal, instance=tap-spiral
(ELSET OMITTED FOR BREVITY)
```

113

```
*Surface, type=ELEMENT, name=_PickedSurf86, internal
__PickedSurf86_S1, S1
*End Assembly
*Amplitude, name=blast-ramp
           0.,           0.,      9.7e-06,          0.25,
1.94e-05,           0.5,     2.91e-05,          0.75
    3.88e-05,           1.,    3.8801e-05,          0.
**
** MATERIALS
**
*Material, name=Steel
*Density
7800.,
*Elastic
 2.07e+11, 0.3
** ----------------------------------------------------------------
**
** STEP: BlastLoad
**
*Step, name=BlastLoad
Apply pressure load pulse
*Dynamic, Explicit
, 0.0008
*Bulk Viscosity
0.06, 0.
**
** BOUNDARY CONDITIONS
**
** Name: BC-1 Type: Displacement/Rotation
*Boundary
_PickedSet87, 1, 1
_PickedSet87, 2, 2
_PickedSet87, 3, 3
**
** LOADS
**
** Name: Blast load   Type: Pressure
*Dsload, amplitude=blast-ramp
_PickedSurf86, P, 100000.
**
** OUTPUT REQUESTS
**
*Restart, write, number interval=1, time marks=NO
**
** FIELD OUTPUT: F-Output-1
**
*Output, field, number interval=100
*Node Output
A, RF, U, V
*Element Output, directions=YES
```

114

```
LE, PE, PEEQ, PEEQVAVG, PEVAVG, S, SVAVG
**
** HISTORY OUTPUT: H-Output-1
**
*Output, history, time interval=8e-06
*Energy Output
ALLAE, ALLCD, ALLCW, ALLDC, ALLDMD, ALLFD, ALLIE, ALLKE, ALLMW,
ALLPD, ALLPW, ALLSE, ALLVD, ALLWK, ETOTAL
*End Step
```

ABAQUS Input Deck for Ram Impact Simulations with Dry Horn Keratin

Node and element numbers and coordinates have been removed from this input

deck for brevity. The complete input deck can be found at: \\samba-

cavs.hpc.msstate.edu\cmd\data1\common\ram_simulations\

```
** Generated by: Abaqus/CAE 6.10-2
**
**
**   ABAQUS Input Deck Generated by HyperMesh Version: 10.0build60
**   Generated using HyperMesh-Abaqus Template Version:10.0build60
**
**      Template: ABAQUS/EXPLICIT 3D
**
*Heading
** Job name: ram Model name: ram_dry
*Preprint, echo=NO, model=NO, history=NO, contact=NO
**
**PARTS
**
*Part, name=Skull
*Node                          (NODE SET OMITTED FOR BREVITY)
*Element, type=C3D8       (ELEMENT SET OMITTED FOR BREVITY)
*Elset, elset=BONE_HORNS            (ELSET OMITTED FOR BREVITY)
*Elset, elset=CENTER_BONE           (ELSET OMITTED FOR BREVITY)
*Elset, elset=LEFT_SKIN, generate    (ELSET OMITTED FOR BREVITY)
*Elset, elset=LEFT_KERATIN, generate  (ELSET OMITTED FOR BREVITY)
*Elset, elset=RIGHT_SKIN, generate    (ELSET OMITTED FOR BREVITY)
*Elset, elset=RIGHT_KERATIN, generate (ELSET OMITTED FOR BREVITY)
** Section: Section-6-BONE_HORNS
*Solid Section, elset=BONE_HORNS, material=BONE
,
** Section: Section-5-CENTER_BONE
*Solid Section, elset=CENTER_BONE, material=BONE
,
** Section: Section-1-RIGHT_SKIN
*Solid Section, elset=RIGHT_SKIN, material=SKIN
```

115

```
,
** Section: Section-2-LEFT_SKIN
*Solid Section, elset=LEFT_SKIN, material=SKIN
,
** Section: Section-3-RIGHT_KERATIN
*Solid Section, elset=RIGHT_KERATIN, material=KERATIN
,
** Section: Section-4-LEFT_KERATIN
*Solid Section, elset=LEFT_KERATIN, material=KERATIN
,
*End Part
**
**
** ASSEMBLY
**
*Assembly, name=Assembly
**
*Instance, name=Skull, part=Skull
*End Instance
**
*Nset, nset=ALL, instance=Skull, generate
(NSET OMITTED FOR BREVITY)
*Elset, elset=ALL, instance=Skull, generate
(ELSET OMITTED FOR BREVITY)
*Nset, nset=_PickedSet86, internal, instance=Skull
(NSET OMITTED FOR BREVITY)
*Elset, elset=_LEFT_HORN_SURF_S1, internal, instance=Skull
(ELSET OMITTED FOR BREVITY)
*Elset, elset=_LEFT_HORN_SURF_S4, internal, instance=Skull
(ELSET OMITTED FOR BREVITY)
*Elset, elset=_LEFT_HORN_SURF_S6, internal, instance=Skull
(ELSET OMITTED FOR BREVITY)
*Elset, elset=_LEFT_HORN_SURF_S3, internal, instance=Skull
(ELSET OMITTED FOR BREVITY)
*Elset, elset=_LEFT_HORN_SURF_S5, internal, instance=Skull
(ELSET OMITTED FOR BREVITY)
*Surface, type=ELEMENT, name=LEFT_HORN_SURF
_LEFT_HORN_SURF_S1, S1
_LEFT_HORN_SURF_S2, S2
_LEFT_HORN_SURF_S4, S4
_LEFT_HORN_SURF_S6, S6
_LEFT_HORN_SURF_S3, S3
_LEFT_HORN_SURF_S5, S5
*Elset, elset=_RIGHT_HORN_SURF_S1, internal, instance=Skull
(ELSET OMITTED FOR BREVITY)
*Elset, elset=_RIGHT_HORN_SURF_S2, internal, instance=Skull
(ELSET OMITTED FOR BREVITY)
*Elset, elset=_RIGHT_HORN_SURF_S4, internal, instance=Skull
(ELSET OMITTED FOR BREVITY)
*Elset, elset=_RIGHT_HORN_SURF_S6, internal, instance=Skull
```

116

```
(ELSET OMITTED FOR BREVITY)
*Elset, elset=_RIGHT_HORN_SURF_S3, internal, instance=Skull
(ELSET OMITTED FOR BREVITY)
*Elset, elset=_RIGHT_HORN_SURF_S5, internal, instance=Skull
(ELSET OMITTED FOR BREVITY)
*Surface, type=ELEMENT, name=RIGHT_HORN_SURF
_RIGHT_HORN_SURF_S1, S1
_RIGHT_HORN_SURF_S2, S2
_RIGHT_HORN_SURF_S4, S4
_RIGHT_HORN_SURF_S6, S6
_RIGHT_HORN_SURF_S3, S3
_RIGHT_HORN_SURF_S5, S5
*Elset, elset=_LEFT_SKIN_SURF_S1, internal, instance=Skull
(ELSET OMITTED FOR BREVITY)
*Elset, elset=_LEFT_SKIN_SURF_S2, internal, instance=Skull
(ELSET OMITTED FOR BREVITY)
*Elset, elset=_LEFT_SKIN_SURF_S4, internal, instance=Skull
(ELSET OMITTED FOR BREVITY)
*Elset, elset=_LEFT_SKIN_SURF_S6, internal, instance=Skull
(ELSET OMITTED FOR BREVITY)
*Elset, elset=_LEFT_SKIN_SURF_S3, internal, instance=Skull
(ELSET OMITTED FOR BREVITY)
*Elset, elset=_LEFT_SKIN_SURF_S5, internal, instance=Skull
(ELSET OMITTED FOR BREVITY)
*Surface, type=ELEMENT, name=LEFT_SKIN_SURF
_LEFT_SKIN_SURF_S1, S1
_LEFT_SKIN_SURF_S2, S2
_LEFT_SKIN_SURF_S4, S4
_LEFT_SKIN_SURF_S6, S6
_LEFT_SKIN_SURF_S3, S3
_LEFT_SKIN_SURF_S5, S5
*Elset, elset=_RIGHT_SKIN_SURF_S1, internal, instance=Skull
(ELSET OMITTED FOR BREVITY)
*Elset, elset=_RIGHT_SKIN_SURF_S2, internal, instance=Skull
(ELSET OMITTED FOR BREVITY)
*Elset, elset=_RIGHT_SKIN_SURF_S4, internal, instance=Skull
(ELSET OMITTED FOR BREVITY)
*Elset, elset=_RIGHT_SKIN_SURF_S6, internal, instance=Skull
(ELSET OMITTED FOR BREVITY)
*Elset, elset=_RIGHT_SKIN_SURF_S3, internal, instance=Skull
(ELSET OMITTED FOR BREVITY)
*Elset, elset=_RIGHT_SKIN_SURF_S5, internal, instance=Skull
(ELSET OMITTED FOR BREVITY)
*Surface, type=ELEMENT, name=RIGHT_SKIN_SURF
_RIGHT_SKIN_SURF_S1, S1
_RIGHT_SKIN_SURF_S2, S2
_RIGHT_SKIN_SURF_S4, S4
_RIGHT_SKIN_SURF_S6, S6
_RIGHT_SKIN_SURF_S3, S3
_RIGHT_SKIN_SURF_S5, S5
```

117

```
*Elset, elset=_LEFT_KERATIN_SURF_S1, internal, instance=Skull
(ELSET OMITTED FOR BREVITY)
*Elset, elset=_LEFT_KERATIN_SURF_S2, internal, instance=Skull
(ELSET OMITTED FOR BREVITY)
*Elset, elset=_LEFT_KERATIN_SURF_S4, internal, instance=Skull
(ELSET OMITTED FOR BREVITY)
*Elset, elset=_LEFT_KERATIN_SURF_S6, internal, instance=Skull(
ELSET OMITTED FOR BREVITY)
*Elset, elset=_LEFT_KERATIN_SURF_S3, internal, instance=Skull
(ELSET OMITTED FOR BREVITY)
*Elset, elset=_LEFT_KERATIN_SURF_S5, internal, instance=Skull(
ELSET OMITTED FOR BREVITY)
*Surface, type=ELEMENT, name=LEFT_KERATIN_SURF
_LEFT_KERATIN_SURF_S1, S1
_LEFT_KERATIN_SURF_S2, S2
_LEFT_KERATIN_SURF_S4, S4
_LEFT_KERATIN_SURF_S6, S6
_LEFT_KERATIN_SURF_S3, S3
_LEFT_KERATIN_SURF_S5, S5
*Elset, elset=_RIGHT_KERATIN_SURF_S1, internal, instance=Skull
(ELSET OMITTED FOR BREVITY)
*Elset, elset=_RIGHT_KERATIN_SURF_S2, internal, instance=Skull
(ELSET OMITTED FOR BREVITY)
*Elset, elset=_RIGHT_KERATIN_SURF_S4, internal, instance=Skull
(ELSET OMITTED FOR BREVITY)
*Elset, elset=_RIGHT_KERATIN_SURF_S6, internal, instance=Skull
(ELSET OMITTED FOR BREVITY)
*Elset, elset=_RIGHT_KERATIN_SURF_S3, internal, instance=Skull
(ELSET OMITTED FOR BREVITY)
*Elset, elset=_RIGHT_KERATIN_SURF_S5, internal, instance=Skull
(ELSET OMITTED FOR BREVITY)
*Surface, type=ELEMENT, name=RIGHT_KERATIN_SURF
_RIGHT_KERATIN_SURF_S1, S1
_RIGHT_KERATIN_SURF_S2, S2
_RIGHT_KERATIN_SURF_S4, S4
_RIGHT_KERATIN_SURF_S6, S6
_RIGHT_KERATIN_SURF_S3, S3
_RIGHT_KERATIN_SURF_S5, S5
*Elset, elset=__PickedSurf87_S4, internal, instance=Skull
*Surface, type=ELEMENT, name=_PickedSurf87, internal
__PickedSurf87_S4, S4
** Constraint: S_TIE-1
*Tie, name=S_TIE-1, adjust=yes
LEFT_HORN_SURF, LEFT_SKIN_SURF
** Constraint: S_TIE-2
*Tie, name=S_TIE-2, adjust=yes
RIGHT_HORN_SURF, RIGHT_SKIN_SURF
** Constraint: S_TIE-3
*Tie, name=S_TIE-3, adjust=yes
LEFT_KERATIN_SURF, LEFT_SKIN_SURF
```

118

```
** Constraint: S_TIE-4
*Tie, name=S_TIE-4, adjust=yes
RIGHT_KERATIN_SURF, RIGHT_SKIN_SURF
*End Assembly
*Amplitude, name=Press-amp
          0.05,          0.25,           0.1,           0.5,
0.15,          0.75,           0.2,            1.,          0.201,
0.
**
** MATERIALS
**
*Material, name=BONE
*Density
 1.8e-06,
*Elastic
20000., 0.3
*Material, name=KERATIN
*Density
 1.2e-06,
*Elastic
3500., 0.3
*Material, name=SKIN
*Density
 1e-06,
*Hyperelastic, ogden
 2.2,12., 0.
*Time Points, name=TimePoints-3, GENERATE
0., 0.6, 0.05
** ----------------------------------------------------------------
--
**
** STEP: Step-1
**
*Step, name=Step-1
*Dynamic, Explicit, direct user control
5e-06, 0.6
*Bulk Viscosity
0.06, 0.
*DIAGNOSTICS, CUTOFF RATIO=1e12, DEFORMATION SPEED CHECK=OFF
**
** BOUNDARY CONDITIONS
**
** Name: spine_bc Type: Symmetry/Antisymmetry/Encastre
*Boundary
_PickedSet86, PINNED
**
** LOADS
**
** Name: pressure_load   Type: Pressure
*Dsload, amplitude=Press-amp
```

119

```
_PickedSurf87, P, 1.7
**
** OUTPUT REQUESTS
**
*Restart, write, number interval=1, time marks=NO
**
** FIELD OUTPUT: F-Output-1
**
*Output, field, time points=TimePoints-3
*Node Output
A, CF, RF, U, V
*Element Output, directions=YES
E, EDCDEN, EDT, ELEDEN, ELEN, ENER, S, SF
**
** HISTORY OUTPUT: H-Output-1
**
*Output, history, time interval=0.05
*Energy Output
ALLAE, ALLCD, ALLCW, ALLDC, ALLDMD, ALLFD, ALLIE, ALLKE, ALLMW,
ALLPD, ALLPW, ALLSE, ALLVD, ALLWK, ETOTAL
*Incrementation Output
DMASS, DT
*End Step
```

ABAQUS Input Deck for Ram Impact Simulations with Wet Horn Keratin

Node and element numbers and coordinates have been removed from this input

deck for brevity. The complete input deck can be found at: \\samba-

cavs.hpc.msstate.edu\cmd\data1\common\ram_simulations\

```
**    Generated by: Abaqus/CAE 6.10-2
**
**
**    ABAQUS Input Deck Generated by HyperMesh Version  :
10.0build60
**    Generated using HyperMesh-Abaqus Template Version :
10.0build60
**
**       Template: ABAQUS/EXPLICIT 3D
**
*Heading
** Job name: ram_wet Model name: ram_wet
** Generated by: Abaqus/CAE 6.10-2
*Preprint, echo=NO, model=NO, history=NO, contact=NO
**
**PARTS
**
```

120

```
*Part, name=Skull
*Node                      (NODE SET OMITTED FOR BREVITY)
*Element, type=C3D8        (ELEMENT SET OMITTED FOR BREVITY)
*Elset, elset=BONE_HORNS           (ELSET OMITTED FOR BREVITY)
*Elset, elset=CENTER_BONE          (ELSET OMITTED FOR BREVITY)
*Elset, elset=LEFT_SKIN, generate    (ELSET OMITTED FOR BREVITY)
*Elset, elset=LEFT_KERATIN, generate  (ELSET OMITTED FOR BREVITY)
*Elset, elset=RIGHT_SKIN, generate    (ELSET OMITTED FOR BREVITY)
*Elset, elset=RIGHT_KERATIN, generate (ELSET OMITTED FOR BREVITY)
** Section: Section-6-BONE_HORNS
*Solid Section, elset=BONE_HORNS, material=BONE
,
** Section: Section-5-CENTER_BONE
*Solid Section, elset=CENTER_BONE, material=BONE
,
** Section: Section-1-RIGHT_SKIN
*Solid Section, elset=RIGHT_SKIN, material=SKIN
,
** Section: Section-2-LEFT_SKIN
*Solid Section, elset=LEFT_SKIN, material=SKIN
,
** Section: Section-3-RIGHT_KERATIN
*Solid Section, elset=RIGHT_KERATIN, material=KERATIN_MARLOW
,
** Section: Section-4-LEFT_KERATIN
*Solid Section, elset=LEFT_KERATIN, material=KERATIN_MARLOW
,
*End Part
**
**
** ASSEMBLY
**
*Assembly, name=Assembly
**
*Instance, name=Skull, part=Skull
*End Instance
**
*Nset, nset=ALL, instance=Skull, generate
(NSET OMITTED FOR BREVITY)
*Elset, elset=ALL, instance=Skull, generate
(ELSET OMITTED FOR BREVITY)
*Nset, nset=_PickedSet86, internal, instance=Skull
(NSET OMITTED FOR BREVITY)
*Elset, elset=_LEFT_HORN_SURF_S1, internal, instance=Skull
(ELSET OMITTED FOR BREVITY)
*Elset, elset=_LEFT_HORN_SURF_S4, internal, instance=Skull
(ELSET OMITTED FOR BREVITY)
*Elset, elset=_LEFT_HORN_SURF_S6, internal, instance=Skull
(ELSET OMITTED FOR BREVITY)
*Elset, elset=_LEFT_HORN_SURF_S3, internal, instance=Skull
```

121

```
(ELSET OMITTED FOR BREVITY)
*Elset, elset=_LEFT_HORN_SURF_S5, internal, instance=Skull
(ELSET OMITTED FOR BREVITY)
*Surface, type=ELEMENT, name=LEFT_HORN_SURF
_LEFT_HORN_SURF_S1, S1
_LEFT_HORN_SURF_S2, S2
_LEFT_HORN_SURF_S4, S4
_LEFT_HORN_SURF_S6, S6
_LEFT_HORN_SURF_S3, S3
_LEFT_HORN_SURF_S5, S5
*Elset, elset=_RIGHT_HORN_SURF_S1, internal, instance=Skull
(ELSET OMITTED FOR BREVITY)
*Elset, elset=_RIGHT_HORN_SURF_S2, internal, instance=Skull
(ELSET OMITTED FOR BREVITY)
*Elset, elset=_RIGHT_HORN_SURF_S4, internal, instance=Skull
(ELSET OMITTED FOR BREVITY)
*Elset, elset=_RIGHT_HORN_SURF_S6, internal, instance=Skull
(ELSET OMITTED FOR BREVITY)
*Elset, elset=_RIGHT_HORN_SURF_S3, internal, instance=Skull
(ELSET OMITTED FOR BREVITY)
*Elset, elset=_RIGHT_HORN_SURF_S5, internal, instance=Skull
(ELSET OMITTED FOR BREVITY)
*Surface, type=ELEMENT, name=RIGHT_HORN_SURF
_RIGHT_HORN_SURF_S1, S1
_RIGHT_HORN_SURF_S2, S2
_RIGHT_HORN_SURF_S4, S4
_RIGHT_HORN_SURF_S6, S6
_RIGHT_HORN_SURF_S3, S3
_RIGHT_HORN_SURF_S5, S5
*Elset, elset=_LEFT_SKIN_SURF_S1, internal, instance=Skull
(ELSET OMITTED FOR BREVITY)
*Elset, elset=_LEFT_SKIN_SURF_S2, internal, instance=Skull
(ELSET OMITTED FOR BREVITY)
*Elset, elset=_LEFT_SKIN_SURF_S4, internal, instance=Skull
(ELSET OMITTED FOR BREVITY)
*Elset, elset=_LEFT_SKIN_SURF_S6, internal, instance=Skull
(ELSET OMITTED FOR BREVITY)
*Elset, elset=_LEFT_SKIN_SURF_S3, internal, instance=Skull
(ELSET OMITTED FOR BREVITY)
*Elset, elset=_LEFT_SKIN_SURF_S5, internal, instance=Skull
(ELSET OMITTED FOR BREVITY)
*Surface, type=ELEMENT, name=LEFT_SKIN_SURF
_LEFT_SKIN_SURF_S1, S1
_LEFT_SKIN_SURF_S2, S2
_LEFT_SKIN_SURF_S4, S4
_LEFT_SKIN_SURF_S6, S6
_LEFT_SKIN_SURF_S3, S3
_LEFT_SKIN_SURF_S5, S5
*Elset, elset=_RIGHT_SKIN_SURF_S1, internal, instance=Skull
(ELSET OMITTED FOR BREVITY)
```

122

```
*Elset, elset=_RIGHT_SKIN_SURF_S2, internal, instance=Skull
(ELSET OMITTED FOR BREVITY)
*Elset, elset=_RIGHT_SKIN_SURF_S4, internal, instance=Skull
(ELSET OMITTED FOR BREVITY)
*Elset, elset=_RIGHT_SKIN_SURF_S6, internal, instance=Skull
(ELSET OMITTED FOR BREVITY)
*Elset, elset=_RIGHT_SKIN_SURF_S3, internal, instance=Skull
(ELSET OMITTED FOR BREVITY)
*Elset, elset=_RIGHT_SKIN_SURF_S5, internal, instance=Skull
(ELSET OMITTED FOR BREVITY)
*Surface, type=ELEMENT, name=RIGHT_SKIN_SURF
_RIGHT_SKIN_SURF_S1, S1
_RIGHT_SKIN_SURF_S2, S2
_RIGHT_SKIN_SURF_S4, S4
_RIGHT_SKIN_SURF_S6, S6
_RIGHT_SKIN_SURF_S3, S3
_RIGHT_SKIN_SURF_S5, S5
*Elset, elset=_LEFT_KERATIN_SURF_S1, internal, instance=Skull
(ELSET OMITTED FOR BREVITY)
*Elset, elset=_LEFT_KERATIN_SURF_S2, internal, instance=Skull
(ELSET OMITTED FOR BREVITY)
*Elset, elset=_LEFT_KERATIN_SURF_S4, internal, instance=Skull
(ELSET OMITTED FOR BREVITY)
*Elset, elset=_LEFT_KERATIN_SURF_S6, internal, instance=Skull
(ELSET OMITTED FOR BREVITY)
*Elset, elset=_LEFT_KERATIN_SURF_S3, internal, instance=Skull
(ELSET OMITTED FOR BREVITY)
*Elset, elset=_LEFT_KERATIN_SURF_S5, internal, instance=Skull
(ELSET OMITTED FOR BREVITY)
*Surface, type=ELEMENT, name=LEFT_KERATIN_SURF
_LEFT_KERATIN_SURF_S1, S1
_LEFT_KERATIN_SURF_S2, S2
_LEFT_KERATIN_SURF_S4, S4
_LEFT_KERATIN_SURF_S6, S6
_LEFT_KERATIN_SURF_S3, S3
_LEFT_KERATIN_SURF_S5, S5
*Elset, elset=_RIGHT_KERATIN_SURF_S1, internal, instance=Skull
(ELSET OMITTED FOR BREVITY)
*Elset, elset=_RIGHT_KERATIN_SURF_S2, internal, instance=Skull
(ELSET OMITTED FOR BREVITY)
*Elset, elset=_RIGHT_KERATIN_SURF_S4, internal, instance=Skull
(ELSET OMITTED FOR BREVITY)
*Elset, elset=_RIGHT_KERATIN_SURF_S6, internal, instance=Skull
(ELSET OMITTED FOR BREVITY)
*Elset, elset=_RIGHT_KERATIN_SURF_S3, internal, instance=Skull
(ELSET OMITTED FOR BREVITY)
*Elset, elset=_RIGHT_KERATIN_SURF_S5, internal, instance=Skull
(ELSET OMITTED FOR BREVITY)
*Surface, type=ELEMENT, name=RIGHT_KERATIN_SURF
_RIGHT_KERATIN_SURF_S1, S1
```

123

```
_RIGHT_KERATIN_SURF_S2, S2
_RIGHT_KERATIN_SURF_S4, S4
_RIGHT_KERATIN_SURF_S6, S6
_RIGHT_KERATIN_SURF_S3, S3
_RIGHT_KERATIN_SURF_S5, S5
*Elset, elset=__PickedSurf87_S4, internal, instance=Skull
*Surface, type=ELEMENT, name=_PickedSurf87, internal
__PICKEDSURF87_S4_1, S4
** Constraint: S_TIE-1-1
*Tie, name=S_TIE-1-1, adjust=yes
LEFT_HORN_SURF, LEFT_GAP_SURF
** Constraint: S_TIE-2-1
*Tie, name=S_TIE-2-1, adjust=yes
RIGHT_HORN_SURF, RIGHT_GAP_SURF
** Constraint: S_TIE-3-1
*Tie, name=S_TIE-3-1, adjust=yes
LEFT_GELATIN_SURF, LEFT_GAP_SURF
** Constraint: S_TIE-4-1
*Tie, name=S_TIE-4-1, adjust=yes
RIGHT_GELATIN_SURF, RIGHT_GAP_SURF
*End Assembly
*Amplitude, name=PRESS-AMP
        0.05,         0.25,          0.1,          0.5,
0.15,          0.75,          0.2,           1.,          0.201,
0.
**
** MATERIALS
**
*Material, name=BONE
*Density
 1.8e-06,
*Elastic
20000., 0.3
*Material, name=KERATIN_MARLOW
*Density
 1.2e-06,
*Hyperelastic, marlow, poisson=0.3
*Uniaxial Test Data, smooth=3
      0.,       0.
 1.55286, 0.02172
 4.14309, 0.05442
 6.15591, 0.10193
 7.66054,  0.1487
 9.01411, 0.19546
 10.6822,  0.2574
 12.0919,  0.3042
 13.5932, 0.35077
 16.0386, 0.41299
 19.5377, 0.47522
  20.705, 0.49079
```

124

```
*Material, name=SKIN
*Density
 1e-06,
*Hyperelastic, ogden
 2.2,12., 0.
*Time Points, name=TIMEPOINTS-3, GENERATE
0., 0.6, 0.05
** -----------------------------------------------------------------
--
**
** STEP: Step-1
**
*Step, name=Step-1
*Dynamic, Explicit, direct user control
5e-06, 0.6
*Bulk Viscosity
0.06, 0.
**
** BOUNDARY CONDITIONS
**
** Name: Disp-BC-1 Type: Symmetry/Antisymmetry/Encastre
*Boundary
_PICKEDSET86, PINNED
**
** LOADS
**
** Name: SURFFORCE-1   Type: Pressure
*Dsload, amplitude=PRESS-AMP
_PICKEDSURF87, P, 1.7
**
** OUTPUT REQUESTS
**
*Restart, write, number interval=1, time marks=NO
**
** FIELD OUTPUT: F-Output-1
**
*Output, field, time points=TIMEPOINTS-3
*Node Output
A, U, V
*Element Output, directions=YES
E, EDCDEN, EDT, ELEDEN, ELEN, ENER, ER, LE, NE, S
**
** HISTORY OUTPUT: H-Output-1
**
*Output, history, time interval=0.05
*Energy Output
ALLAE, ALLCD, ALLCW, ALLDC, ALLDMD, ALLFD, ALLIE, ALLKE, ALLMW,
ALLPD, ALLPW, ALLSE, ALLVD, ALLWK, ETOTAL
*End Step
```

125